

## ABSTRACT

CHOI, SUHWAN. Manipulating Microdroplets in Alternating Electric Fields: Dispersion, Coalescence, Bridging, and Fluid Transfer. (Under the direction of Dr. Alexei V. Saveliev.)

Electrical fields induce fluid motion in many systems such as water-oil mixtures, electrolyte fluids, and colloidal suspensions. Similarly, electric fields can be used to move liquid droplets. Electrically induced droplet motion is used in many processes such as commercial ink-jet printing, petroleum oil dehydration, electrospraying, electrospinning, electrowetting in digital microfluidics and lab-on-a-chip manipulations. The tendency for adjacent droplets to coalesce is an important issue in many practical applications such as emulsification, or oppositely, the formation of water-in-oil emulsion is undesirable in crude oil production. Numerous studies have considered the droplet motion in a dc electric field, however, a few experiments in liquid-in-liquid system under an alternating electric field have been conducted. This dissertation experimentally studies fundamentals and applications of electrohydrodynamics of microdroplets in an alternating electric field.

This research work studies an application of an electric field based method for in situ emulsification of water droplets immersed in a continuous oil phase. The emulsification of a water microdroplet placed in oil was performed using a non-uniform alternating electric field formed in the pin-to-plate geometry. The emulsification process started with entrainment of the water droplet in the high electric field region near the pin electrode under the dielectrophoretic force. Breakup mechanisms responsible for a gradual dispersion of the water droplets are discussed. Water droplets with a narrow size distribution are formed at long processing times. The generated emulsion is confined near the needle electrode and had a well-defined boundary with a shape resembling a pendant drop suspended on the pin

electrode. The opposite process, partial coalescence of microdroplets is of interest for many microfluidic applications where a controlled fluid transfer from one droplet to another is required for mixing, dispensing and metering of chemical and biological fluids. This work studies a phenomena of oscillatory coalescence of water droplets situated in an alternating electric field. The oscillatory coalescence exists in a range of electrical capillary numbers and fluid conductivities and proceeds through a finite number of cycles. Each cycle includes repulsion and attractive stages and results in a partial fluid transfer through a liquid bridge formed between droplets during the repulsion stage. An energy model is proposed to describe the phenomena and its limit of existence.

© Copyright 2017 by Suhwan Choi

All Rights Reserved

Manipulating Microdroplets in Alternating Electric Fields: Dispersion, Coalescence,  
Bridging, and Fluid Transfer

by  
Suhwan Choi

A dissertation submitted to the Graduate Faculty of  
North Carolina State University  
in partial fulfillment of the  
requirements for the degree of  
Doctor of Philosophy

Mechanical Engineering

Raleigh, North Carolina

2017

APPROVED BY:

---

Dr. Alexei V. Saveliev  
Committee Chair

---

Dr. Gregory D. Buckner

---

Dr. Tarek Echehki

---

Dr. Tiegang Fang

## **DEDICATION**

This dissertation is dedicated to my family, parents, and a brother for their lifelong support and encouragement.

## **BIOGRAPHY**

Suhwan Choi was born on April 14, 1982 in Jecheon, Korea. He joined North Carolina State University in Fall 2010 for Master of Science program in Mechanical Engineering. After completing MS in 2013, Suhwan Choi decided to pursue his doctoral degree. Under the guidance of Dr. Alexei V. Saveliev, he performed research on Manipulating Microdroplets in Alternating Electric Fields: Dispersion, Coalescence, Bridging, and Fluid Transfer.

## ACKNOWLEDGMENTS

First, I would like to give thanks to God for his love and grace.

I acknowledge my advisor Dr. Alexei V. Saveliev. I would like to express my sincerest gratitude to him. I am thankful for all of the great advice, discussions, encouragement. He always showed his trust and patience with me during my PhD work.

Thank to my committee members: Dr. Gregory D. Buckner, Dr. Tarek Echehki, and Dr. Tiegang Fang for their valuable advising on my work.

Thanks to the staff in the Mechanical and Aerospace Engineering Department. You helped me navigate smoothly the road through the department. Special thanks to Dr. Paul Ro and Annie White who helped me navigate smoothly the way through the department.

I would like to acknowledge my parents and a brother in Korea whose sacrifices, teachings, and counsel made this achievement possible. Thank you for all you have done. Thanks to my son Noel Jaehee Choi. Life with you has been amazing happiness and full of unforgettable moments that will remain with me forever. My deepest gratitude is for my wife Eun Jin Joo. You have been my partner throughout this journey and your support and love are a big part of this achievement.

# TABLE OF CONTENTS

<b>LIST OF TABLES</b> .....	viii
<b>LIST OF FIGURES</b> .....	ix
Chapter 1. Introduction .....	1
1.1 Electrohydrodynamics of microdroplets in electric fields.....	2
1.1.1 Droplet Motion .....	4
1.1.2 Droplet Deformation and Break-up .....	6
1.2 Charge Relaxation in DC and AC .....	10
1.3 Thesis motivations and objectives .....	12
Chapter 2. Experimental Setup and Approach .....	16
2.1 Materials .....	16
2.2 Image Analysis .....	19
2.3 Interfacial Tension Measurement .....	22
Chapter 3. In situ Emulsification in a Non-uniform Alternating Electric Field .....	32
3.1 Introduction .....	32
3.2 Experimental .....	33
3.3 Electric Field Distribution .....	35
3.4 Characteristic Dispersion Sequence .....	36
3.5 Emulsified Droplet Diameter .....	38
3.6 Shape of Emulsion and Emulsion Properties .....	47
3.7 Mechanisms of Droplet Break-up .....	48

3.8 Comparative Analysis of Emulsification in DC and AC .....	52
Chapter 4. Coalescence of Droplets in an Alternating Electric Field .....	55
4.1 Introduction .....	55
4.2 Experimental .....	57
4.3 Coalescence Sequence .....	58
4.4 Oscillatory Coalescence .....	60
4.5 Fluid Transfer between Droplets .....	61
4.6 Limits of Existence of the Oscillatory Coalescence .....	64
4.6.1 Effect of the Electric Field .....	64
4.6.2 Effect of Non-dimensional Frequency .....	71
4.7 Energy Based Model of the Oscillatory Coalescence .....	72
4.7.1 Surface energy of the intersecting spheres model .....	73
4.7.2 Electrical energy of the intersecting spheres model .....	77
4.7.3 Total energy of the intersecting spheres model .....	79
4.7.4 Critical Electric Capillary Number .....	80
4.8 Stability of Liquid Bridge .....	86
4.9 Non-coalescence of droplets pair at low $ff_w$ .....	87
Chapter 5. Conclusions and Future work .....	92
5.1 Conclusions .....	92
5.2 Future Outlook .....	94
<b>REFERENCES</b> .....	96
<b>APPENDICES</b> .....	108

Appendix A: Volume Analysis Script .....	109
Appendix B: Droplet Center Finding Function .....	110
Appendix C: Converting to Binary Image Function .....	112
Appendix D: Droplet Interface Finding Function .....	113
Appendix E: Droplet Volume Integration in Right-hand-side Function .....	119
Appendix F: Droplet Left-side Interface Tracking Function .....	120

## LIST OF TABLES

<b>Table 1.1</b> The critical capillary number $Ca_E^*$ and the critical shape deformation $D_c$ at $Ca_E^*$ , for a conducting droplet situated in a dielectric oil [2,41-45].....	9
<b>Table 2.1</b> High voltage power supplies.....	18
<b>Table 2.2</b> The experimental droplet deformation $D$ at different $E$ for the water droplet situated in a 10000cSt silicone oil shown in Figure 2.4 (a). The $Ca_E$ calculated with the interfacial tension $\gamma_{ll} = 0.0482$ N/m at which the experimental data $D$ fits the best is listed.....	25
<b>Table 3.1</b> Experiments at 6.7 kHz were performed to study the effect of the electric field $E$ on the average diameter of emulsified water droplets.....	43
<b>Table 4.1</b> Non-dimensional radius, spacing, and surface energy for the intersecting spheres model.....	76
<b>Table 4.2</b> Non-dimensional spacing, dipole moment, and electrical energy for the intersecting spheres model.....	78
<b>Table 4.3</b> Experimental results are listed for the droplet pair at $f/f_w = 8.5 \cdot 10^{-4}$ and $f/f_w = 1.8 \cdot 10^{-3}$ with different $Ca_E$ . Illustration of the various coalescence regimes: (A) complete coalescence on the first contact, (B) stable non-coalescing shape formation, no jet emissions, (C) non-coalescence with the oscillatory motion of the droplet pair, unstable bridge formation and emulsification, (D) non-coalescence with droplets attraction, deformation and stabilization at a certain distance with electrified jet emissions.....	91

## LIST OF FIGURES

<b>Figure 1.1</b>	(a) Schematic of the experimental work on an electrified jet of glycerin and alcohol from a glass capillaries [25,26]. (b) Images of an elongated dielectric droplet in a continuous dielectric phase under influence an electric field [27].....	3
<b>Figure 1.2</b>	Droplet motion in electric fields such as (a) electrophoresis and (b) dielectrophoresis.....	4
<b>Figure 1.3</b>	Schematic diagram of the dielectrophoretic (DEP) movement. (a) Particle more polarizable than the medium move toward the pin electrode where the electric field is increasing. This is referred to as positive dielectrophoresis. (b) Particle less polarizable than the medium is pushed in the plate electrode where the electric field is decreasing. This is referred to as negative dielectrophoresis....	6
<b>Figure 1.4</b>	(a) Steady deformed shape of droplet and (b) schematic sequence of droplet breakup in electric fields.....	7
<b>Figure 1.5</b>	Schematic view of charge relaxation in (a) DC and (b) AC electric fields. (c) Diagram of electrical behavior of fluids in terms of the applied frequency and the charge relaxation frequency.....	11
<b>Figure 2.1</b>	Layout of the experimental setup.....	18
<b>Figure 2.2</b>	Image analysis procedure to measure a volume of the water droplet in oil. (a) Image captured by the CCD camera. (b) Converting to mono color. (c) Creating binary file. (d) Tracing the interface and moving the apex to the point at (0,0). (e) Converting pixel to dimension and integrating to get the volume. Dashed line indicates the droplet symmetry line. (f) Reference image capturing a needle with a known diameter.....	20

<b>Figure 2.3</b>	A schematic of interface tracing scheme.....	22
<b>Figure 2.4</b>	(a) Droplet deformation images at different electric fields (water in 10000 cSt silicone oil). (b) Plot of droplet deformation Eq. (1.6) compared with the best fit listed in Table 2.2 which were marked as red-colored diamond symbols....	24
<b>Figure 2.5</b>	(a) Image of a pendant droplet in 10000 cSt silicone oil. (b) Water-oil interface traced by image analysis marked as red line. (c) Eq. (2.12) for the curvature fit to the set of right half interfacial coordinates $I_R = (x_r, z_r)$ from the image (black color) by minimizing $\psi$ . (d) Eqs. (2.8)-(2.10) with the best fitted curvature $b_n$ generated the droplet shape $YL = (x_j, z_j)$ marked as red dots which was fitted to the $I_R = (x_r, z_r)$ .....	29
<b>Figure 2.6</b>	Schematic view of the method to calculate the minimum Euclidian distance $d_i$ between the experimental $I = (x_i, z_i)$ and Young–Laplace droplet shapes $YL = (x_j, z_j)$ .....	30
<b>Figure 2.7</b>	(a) Plot of $\psi$ are shown for the iterated radius of curvature (b) $b_n$ at the apex. (c) Plot of $\psi$ are shown for the iterated interfacial tension (d) $\gamma_{ll}$ .....	31
<b>Figure 3.1</b>	Water-in-oil emulsification using a non-uniform ac electric field. (a) Schematic of the glass cuvette with the needle electrode. (b) Electric field distribution and equipotential line in the cuvette filled with the castor oil at an instantaneous electric potential of $- 10.5$ kV (Comsol Multiphysics). (c) Layout of the experimental setup.....	34
<b>Figure 3.2</b>	Dispersion sequence of water-in-oil emulsification at 7.4 kV with 6.7 kHz at the processing times: (a) 0 s, (b) 1s, (c) 10 s, (d) 90 s, (e) 600 s. (f) Quasi-steady distribution of the emulsion with superimposed arrows representing the relative magnitude and the direction of the electric field.....	37

<b>Figure 3.3</b>	(a) Average droplet diameter as a function of the processing time at 7.4 kV with 6.7 kHz. The insets are the optical microscope images of the droplets extracted from the near the needle at 5 min and 60 min. (b) Side and top view of the emulsion after sedimentation for 24 hours.....	39
<b>Figure 3.4</b>	Emulsified water droplets image analysis. (a) Image captured from the optical microscope. (b) Converting to mono color. (c) Creating binary image. (d) Removing noise mark.....	41
<b>Figure 3.5</b>	Diameter distribution of microdroplets at 6.4 kV at 6.7 kHz.....	42
<b>Figure 3.6</b>	(a) Theoretical (Eq. 3.4) and experimental diameter of microdroplets plotted against the electric field. (b) Critical electrical capillary constant plot adjusted by $E_{eff} = E_{max}/1.9$ .....	45
<b>Figure 3.7</b>	(a) Image of emulsion cloud. Sharp boundary of the suspension is observed. (b) Electric field square distribution near the needle electrode (COMSOL Multiphysics).....	48
<b>Figure 3.8</b>	Sequential images showing initial breakup of a large droplet placed in the oil near the needle electrode powered by ac voltage at 4.2 kV with 6.7 kHz. Numbers represent recording times.....	49
<b>Figure 3.9</b>	Microscale mechanisms of water droplets breakup. (a) Small 1 and large 2 droplets in contact with the needle electrode are disintegrated by elongation and capillary breakup. (b) Droplets in regions 1 and 2 electrospaying inside the continuous phase. (c) Thin liquid bridges formed between droplets sustain the droplet chains aligned with the direction of the electric field. Under certain conditions, the bridges disintegrate to form tiny droplets.....	51
<b>Figure 3.10</b>	Dispersion sequence of water-in-oil emulsification at 7.4 kV in a DC electric field at the processing times: (a) 0 s, (b) 1 s, (c) 10 s, (d) 50 s, (e) 90 s. (f)	

	Distribution of the emulsion at 90 s in the AC electric field at the same experimental conditions.....	54
<b>Figure 4.1</b>	Schematic of the experimental setup.....	56
<b>Figure 4.2</b>	Attraction and repulsion stages of the first oscillatory coalescence cycle for a pair of water droplets suspended in silicone oil ( $E = 0.38$ kV/mm, $Ca_E = 0.09$ , $\sigma_w = 1.1$ $\mu$ S/cm, $\alpha = 0.5$ , and $f/f_w = 0.0695$ ). The liquid bridge formed in the repulsion stage alters the droplet dynamics by allowing charge and fluid transfer between droplets.....	59
<b>Figure 4.3</b>	(a) The oscillatory coalescence between a pair of droplets proceeds through 197 cycles ( $E = 0.42$ kV/mm, $Ca_E = 0.11$ , $\sigma_w = 1.1$ $\mu$ S/cm, and $f/f_w = 0.0695$ ). The liquid transfer reduces the droplet volume ratio from $\alpha = 0.5$ to $\alpha \approx 10^{-5}$ . The small satellite droplet completely coalesces during the last cycle. (b) The volume of the top droplet monotonically decreases with each cycle. (c) The oscillatory coalescence frequency remains practically constant for nearly 170 cycles.....	61
<b>Figure 4.4</b>	Fluid transfer between droplets is controlled by the pressure difference induced by surface tension and electric stresses. Laplace's droplet pressures define a direction of fluid transfer in a uniform electric field at $\alpha \sim 1$ . The oscillatory coalescence series initiated at $\alpha = 0.5$ and $\alpha = 1.5$ result in sequential increase of the larger drops ( $E = 0.40$ kV/mm, $Ca_E = 0.10$ , $\sigma_w = 9.5$ $\mu$ S/cm, and $f/f_w = 0.0695$ ). The system is metastable at the symmetry point ( $\alpha = 1$ ).....	63
<b>Figure 4.5</b>	Effect of the electric field strength on the oscillatory coalescence frequency (a) and fluid transfer (b) for $\sigma_w = 1.1$ $\mu$ S/cm and initial $\alpha = 0.5$ . The oscillation frequency is averaged over the first 10 cycles.....	65

- Figure 4.6** Sequential images of complete coalescence of the droplets on the first contact at the electric fields lower than 0.38 kV/mm ( $Ca_E < 0.09$ ) for  $\sigma_w = 1.1 \mu\text{S/cm}$ , initial  $\alpha = 0.5$ , and  $f/f_w = 0.0695$ .....66
- Figure 4.7** The bridge thins out and becomes unstable at electric fields greater than 0.47 kV/mm. The droplet oscillation and periodic formation of the thin bridge is observed at  $Ca_E = 0.156$  for  $\sigma_w = 1.1 \mu\text{S/cm}$ , initial  $\alpha = 0.5$ , and  $f/f_w = 0.0695$ . The bridge is unstable and frequently breaks up generating a fine water-in-oil emulsion in the area between two droplets.....67
- Figure 4.8** Effect of the electrical conductivity of water droplets on the oscillatory coalescence frequency (a) and fluid transfer (b) at  $E = 0.40 \text{ kV/mm}$  and initial  $\alpha = 0.5$  ( $f_c$  is averaged over the first 10 cycles).....69
- Figure 4.9** Non-coalescence mode is observed at  $Ca_E = 0.10$  for  $\sigma_w = 234 \mu\text{S/cm}$ , initial  $\alpha = 0.5$ , and  $f/f_w = 3.3 \cdot 10^{-4}$ . In this mode the droplets first attract towards one another, deform and develop electrified menisci on the adjacent surfaces. The electrically-induced emission of mass starts at a certain distance and results in a partial charge transfer between the droplets.....70
- Figure 4.10** Diagram illustrating the various coalescence regimes: (A) complete coalescence on the first contact, (B) oscillatory coalescence, (C) non-coalescence with the oscillatory motion of the droplet pair, unstable bridge formation and emulsification, (D) non-coalescence with droplets attraction, deformation and stabilization at a certain distance with electrified jet emissions; color also indicates the different coalescence regimes. The results are obtained with the water conductivities in the range from (0.5  $\mu\text{S/cm}$  to 235  $\mu\text{S/cm}$ ) and four applied frequencies: 60 Hz (hollow symbols), 10.3 kHz (symbols solid on the right), 16.8 kHz (symbols solid on the left), 41.7 kHz (solid symbols).....72

<b>Figure 4.11</b>	Geometry of the intersecting spheres model.....	74
<b>Figure 4.12</b>	The normalized surface energy as a function of the droplet spacing for the intersecting spheres model.....	77
<b>Figure 4.13</b>	The normalized electrical energy as a function of the droplet spacing for the intersecting spheres model.....	78
<b>Figure 4.14</b>	The normalized energy plotted as a function of the droplet spacing of the intersecting spheres model for a few $Ca_E$ numbers defined based on the radius of a single droplet with the same total volume.....	80
<b>Figure 4.15</b>	(a) Normalized surface and electric energies of two equal droplets as functions of relative distance between droplets. (b) Total energy of the pair for electrically isolated droplets (solid line) and for equipotential droplets (dashed line) defines the droplet coalescence path. At $Ca_E = 0.06$ the droplets coalesce after the first contact. At $Ca_E = 0.15$ the droplets coalesce through oscillatory motion.....	82
<b>Figure 4.16</b>	(a) Images of stable non-coalescing water droplets at $f/f_w = 8.5 \cdot 10^{-4}$ and $Ca_E = 0.048$ recorded the moment of contacting a droplet pair one another every 0.1 s. At $t = 33.5$ s, the stable non-coalescing water droplets was observed. (b) Images of stable non-coalescing water droplets at $f/f_w = 1.8 \cdot 10^{-3}$ and $Ca_E = 0.057$ recorded the moment of contacting a droplet pair one another every 0.1 s. At $t = 20$ s, the stable non-coalescing water droplets was observed.....	89

## Chapter 1. Introduction

Electric fields have long been used to manipulate microdroplets. The following aspects of single and multiple microdroplet dynamics has been studied: droplet transport under electrophoretic and dielectrophoretic forces [1], droplet deformation and breakup [2,3], electrically enhanced coalescence of droplets [4,5], and partial coalescence of droplets [6,7]. Creating an emulsion is another application of an electric field based microdroplet manipulation. An emulsion is a mixture of two immiscible liquid such as water in oil system. Emulsions are widely used in medicines, detergents, paints, lubricants, and foods [8-11]. Traditional methods for making emulsions involve mechanical and fluid devices, ultrasound and chemical modification by surfactants addition. Mechanical agitation of an emulsification is widely used in many applications for the simplicity despite the inefficient energy consumption. Alternative approaches include a microfluidic device to generate an emulsion by the action of capillary or hydrodynamic forces [12-16] and the use of electric forces [17,18].

In practical applications such as emulsification process, an important issue is the tendency for adjacent droplets to coalesce because of minimizing the total surface energy. Oppositely charged droplets attracts one another. The attraction enhances the probability of their coalescence [19-21]. Ristenpart et al. [6] demonstrated that two oppositely charged droplets bounced off one another if the critical electric field strength is applied. Three possible mechanisms suggested are complete coalescence, partial coalescence, and non-coalescence [22].

In this chapter, a general overview of electrohydrodynamics of microdroplets as well as their applications is provided. Applying electric fields to microdroplets can generate external forces such as dielectrophoretic and electrophoretic forces that are the main phenomena controlling the droplet motion. Differences in droplet dynamics between DC and AC electric fields are discussed. This background information motivates the work presented in this dissertation.

### 1.1 Electrohydrodynamics of microdroplets in electric fields

Electrohydrodynamics considers fluid motion in the applied electrical field and effects of the fluid motion on the electrical field distribution. Electrohydrodynamics deals with the dynamics of electrically charged fluid. Interactions between electric fields and the charged fluid can generate fluid motion such as electroosmotic motion and electrophoresis and dielectrophoresis of species in the fluid [23,24]. In the beginning of the 19th century, John Zeleny published experimental work on an electrified jet of glycerin and alcohol from a glass capillary as shown in Figure 1.1 (a) [25,26]. Taylor studied the elongation of a droplet of dielectric fluid in a continuous dielectric phase under influence an electric field, as shown in Figure 1.1 (b) [27]. A number of recent eletrohydrodynamic applications involve electrocoalescence, digital microfluidics, electrospraying, electrospinning, and emulsification [17,28-35].

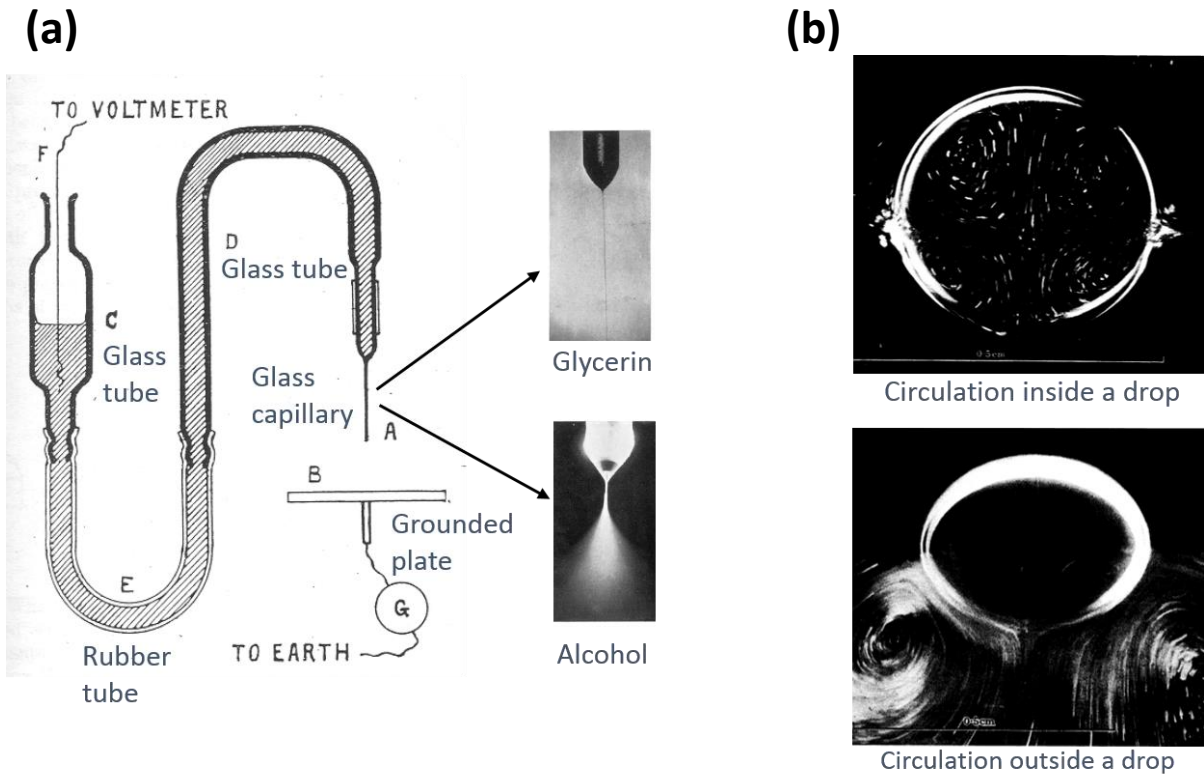


**Figure 1.1** (a) Schematic of the experimental work on an electrified jet of glycerin and alcohol from a glass capillary [25,26]. (b) Images of an elongated dielectric droplet in a continuous dielectric phase under influence of an electric field [27].

Nineteenth-century studies of droplet dynamics focused on the behavior of perfect conductors (e.g., water) or perfect dielectrics (e.g., benzene). However, a variety of practically important liquids have a finite electrical conductivity and thus do not satisfy the perfect dielectric assumptions. To address this the leaky dielectric model was introduced by Allan and Mason in 1962 [36]. It should be noted that ions are responsible for the electric charge accumulation and current transfer in liquids. Charges might be induced in poorly conducting liquids even though equilibrium charges in diffuse layers are absent [37]. In this chapter, the fundamentals of droplet motion, deformation, and breakup of a high conductivity

leaky dielectric liquid in a low conductivity medium system under electric fields are introduced and discussed.

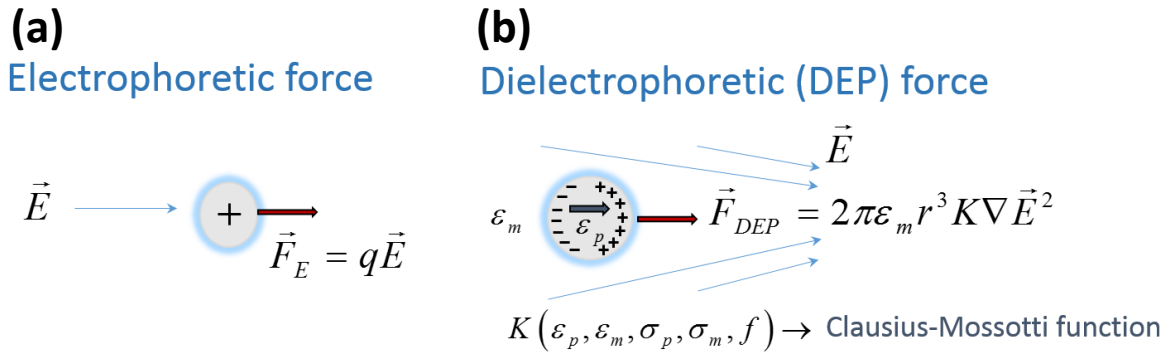


**Figure 1.2** Droplet motion in electric fields such as (a) electrophoresis and (b) dielectrophoresis.

### 1.1.1 Droplet Motion

Electrophoresis is the motion of dispersed particles with a non-zero net charge under the influence of a uniform electric field. Electrophoretic force on a charged particle is produced by the Coulomb force which is given by the product of the electric field and the charge on the particle:

$$\vec{F}_E = q\vec{E} \quad (1.1)$$

where  $q$  is the total charge on the particle and  $E$  is the magnitude of electric field, as shown in Figure 1.2 (a). In an AC electric field, the movement is oscillatory but the resulting time-averaged displacement is zero.

Dielectrophoresis is the motion of dielectric particles produced by a non-uniform electric field as shown in Figure 1.2 (b). Dielectrophoretic (DEP) force does not require

particles to be charged. The strength of the force depends on the electrical properties of the dispersed particle and the continuous phase, on the volume of the particle, on the applied frequency, as well as on the gradient of the electric field

$$\vec{F}_{DEP} = 2\pi\epsilon_m r^3 K \nabla \vec{E}^2 \quad (1.2)$$

where subscripts  $m$  and  $p$  correspond to the values of medium and particle respectively,  $\epsilon$  is the relative permittivity,  $\sigma$  is the electrical conductivity,  $f$  is the applied frequency,  $r$  is the radius of the particle, and  $K$  is the Clausius-Mossotti function given as [38]:

$$K = \frac{\epsilon_m^* - \epsilon_p^*}{\epsilon_m^* + 2\epsilon_p^*} \quad (1.3)$$

where  $\epsilon^*$  is the complex dielectric constant,  $\epsilon^* = \epsilon + i\sigma/f$ .

When the particle is more polarizable than the medium, higher charge densities are induced on the inside of the interface than on the outside. The dipole is aligned in the same direction as the applied field. Then, the particle is attracted by both electrodes but the region near the point electrode has the higher field strength. As a result, the particle is entrained in the direction of increasing field strength. DEP force is directed along the electric field gradient. This phenomenon is called positive dielectrophoresis, as shown in Figure 1.3 (a). However, if the particle is less polarizable than the outside medium, than higher charge densities are induced on the outside of the droplet/medium interface and the resulting dipole is directed opposite to the field. Both poles experience a repulsive force from the facing electrode. Thus, the pole facing the point electrode experiences a stronger repulsive force and the particle is pushed in the direction of decreasing field strength. This is called a negative dielectrophoresis, as shown in Figure 1.3 (b).

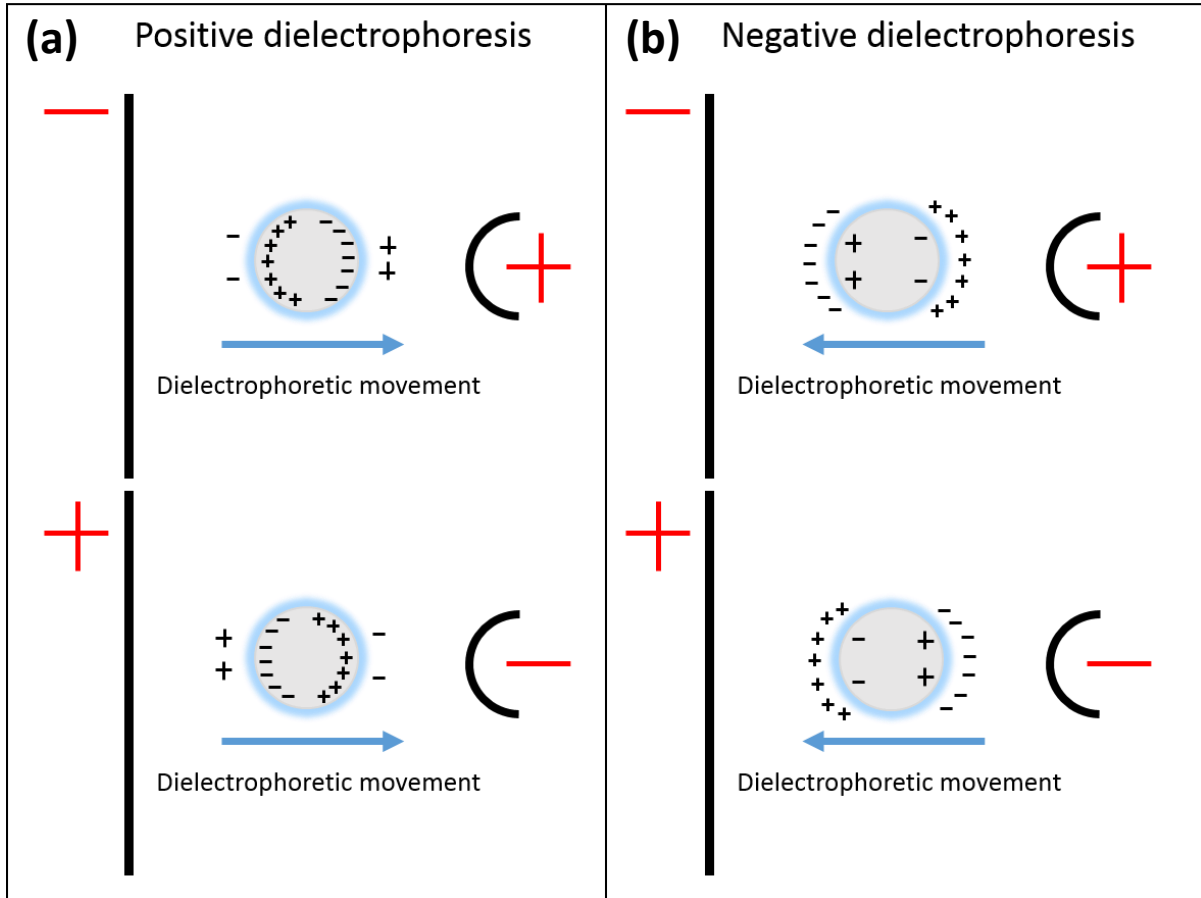


**Figure 1.3** Schematic diagram of the dielectrophoretic (DEP) movement. (a) Particle more polarizable than the medium move toward the pin electrode where the electric field is increasing. This is referred to as positive dielectrophoresis. (b) Particle less polarizable than the medium is pushed in the plate electrode where the electric field is decreasing. This is referred to as negative dielectrophoresis.

### 1.1.2 Droplet Deformation and Break-up

When a fluid is suspended in another immiscible fluid, a spherical droplet is formed owing to the influence of interfacial tension. Once external forces such as gravitation, shear, or electrical forces are exerted, the droplet deforms against the interfacial tension. When a higher conductivity leaky dielectric droplet is suspended in a low conductivity medium under a uniform external electric field, the droplet can be deformed into an oblate spheroid, which

is the result of a balance between the interfacial tension stress  $4\gamma_{ll} / d$  and the Maxwell stress  $\varepsilon\varepsilon_0 E^2 / 2$ , where  $\gamma_{ll}$  is the interfacial tension,  $d$  is the diameter of the droplet, and  $\varepsilon_0$  is the permittivity of free space, as shown in Figure 1.4 (a).

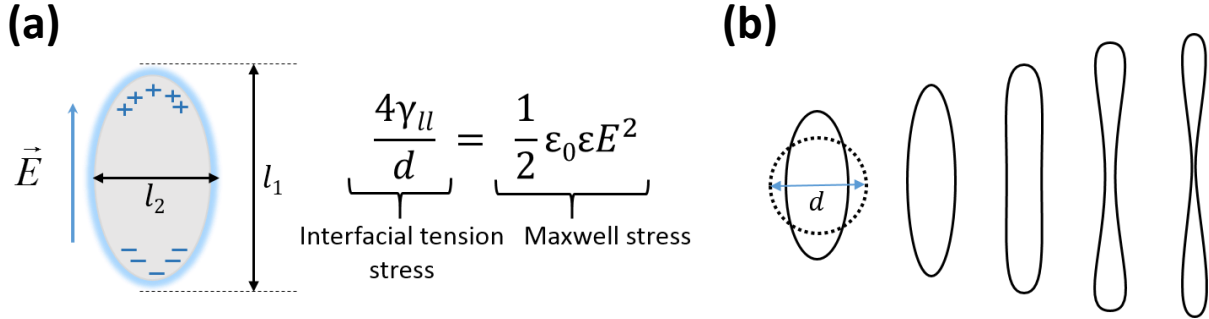


**Figure 1.4** (a) Steady deformed shape of droplet and (b) schematic sequence of droplet breakup in electric fields.

The electrical force at the liquid interface is always directed normal to the interface. It is directed from the fluid with higher relative permittivity towards the fluid with lower permittivity. The droplet deformation is described as a function of the electric capillary number defined as

$$Ca_E = d\varepsilon\varepsilon_0 E^2 / 2\gamma_{ll} \quad (1.4)$$

In the limit of small perturbations, the deformation of a spherical droplet has been analyzed by Taylor [27] and by Ajayi [39] in terms of  $Ca_E$  to the first and second order. The axisymmetric droplet deformation owing to the electrical stress is defined as:

$$D = \frac{l_1 - l_2}{l_1 + l_2} \quad (1.5)$$

where  $l_1$  and  $l_2$  are the droplet length and breadth, respectively. The droplet deformation could be expressed as

$$D = k_1 Ca_E + k_2 Ca_E^2 + O(Ca_E^3) \quad (1.6)$$

$$k_1 = \frac{9}{16} \frac{F_d(R, Q, \lambda)}{(1+2R)^2}$$

$$k_2 = \frac{k_1}{(1+2R)^2} \left[ \left( \frac{9}{5} \frac{1-R}{1+2R} - \frac{1}{16} \right) F_d + R(1-RQ) \beta(\lambda) \right]$$

$$F_d(R, Q, \lambda) = (1-R)^2 + R(1-RQ) \left[ 2 + \frac{3}{5} \frac{2+3\lambda}{1+\lambda} \right]$$

$$\beta(\lambda) = \frac{23}{20} - \frac{139}{210} \frac{1-\lambda}{1+\lambda} - \frac{27}{700} \left( \frac{1-\lambda}{1+\lambda} \right)^2$$

where subscripts  $m$  and  $p$  indicate values of medium and droplet, respectively,  $R = \sigma_m/\sigma_p$  is a conductivity ratio,  $Q = \varepsilon_p/\varepsilon_m$  is a dielectric constant ratio, and  $\lambda = \nu_p/\nu_m$  is a viscosity ratio [40]. The function  $F_d(R, Q, \lambda)$  predicts the deformation shape (prolate with  $F_d > 0$  and oblate with  $F_d < 0$ ). Below a certain critical capillary number, a conducting droplet maintains a steady deformed shape. In the case of  $F_d = 0$ , the droplet will remain spherical under any electric field.

**Table 1.1** The critical capillary number  $Ca_E^*$  and the critical shape deformation  $D_c$  at  $Ca_E^*$ , for a conducting droplet situated in a dielectric oil [2,4.1-45].

Methodology	$Ca_E^*$	$D_c$ at $Ca_E^*$	Reference
Spheroidal approximation	0.210	0.310	Taylor, 1964
Numerical method	0.209	0.293	Miksis, 1981
Boundary element method	0.206	0.259	Sherwood, 1988
Boundary element method	0.2044	0.200	Dubash and Mestel, 2007
Experiments	0.214	0.220	Ha and Yang, 2000
Experiments	0.212	0.225	Rahul <i>et al.</i> , 2014

As the capillary number  $Ca_E$  is increased beyond the critical capillary number  $Ca_E^*$ , the Maxwell stress on the droplet increases until overwhelming the interfacial tension, thereby resulting in droplet breakup, as shown in Figure 1.4 (b). Taylor calculated the critical capillary number  $Ca_E^* = 0.21$  in a conducting droplet situated in a dielectric fluid using the spheroidal droplet approximation [46]. Table 1.1 shows the comparison of the critical capillary number  $Ca_E^*$  and the critical shape deformation  $D_c$  at  $Ca_E^*$  with different experimental, analytical, and numerical studies [2,41-45]. The  $Ca_E^*$  are comparable and a narrow scatter around 10% is observed, supporting  $Ca_E^* = 0.21 \pm 0.02$ .

## 1.2 Charge Relaxation in DC and AC

As it was mentioned previously that electric charges are created by ion motion even in poorly conducting fluids. An important characteristic time of a fluid under an electric field is the charge relaxation time for ions required to move a distance of the order of the Debye length (how far the electrostatic effects remain) by diffusion [47]. The characteristic time

$$\tau_r = \frac{\varepsilon\varepsilon_0}{\sigma} \quad (1.7)$$

can be identified as the ratio of the permittivity  $\varepsilon\varepsilon_0$  and the electrical conductivity  $\sigma$ . The charge relaxation frequency associated with this time has the form:

$$f_r = \frac{1}{\tau_r} \quad (1.8)$$

Figure 1.5 (a) shows a schematic view of charges relaxing in a conducting water droplet suspended in a poorly conducting oil system in a DC electric field. In this case the charge relaxation frequencies for water and oil are  $f_w = \sigma_w/\varepsilon_0\varepsilon_w$  and  $f_o = \sigma_o/\varepsilon_0\varepsilon_o$ , respectively. Charges in the water droplet can be relaxed and accumulated at the interface in a short time based on the relaxation frequency resulting in the zero electric field inside the droplet. Charges in the oil, however, are relaxing relatively slow and the electric field in the oil phase remains non-zero until all charges are relaxed. After relaxation of all charges in the oil, both fluids shield the electric field as conductors.

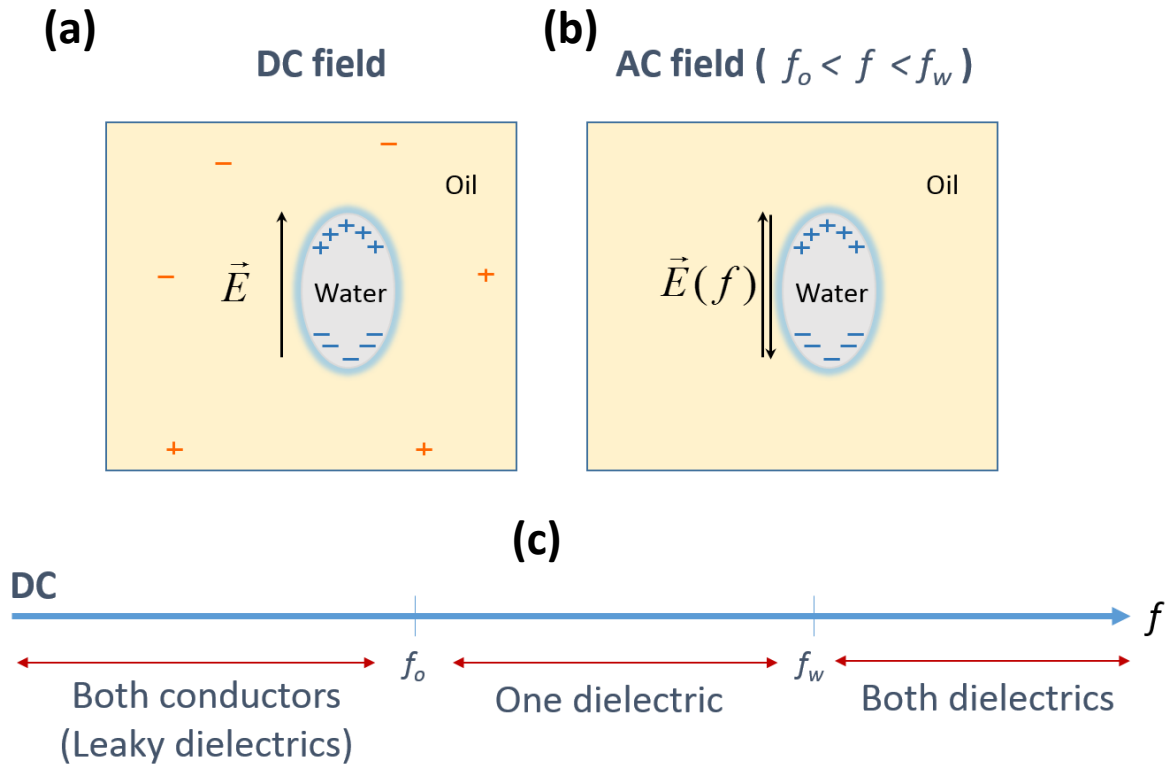


**Figure 1.5** Schematic view of charge relaxation in (a) DC and (b) AC electric fields. (c) Diagram of electrical behavior of fluids in terms of the applied frequency and the charge relaxation frequency.

In AC fields, the charges will alternate with the applied frequency  $f$ . Figure 1.5 (b) shows the case  $f_w > f \gg f_o$  where the charges in water droplet alternate. At the applied frequency higher than the charge relaxation frequency of the oil, the oil behaves as a pure dielectric. The charges formed on the water/oil interface oscillate with frequency  $f$  and reduce the field in the droplet. These charges are zero in time-averaged value. This case,  $f_w > f \gg f_o$ , represents a classic case of a leaky dielectric droplet suspended in a pure dielectric fluid. Three characteristic ranges can be identified depending on the applied frequency: both fluids behave as leaky dielectrics  $f < f_o$  and  $f < f_w$ , one fluid is a leaky dielectric and another is a

perfect dielectric  $f > f_o$  and  $f < f_w$ , both fluids can be considered perfect dielectrics at  $f > f_o$  and  $f > f_w$ . (Fig. 1.5c).

### 1.3 Thesis Motivations and Objectives

Emulsions can be generated in different methods such as impellers, rotor mixers, colloid milling, flow-injection, high pressure, ultrasonic, etc. These methods involve mechanical devices generating high shear to disintegrate the discontinuous phase into small droplets. An electric field based method, however, induces a high electric stress on a droplet surface to overcome the interfacial tension force, resulting in a droplet emulsification. The electrostatic methods have evolved more efficient emulsification techniques for water droplets in oil [48,49]. Especially for the poorly conducting high viscous oil system, the electrical energy required per unit volume to generate an emulsion can be 2 orders of magnitude less compared to the mechanically involved systems [50,51]. An important issue in practical applications such as emulsification process is the tendency for adjacent droplets to coalesce because of minimizing the total surface energy. Coalescence of droplet pairs, however, is rich in physical effects and is a subject of continuous research efforts in many field, for example in oil-water separation [5].

Several other techniques remain unexplored: emulsification of microdroplets using AC and DC electric fields, coalescence in AC electric fields, and controlled direct fluid transfer between free or sessile microdroplets [52,53].

Novel experimental approaches to control emulsification, coalescence, and precise metering and dispensing of fluids are needed for applications in biotechnology, microfluidics, and medicine. This dissertation describes the experimental study on microdroplet manipulation in electric fields for dispersion, coalescence, liquid bridging and fluid transfer. Although electrically induced droplet dynamics is widely known in DC electric fields, our studies focus on liquid-in-liquid system under an alternating electric field which has not been studied extensively. Thus, the unique contribution of this thesis is new insights into controlling the interface between different immiscible liquids under an AC electric field.

As discussed in the above section, novel methods for controlled emulsification of single droplets are required for chemical and biological analysis, drug delivery and medical applications. Precise metering and dispensing of chemical and biological reagents are also important for a number of medical and biological applications. This research attempts to address the following objectives:

- To study an application of non-uniform alternating electric fields for *in situ* emulsification of small water droplets. To demonstrate that high density small diameter water-in-oil emulsions can be generated using non-uniform ac electric fields applied between needle and plate electrodes.
- To investigate breakup mechanisms responsible for a gradual dispersion of the water droplets in alternating electric field.
- To study coalescence patterns of droplets in an alternating electric field.
- To study a fluid transfer from one droplet to another.

- To develop a model to describe the coalescence phenomenon and define its limit of existence.

Chapter 2 presents the experimental setup and approach of this work, including experimental materials and methods, high voltage generating systems, image analysis, and a methodology to evaluate an equilibrium interfacial tension.

In Chapter 3, an electric field based method for in situ emulsification of water droplets immersed in a continuous oil phase is reported. High density water-in-oil emulsions are generated using non-uniform ac electric fields applied between needle and plate electrodes. Breakup mechanisms responsible for a gradual dispersion of the water droplets are investigated. Identified mechanisms involve drop elongation to a cylindrical shape followed by a capillary breakup, ac electrospaying from individual water droplets, and formation and breakup of bead-like structures comprised by the water droplets interconnected by thin water bridges. Water droplets with diameters close to 1  $\mu\text{m}$  and a narrow size distribution are formed at long processing times. The generated emulsion has a well-defined boundary and is confined near the needle electrode in a shape resembling a pendant droplet.

In Chapter 4, partial coalescence of microdroplets in AC electric fields is considered. This phenomenon is of interest for a number of microfluidic applications where a controlled fluid transfer from one droplet to another is required for mixing, dispensing and metering of chemical and biological fluids. A phenomenon of oscillatory coalescence of water droplets situated in an alternating electric field is reported. The oscillatory coalescence exists in a

range of electrical capillary numbers and fluid conductivities and proceeds through a finite number of cycles. Each cycle includes attractive and repulsion stages and results in a partial fluid transfer through a liquid bridge formed between droplets during the repulsion stage. An energy model to describe the phenomenon and define its limit of existence is proposed.

## Chapter 2. Experimental Setup and Approach

All the experimental work presented here was performed using the experimental setup equipped with a high voltage power supply system and a high resolution image capturing system. The acquired images were processed using specially developed image analysis tools. Microdroplets were manipulated and analyzed by this system in two experimental studies. In the first study, in situ emulsification of water droplets in oil was tested in pin-to-plate electrical geometry. In the second, droplet coalescence was studied in plate-to-plate uniform electric fields. The common experimental details are described in the following sections of this Chapter.

### 2.1 Materials

Deionized water with the electrical conductivity of  $0.05 \mu\text{S}/\text{cm}$  was obtained from Milli-Q water system (Merck Millipore, Direct-Q). The conductivities of water droplets were adjusted in the range from  $0.05 \mu\text{S}/\text{cm}$  to  $250 \mu\text{S}/\text{cm}$  by adding salt into the Milli-Q water. A conductivity meter (Model CON 400, OAKTON Co.) was used to measure the conductivity at the room temperature of  $23 \text{ }^\circ\text{C}$  for each experiment. Oils used as a continuous phase were castor oil (conductivity  $\sigma_{co} = 10^{-7} \mu\text{S}/\text{cm}$ , dielectric constant  $\varepsilon_{co} = 3.8$ , kinematic viscosity  $\nu_{co} = 850 \text{ cSt}$ , and surface tension  $\gamma_{co} = 29 \text{ mN}/\text{m}$ ) and silicone oil (conductivity  $\sigma_{so} = 10^{-11} \mu\text{S}/\text{cm}$ , dielectric constant  $\varepsilon_{so} = 2.7$ , kinematic viscosity  $\nu_{so} = 10000 \text{ cSt}$ , and surface tension  $\gamma_{so} = 21 \text{ mN}/\text{m}$ ). For the voltage source, direct current (DC) and alternating current (AC) power generator with a high voltage transformer were used to apply electric potential to the

liquid-liquid systems in this research as shown in Figure 2.1. The high voltage power supplies used in this work are listed in Table 2.1. A stainless steel was used as a material for the first and the second electrode. A pin-to-plate electrical geometry, where a non-uniform electric field was induced, was composed of a needle with the outer diameter of 0.3 mm and blunt tip and ground plate. A uniform electric field was created by two plane electrodes. The voltage waveform (electric potential in peak-to-peak and root-mean-square values, and applied frequency) was monitored using a Tektronix oscilloscope (Model TDS 2024B). A CCD camera (Model PLB954, Pixelink, Inc.) capable of filming at up to 10 frames per second was used to capture a droplet dynamics. The spatial resolution of the camera ( $1392 \times 1040$  pixels) was adequate to analyze dynamical behavior of microdroplets. The camera was equipped with a scientific grade zoom lens (Model 125, Optem, Inc.) in order to obtain a view of approximately a droplet with  $10 \mu\text{m}$  in diameter. Image acquisition was controlled by PixeLINK Capture OEM (Pixelink, Inc.) on a computer. A motorized positioning stage was designed to adjust the distance between the electrodes. The generated emulsions were characterized using an optical microscope (Model TC5400, Meiji Techno Co.).

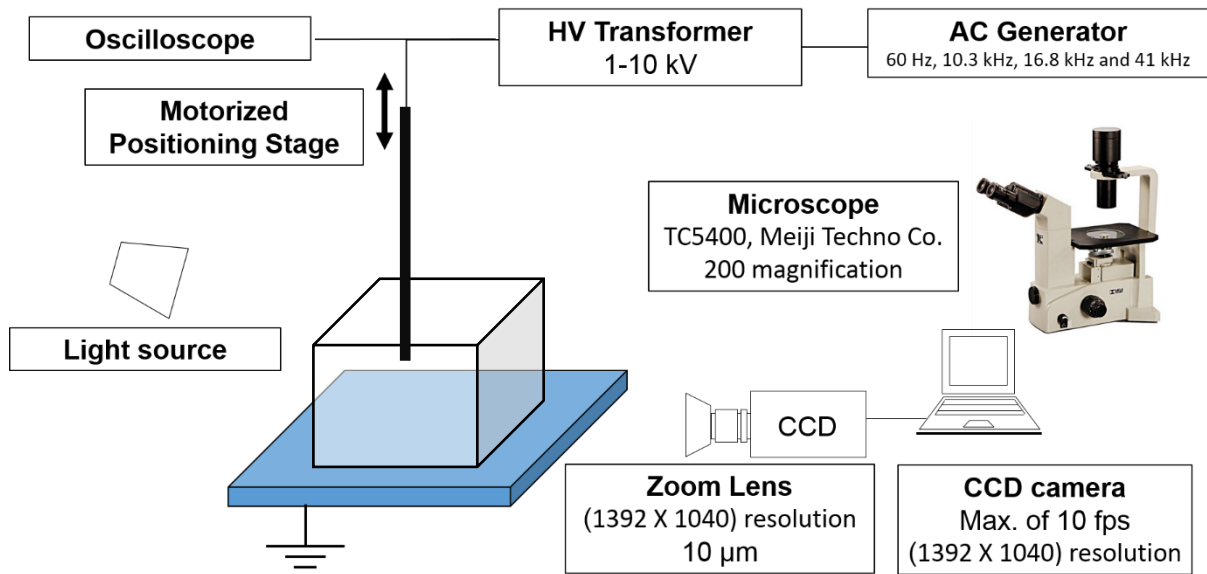


**Figure 2.1** Layout of the experimental setup.

**Table 2.1** High voltage power supplies.

Type	Company	Model	frequency
DC	Glassman High Voltage, Inc.	EQ30N40	N/A
AC	Webster-Wilkinson Ltd.	TYPE 44324	60 Hz
AC	Compact Power, Inc.	MAC-01A	1 kHz to 20 kHz
AC		PVM12	20 kHz to 50 kHz

## 2.2 Image Analysis

All experimental images captured with the CCD color camera were analyzed using Matlab with customized code. For each experimental image sequence, positions, shapes, and length of the droplets were measured. Each image has a bitmap corresponding to three bits of information (red, green and blue) with pixel values ranging from 0 to 255. The back light illumination with camera positioned at an angle to the light source allowed droplet interface to appear significantly darker than other areas as shown in Figure 2.2 (a). The image then was converted to mono color with grayscale from 0 to 255 where 0 corresponds to black and 255 corresponds to white color (Fig. 2.2b). A threshold could be chosen to convert the mono to binary image where pixels below the threshold had their values be 255 to represent the interface and pixels above it be 0 to distinguish the surrounding areas (Fig. 2.2c).

It was extremely important to accurately trace the water-oil interface using individual pixels. Figure 2.3 is a zoom-in view of an arbitrary location on the water-oil interface. Each pixel represented by a square has either white or black color where white represents the interface which we wish to trace and black represents inside of the droplet and the outside oil. The pixels at the right bottom corner end were investigated first. The entire bottom row was investigated in right-to-left manner as indicated by the blue colored arrows until a pixel with value 255 (white) is found. The pixel marked with '1' in Figure 2.3 was the first interfacial point. Then, the first right end pixel on the right at the second row was called and the entire row is investigated again. The black colored arrows indicate moving to the right above row. Finally a pixel with a value 255 marked by '2' is reached. The process continues

until the last row is investigated. The left side of interface is investigated in the same manner as the right side.

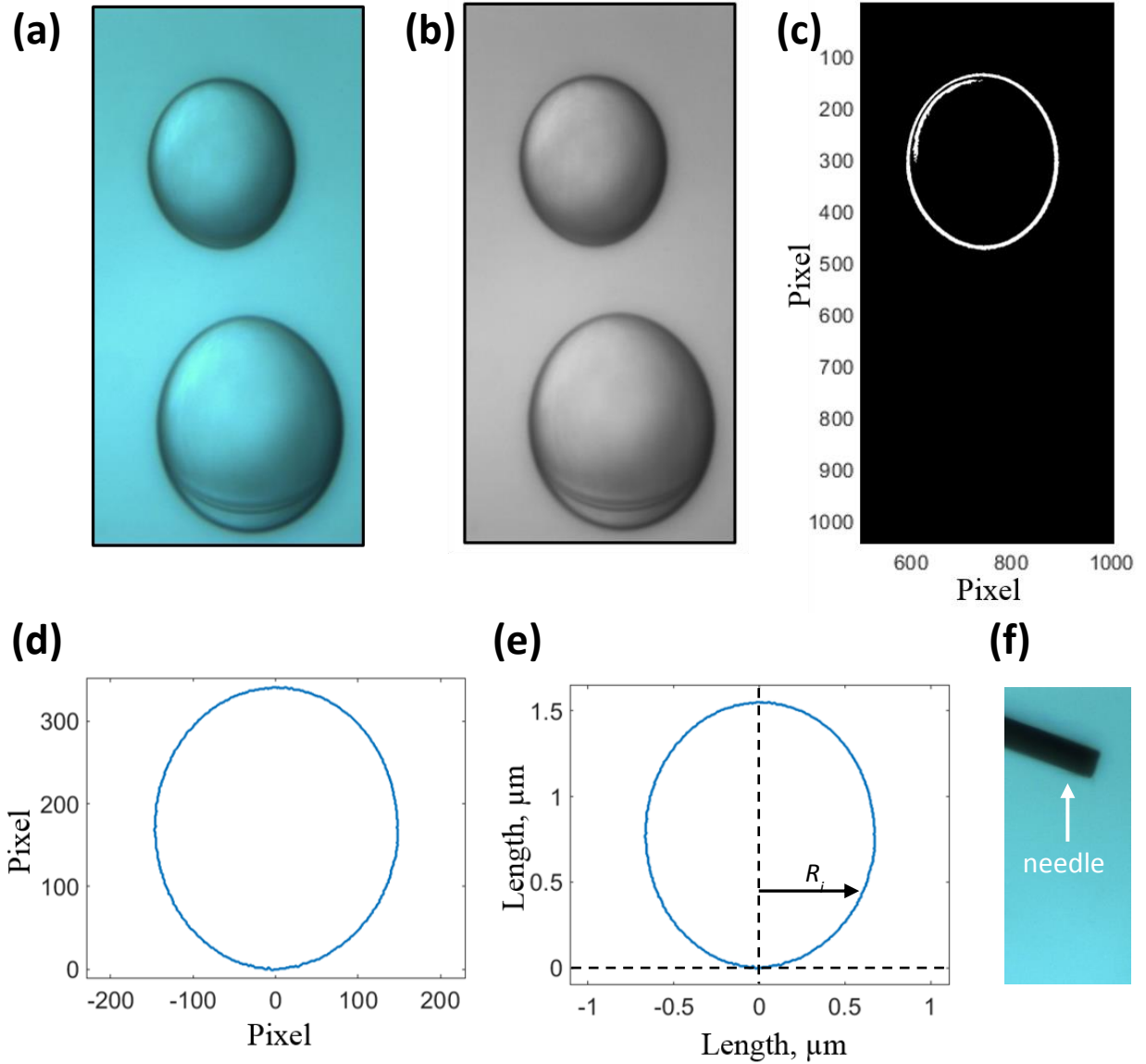


**Figure 2.2** Image analysis procedure to measure a volume of the water droplet in oil. (a) Image captured by the CCD camera. (b) Converting to mono color. (c) Creating binary file. (d) Tracing the interface and moving the apex to the point at (0,0). (e) Converting pixel to dimension and integrating to get the volume. Dashed line indicates the droplet symmetry line. (f) Reference image capturing a needle with a known diameter.

This algorithm is used to trace both the right and left interface frame by frame. All the identified points represent the interface. Figure 2.2 (d) shows the interface where the apex moved to the point at (0,0). Then, the scale in pixel was converted to the dimension in mm by using an image capturing a needle with a known diameter at the same condition as shown in Figure 2.2 (f). The needle with a diameter of 0.3 mm was captured in the image where the diameter occupied ~55 pixels. As a result, the area of one pixel was evaluated as  $25 \mu\text{m}^2$ . The volume of the droplet was calculated by integrating the interfacial points. Figure 2.2 (e) shows the water-oil interface with the apex located at the point (0,0) in real dimension in mm. In Figure 2.2 (e), a length from the center line of the droplet to an arbitrary point can be regarded as a radius  $R_i$  of a circular disk which is perpendicular to the center with the thickness  $h$  of  $25 \mu\text{m}^2$  which corresponds to the area of a pixel. Then, each circular disk has a volume of  $\pi R_i^2 h$ . After integrating all the circular volume, we end up with

$$V = \sum \pi R_i^2 h \quad (2.1)$$

where  $V$  is the volume of the droplet.

Each experimental image sequence analyzed in this manner can allow to measure positions, shapes, and length of the droplets, volume flowrate, fluid velocity through a liquid bridge, and droplet movement.

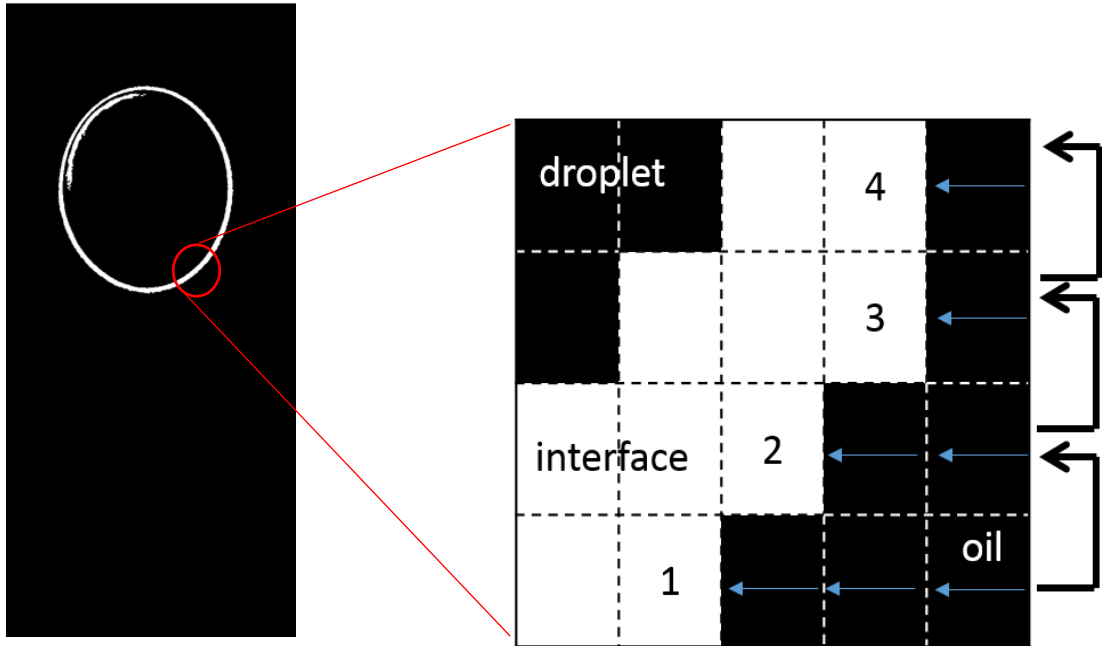


**Figure 2.3** A schematic of interface tracing scheme.

### 2.3 Interfacial Tension Measurement

A process to estimate an equilibrium interfacial tension is discussed in this section. An axisymmetric droplet deformation with respect to  $Ca_E$  is considered. An initial water droplet with a radius  $a = 0.804$  mm was suspended in a 10000cSt silicone oil. A uniform electric field was varied in a range from 0 to 0.70 kV/mm to have the droplet deformed. Each deformed steady shape was captured by the CCD camera at different electric fields, as shown in Figure 2.4 (a). The water-oil interface was traced by the threshold method [54]. Then, the deformation factor  $D = (l_1 - l_2) / (l_1 + l_2)$  was analyzed at different electric fields for each image. The experimentally measured droplet shape deformation  $D$  at different  $E$  is listed in Table 2.2. The initial droplet was observed as a sphere. Upon applying  $E$  the droplet deformed into a prolate shape, as shown in Figure 2.4 (a). The deformation factor  $D$  increases with

increasing  $E$  until the critical capillary number reached  $Ca_E^* = 0.21$  where the droplet was broken up.

In this water-oil system, deformation parameters were analyzed based on the water and oil properties: conductivity ratio  $R = 10^{-12}$ , dielectric constant ratio  $Q = 29.1$ , viscosity ratio  $\lambda = 10^{-4}$ ,  $F_d(R, Q, \lambda) = 1$ ,  $\beta(\lambda) = 0.4497$ ,  $k_1 = 0.5625$ , and  $k_2 = 0.9773$ . This parameters define the droplet shape according to Eq. (1.6). The interfacial tension can be predicted using data in Table 2.2. For example, at  $E = 0.57$  kV/mm and  $D = 0.095849$ ,  $Ca_E$  can found as:

$$Ca_E = \frac{-k_1 + \sqrt{k_1^2 - 4k_2(-D)}}{2k_2} \quad (2.2)$$

Substituting  $D = 0.095849$  into Eq. (2.2), the capillary number is obtained as  $Ca_E = 0.1375$ .

Then, the interfacial tension value can be analyzed by rearranging Eq. (1.4) defined as

$$Ca_E = d\varepsilon\varepsilon_0 E^2 / 2\gamma_{ll},$$

$$\gamma_{ll} = \frac{a\varepsilon\varepsilon_0 E_0^2}{Ca_E}. \quad (2.3)$$

At  $E = 0.57$  kV/mm, the interfacial tension is obtained as  $\gamma_{ll} = 0.0464$  N/m. At different

experimental data, the  $\gamma_{ll}$  can be analyzed with the same manner. Then, the analyzed  $\gamma_{ll}$  are

compared with the theoretical droplet deformation Eq. (1.6) to have the best fit by iterating

$\gamma_{ll}$ . Figure 2.4 (b) is the plot of the theoretical droplet deformation. Eq. (1.6) indicated by

the black line is compared with the best fit data marked as red-colored diamond symbols. The

$Ca_E$  calculated with the interfacial tension  $\gamma_{ll} = 0.0482$  N/m at which the experimental data  $D$

fits the best is listed in the Table 2.2. The  $\gamma_{II}$  is comparable and support  $\gamma_{II}=0.0482 \pm 0.002$  N/m [55].

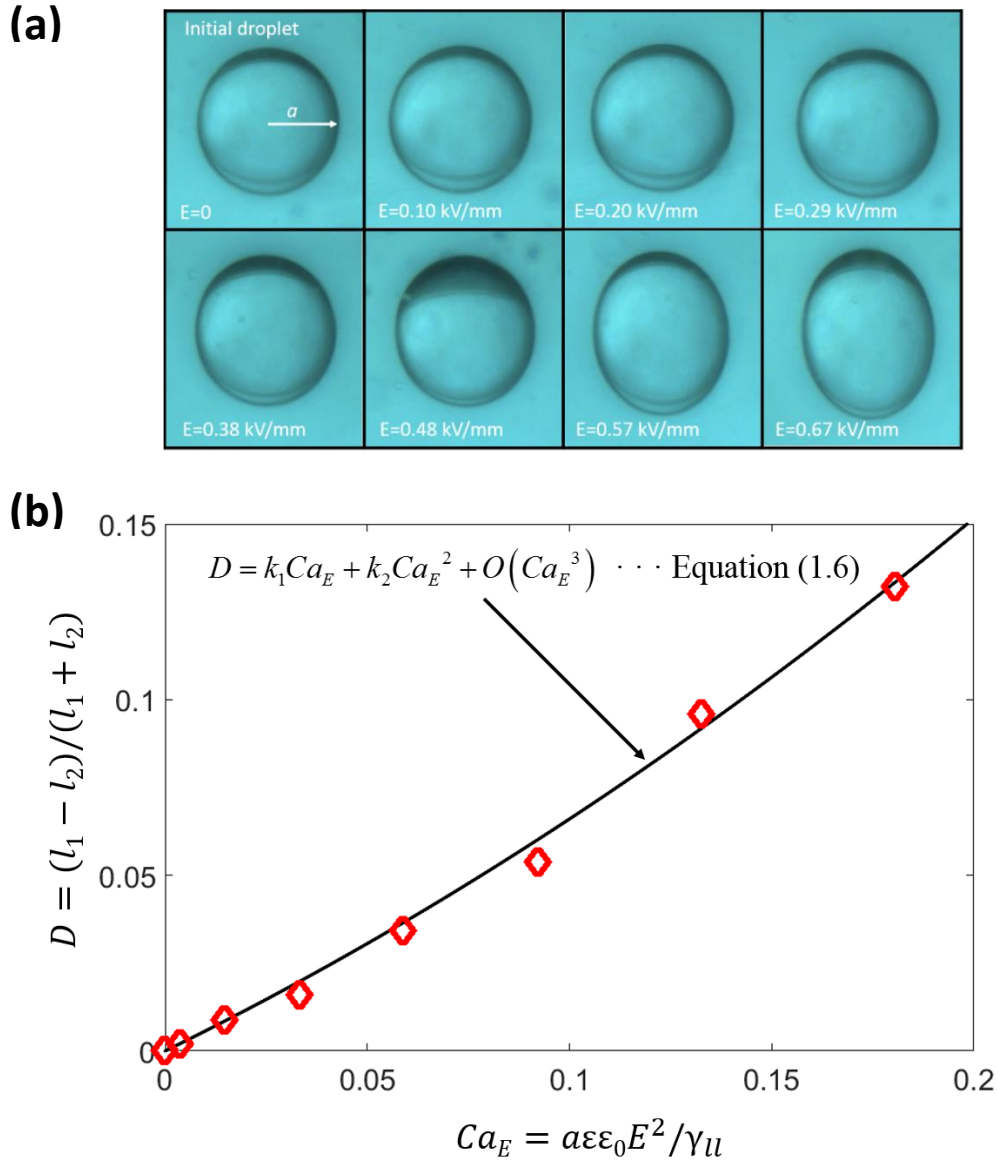


**Figure 2.4** (a) Droplet deformation images at different electric fields (water in 10000 cSt silicone oil). (b) Plot of droplet deformation Eq. (1.6) compared with the best fit listed in Table 2.2 which were marked as red-colored diamond symbols.

**Table 2.2** The experimental droplet deformation  $D$  at different  $E$  for the water droplet situated in a 10000cSt silicone oil shown in Figure 2.4 (a). The  $Ca_E$  calculated with the interfacial tension  $\gamma_{ll} = 0.0482$  N/m at which the experimental data  $D$  fits the best is listed.

$E$ (kV/mm)	$D$	$Ca_E$	Condition
0	0	0	Initial droplet
0.10	0.001985	0.0037	deformed
0.20	0.008969	0.0147	deformed
0.29	0.015972	0.0332	deformed
0.38	0.034359	0.0589	deformed
0.48	0.053728	0.0921	deformed
0.57	0.095849	0.1326	deformed
0.67	0.132051	0.1805	deformed
0.75	-	0.2280	Breakup

An axisymmetric droplet shape analysis for pendant droplets is another alternative method for measuring the interfacial tension  $\gamma_{ll}$ . An axisymmetric water droplet was created from a capillary needle. A CCD camera was used to capture the pendant droplet in the 10000cSt silicone oil (Fig. 2.5a). The water-oil interface was traced by the threshold method

[54]. Figure 2.5 (b) shows the image with a superposition of traced points marked as red dots. The set of interfacial coordinates from the image traced by the threshold method was denoted as  $I = (x_i, z_i)$  where  $x$  and  $z$  are radial and vertical positions of the interface, respectively, (Fig. 2.5b). Then, the interface shape was compared with a prescribed shape by the Young-Laplace equation

$$\gamma_{ll}\kappa = \Delta\rho g z - \frac{2\gamma_{ll}}{b_n} \quad (2.4)$$

where  $\kappa = \kappa_1 + \kappa_2$  is the mean curvature,  $b_n$  is the radius at the droplet apex (Fig. 2.5b). The equation can be non-dimensionalized with the length  $b_n$  leading to

$$\kappa^* = Bo^* z^* - 2 \quad (2.5)$$

where the superscript ‘\*’ indicates dimensionless values,  $Bo^* = \Delta\rho g b_n^2 / \gamma_{ll}$  is the Bond number which is the ratio between the interfacial tension and body force. In order to determine a droplet shape from the equation with the mean curvature

$$\kappa = \frac{d\theta}{ds^*} + \frac{\sin\theta}{x^*} , \quad (2.6)$$

Eq. (2.5) can be modified to the form

$$\frac{d\theta}{ds^*} + \frac{\sin\theta}{x^*} = Bo^* z^* - 2 . \quad (2.7)$$

This set of differential equations to be solved is given as:

$$\frac{d\theta}{ds^*} = 2 - Bo^* z^* - \frac{\sin\theta}{x^*} \quad (2.8)$$

$$\frac{dx^*}{ds^*} = \cos\theta \quad (2.9)$$

$$\frac{dz^*}{ds^*} = \sin \theta \quad (2.10)$$

where  $s$  is the arc length,  $\theta$  is the interface tangential angle and the axis [56-58]. The Runge-Kutta with 4th-order method was used to integrate these equation with initial conditions as  $x(0) = 0$ ,  $z(0) = 0$ , and  $\theta(0) = 0$  numerically. The droplet shape given by Eqs. (2.8)-(2.10) is denoted as  $YL = (x_j, z_j)$ . The solutions of the Young–Laplace equation presented above are symmetric about the apex, so the set of interfacial coordinates from the image  $I$  is split into two halves about the vertical axis of symmetry. The resulting left and right halves are  $I_L = (x_l, z_l)$  and  $I_R = (x_r, z_r)$ .

The droplet shape prescribed by the Eq. (2.7) was compared with the experimentally measured droplet shape. There are two unknown parameters in the process: interfacial tension and the curvature at the apex. The initial guess for the radius of curvature at the apex  $b_n$  was the maximum distance between the axis of symmetry and the droplet surface. The mean curvature  $\kappa_1 = d\theta/ds^*$  can be expressed in another form as

$$\kappa_1 = \frac{\frac{d^2 z^*}{dx^{*2}}}{\left[ 1 + \left( \frac{dz^*}{dx^*} \right)^2 \right]^{3/2}} \quad (2.11)$$

which is identical to  $b_n$  near the droplet apex, leading to the following relation

$$b_n = \frac{\frac{d^2 z^*}{dx^{*2}}}{\left[ 1 + \left( \frac{dz^*}{dx^*} \right)^2 \right]^{3/2}} . \quad (2.12)$$

For every point on the interface the minimum Euclidian distance between the experimental  $I = (x_i, z_i)$  and Young–Laplace droplet shapes  $YL = (x_j, z_j)$  was calculated by the minimum of

$$\psi = \sum d_i \quad (2.13)$$

where  $d_i = \sqrt{(x_i - x_j)^2 + (z_i - z_j)^2}$  is used to denote the distance measured at specific positions  $i$  along an axis of the independent variable at minimization step. The minimum of  $d_i$ , denoted as  $\delta$ , is shown schematically in Figure 2.6. The sum of all  $\delta$  gives the value  $\psi$ . Figure 2.5 (c) shows the plot of the set of right half interfacial coordinates from the image (black color)  $I_R = (x_r, z_r)$ . The curvature (red color) near the apex from Eq. (2.12) fitted to  $I_R = (x_r, z_r)$  at the minimum  $\psi$ . The interfacial tension can be obtained by solving Eqs. (2.8)-(2.10) with the curvature  $b_n$  at the apex by minimizing  $\psi$ . Figure 2.5 (d) shows that Eqs. (2.8)-(2.10) with the best fitted curvature  $b_n$  generates the droplet shape  $YL = (x_j, z_j)$  marked as red dots which was fitted to the  $I_R = (x_r, z_r)$  to get the interfacial tension  $\gamma_{ll}$ . As shown in Figure 2.7 (a)-(b), the best fit of  $b_n$  was analyzed by minimizing the sum of minimum Euclidian distance  $\psi$ . At the minimum value of  $\psi = 0.3 \cdot 10^{-5}$ , the  $b_n = 870 \text{ mm}^{-1}$  which is used to find the interfacial tension. The plot of  $\psi$  for the iterated interfacial tension  $\gamma_{ll}$  are shown in Figure 2.7 (c)-(d). At the minimum value of  $\psi = 0.4 \cdot 10^{-5}$ , the interfacial tension was analyzed as  $\gamma_{ll} = 0.0453 \text{ N/mm}$  which is comparable with the electrically deformed droplet shape method described above and support  $\gamma_{ll} = 0.0482 \pm 0.002 \text{ N/m}$  [55].

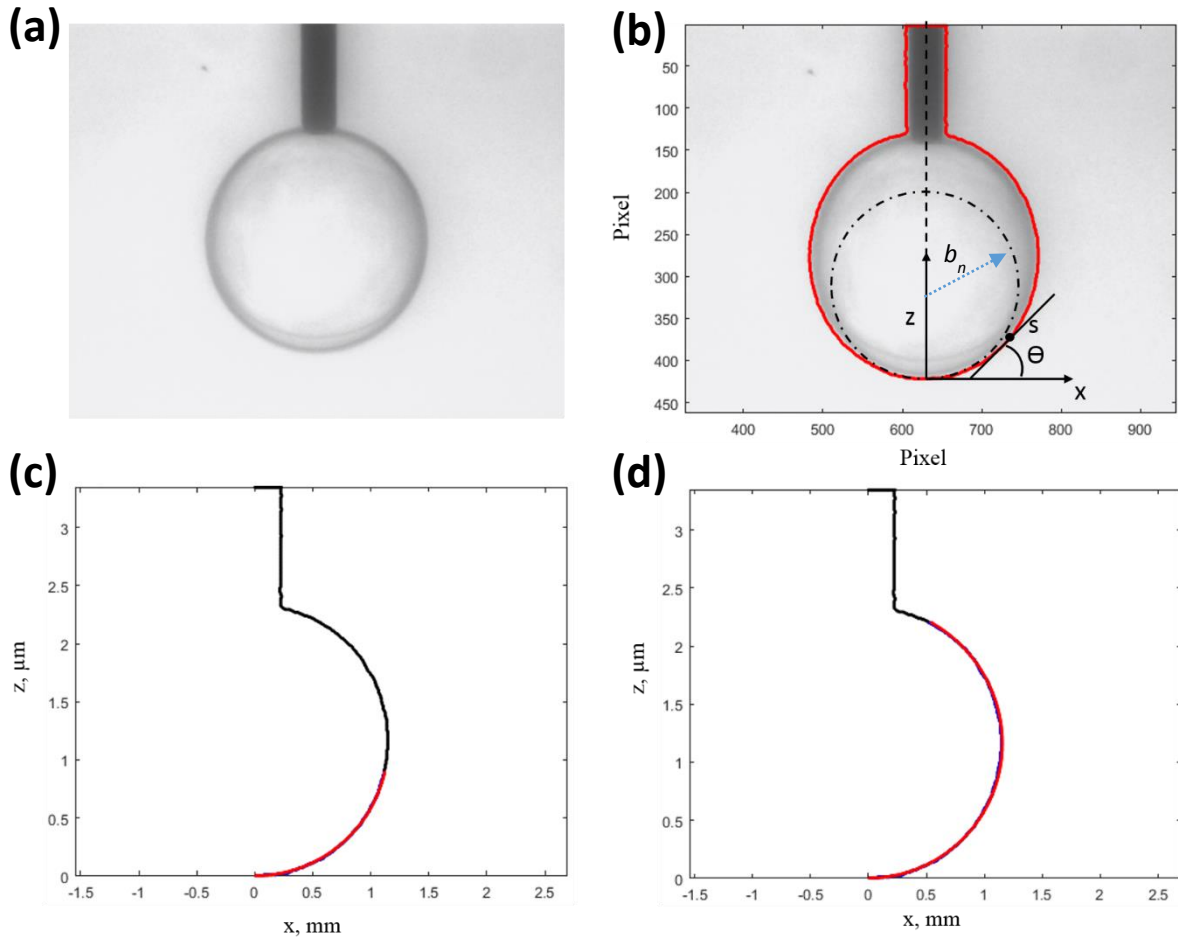


**Figure 2.5** (a) Image of a pendant droplet in 10000 cSt silicone oil. (b) Water-oil interface traced by image analysis marked as red line. (c) Eq. (2.12) for the curvature fit to the set of right half interfacial coordinates  $I_R = (x_r, z_r)$  from the image (black color) by minimizing  $\psi$ . (d) Eqs. (2.8)-(2.10) with the best fitted curvature  $b_n$  generated the droplet shape  $YL = (x_j, z_j)$  marked as red dots which was fitted to the  $I_R = (x_r, z_r)$ .

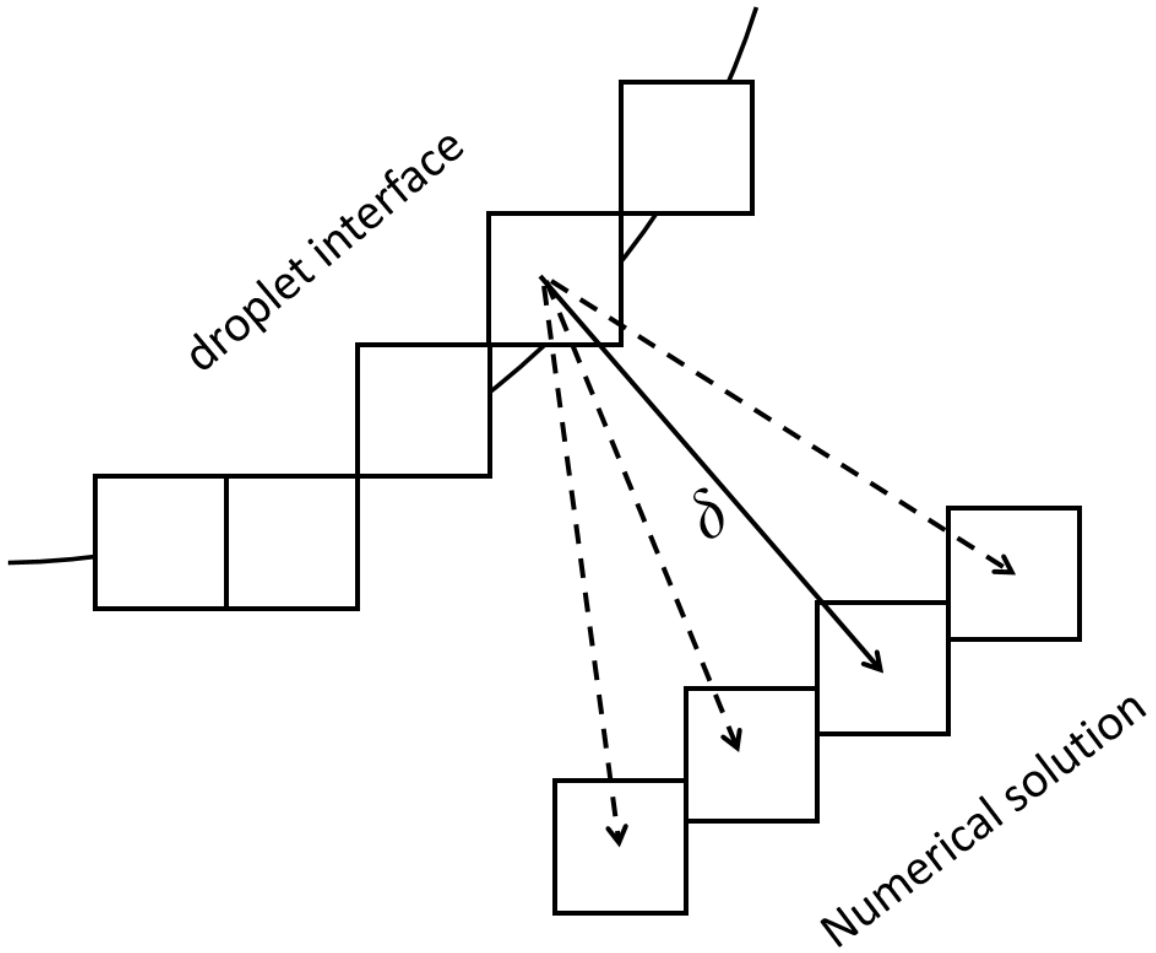


**Figure 2.6** Schematic view of the method to calculate the minimum Euclidian distance  $d_i$  between the experimental  $I = (x_i, z_i)$  and Young–Laplace droplet shapes  $YL = (x_j, z_j)$ .

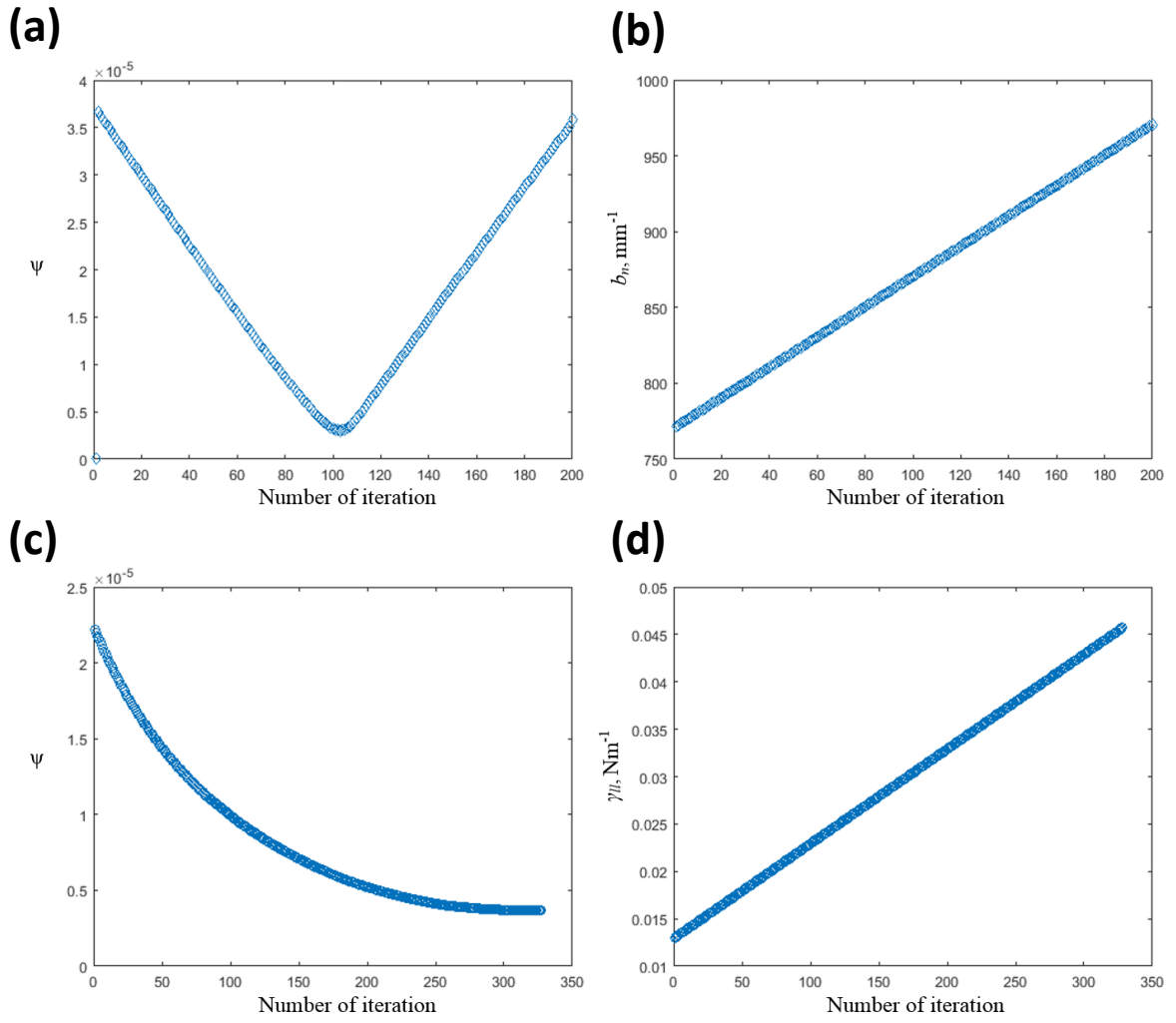


**Figure 2.7** (a) Plot of  $\psi$  are shown for the iterated radius of curvature (b)  $b_n$  at the apex. (c) Plot of  $\psi$  are shown for the iterated interfacial tension (d)  $\gamma_{II}$ .

## Chapter 3. In situ Emulsification in a Non-uniform Alternating Electric Field

### 3.1 Introduction

Methods of electrically assisted emulsification are of interest for various applications [31,48,59-62]. Electrically induced breakup of electrified liquid jets is widely used in modern electro spraying technologies [63,64]. Electro sprays in dc mode and electric forces applied to electrified liquid surfaces were described in classical works of Zeleny [25] and Taylor [2]. Electro sprays under ac electric fields have been studied and demonstrated stability in a range of applied frequencies from 1 to 400 kHz [65,66]. Methods similar to a classical electro spray in liquid-in-gas systems were applied for a controlled generation of emulsion drops using flow of one liquid in another. Sato et al. experimentally studied dispersion mechanisms in an oil-in-water system around the capillary nozzle tip [67]. Jets of conducting liquids were generated inside stationary liquids by Barrero et al. [68]. A microfluidic emulsification device by Kim et al. used electro spray in a flow focusing geometry [69] to generate submicron droplets in a Taylor cone mode. The tip of the cone was stretched to a narrow microjet and was broken into a plume of tiny droplets similar to what was previously observed for dc spraying of electrolyte solutions in air [62]. A few experiments in liquid-in-liquid system under an ac electric field have been conducted for emulsification [68-71].

The main factor controlling the breakup of dc electrified liquids is surface accumulated charges generating normal and shear electrical stresses [72-75]. Charged droplets generated in dc electro spray systems have the same polarity as the dispersing

electrode and rapidly move away from it. In contrast, ac electric fields can produce electrically neutral droplets. The formed droplets could be confined in the area near the electrode by a dielectrophoretic force acting on a dielectric placed in a non-uniform electric field [75,76]. In this work, this approach was used for in situ emulsification of small water droplets immersed in a continuous oil phase.

### 3.2 Experimental

The emulsification studies were performed in a glass cuvette with a height of 45mm and a square cross section of 12mm by 12mm (Fig. 3.1a). The cuvette was placed on a grounded plate that served as the first electrode. A stainless steel needle with the outer diameter of 0.3mm and blunt tip served as the second electrode. The needle was positioned along the cuvette axis with the tip located at a distance of 3.4 mm from the cuvette bottom. The cuvette was filled with 3 ml of castor oil with the conductivity  $\sigma_{co} = 10^{-7}$   $\mu\text{S/cm}$ , dielectric constant  $\epsilon_{co} = 3.8$ , viscosity  $\nu_{co} = 850$  cSt, and surface tension  $\gamma_{co} = 29$  mN/m. Distilled water with a conductivity  $\sigma_w = 0.05$   $\mu\text{S/cm}$  was used as a dispersed phase to make water-in-oil emulsions. At the beginning of each experiment, a water droplet with a volume of 5  $\mu\text{l}$  was placed on the bottom of the cuvette under the tip of the needle electrode (Fig. 3.1a).

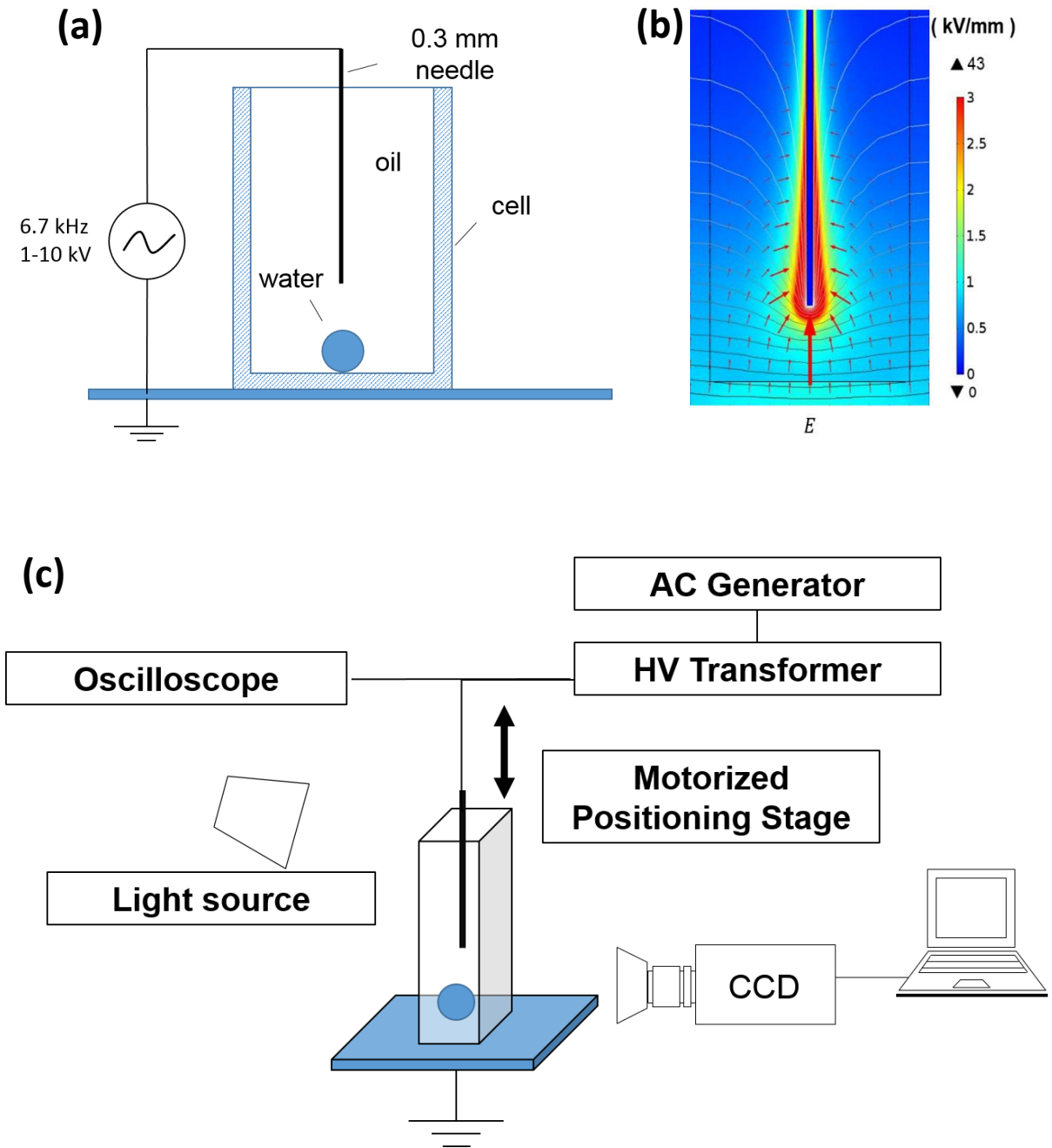


**Figure 3.1** Water-in-oil emulsification using a non-uniform ac electric field. (a) Schematic of the glass cuvette with the needle electrode. (b) Electric field distribution and equipotential line in the cuvette filled with the castor oil at an instantaneous electric potential of  $-10.5$  kV (Comsol Multiphysics). (c) Layout of the experimental setup.

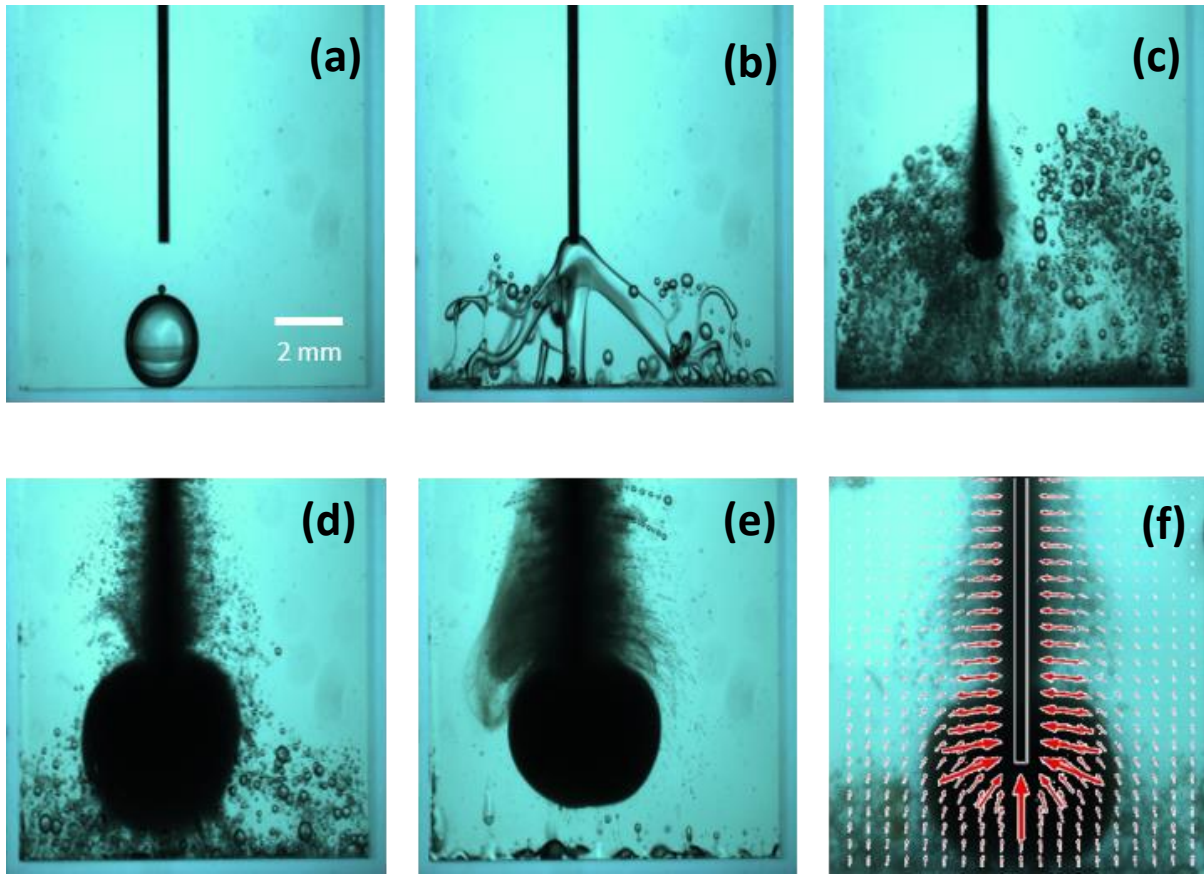
Complete experimental layout is shown in Figure. 3.1 (c). Ac power generator (Model MAC-01A, Compact Power, Inc.) with a high voltage transformer was used as a voltage source. The voltage waveform was monitored using a Tektronix oscilloscope (Model TDS 2024B). A CCD camera (Model PLB954, Pixelink, Inc.) equipped with a scientific grade zoom lens (Model 125, Optem, Inc.) was used to capture a droplet dynamics during the emulsification process. The generated emulsions were characterized using an optical microscope (Model TC5400, Meiji Techno Co.).

### 3.3 Electric Field Distribution

A variable frequency (1–10 kHz) ac voltage (1–10 kV) was applied to the needle electrode. The cuvette walls formed a conductive barrier and only a small displacement current crossed the interelectrode space. The electrode geometry resulted in a strongly non-uniform electric field distribution near the needle tip and needle surface. Figure. 3.1 (b) shows numerical results of the electric field distribution simulated by COMSOL Multiphysics model in the cuvette filled with the castor oil at an instantaneous electric potential of ~10.5 kV. Electric fields of ~40 kV/mm and strong electric field gradients exist near the needle surface. It is expected that the dielectrophoretic (DEP) force is directed along the electric field square gradients,  $F_{DEP} \sim \nabla E^2$ .

### 3.4 Characteristic Dispersion Sequence

Figure. 3.2 shows a dispersion sequence for a water droplet placed at the bottom of the oil-filled cuvette energized by ac voltage at 7.4 kV and 6.7 kHz. The applied voltage generated a strong dielectrophoretic force. As a result, the water droplet was immediately attracted toward the needle electrode. The droplet in contact with the needle experienced high electrically induced stresses on its outer surface. As a result, thick water channels protruded from the droplet in different directions (Fig. 3.2b). The channels were further disintegrated into relatively large droplets that in turn were attracted to the needle by the dielectrophoretic forces. After only 10 s the cuvette was filled with a cloud of small and large water droplets with the small droplets accumulated in the region close to the needle where the electric field was very strong (Fig. 3.2c). After this, the process was continued at microscale. The droplets were constantly entrained into the area of high electric field and dispersed. At 90 s, the formed emulsion was mostly contained near the needle electrode (Fig. 3.2d). After 600 s, a quasi-steady distribution of the emulsified droplets was observed (Fig. 3.2e). A dense cloud containing water-in-oil emulsion was formed. One part of the cloud was shaped as a sphere attached to the end of the needle electrode. The other part was accumulated along the outer surface of the needle.



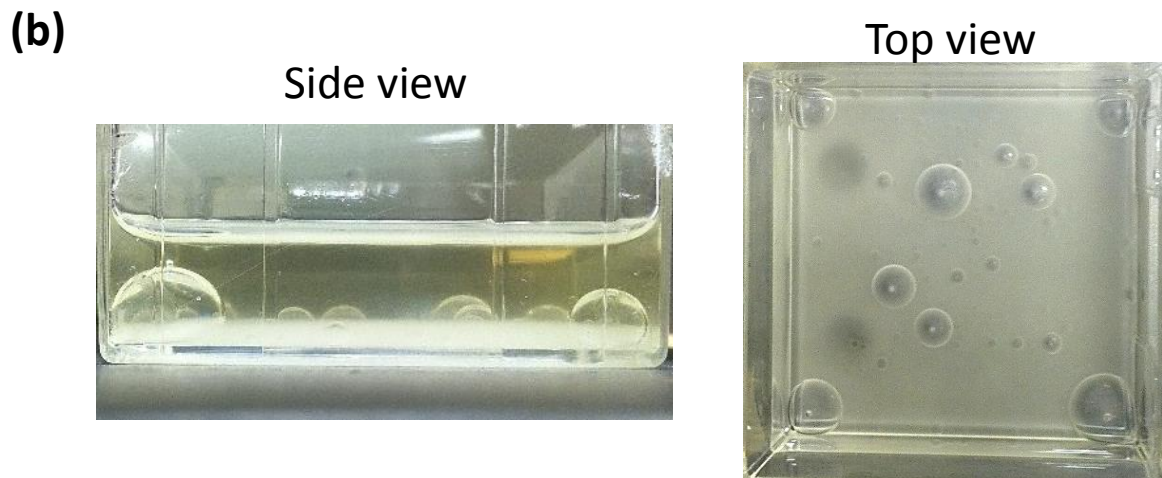
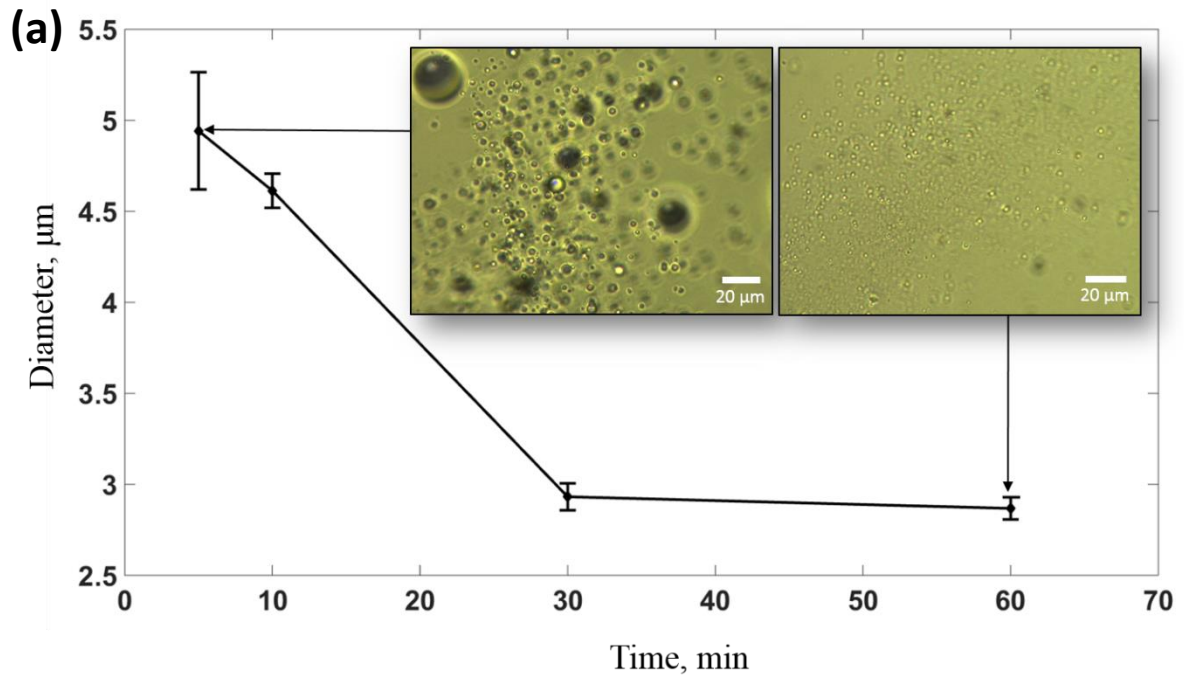
**Figure 3.2** Dispersion sequence of water-in-oil emulsification at 7.4 kV with 6.7 kHz at the processing times: (a) 0 s, (b) 1s, (c) 10 s, (d) 90 s, (e) 600 s. (f) Quasi-steady distribution of the emulsion with superimposed arrows representing the relative magnitude and the direction of the electric field.

Figure. 3.2 (f) shows that the shape of the cloud closely resembles the distribution of the electric field near the needle electrode obtained for the cuvette filled with the castor oil (Fig. 3.1b). It should be noted that the electric field distribution is altered by the presence of the high density water emulsion. The electric field in the cloud is expected to decrease due to increasing of the average dielectric permittivity of the media. The droplets inside the cloud are attracted to the needle by the dielectrophoretic force. A value of the dielectrophoretic

force [77,78]  $F_{DEP}$  depends on the droplet diameter  $d$ , and the gradient of the electric field  $E$  as  $F_{DEP} \sim d^3 \nabla E^2$ . The large droplets experience larger dielectrophoretic force and are preferentially entrained in the high field area where they are dispersed into smaller droplets. It should be noted that for certain conditions, when one fluid has a greater electrical conductivity and another has a greater dielectric constant, the dielectrophoretic force can change sign depending on an applied frequency [79,80]. This cross-over effect was not observed in water-in-castor oil system with  $\sigma_w \gg \sigma_{co}$  and  $\epsilon_w \gg \epsilon_{co}$ .

### 3.5 Emulsified Droplet Diameter

More insights on the properties of the formed suspension were obtained by measuring the average droplet diameters. Because of the high density of the suspension, these measurements were performed using an optical microcopy on extracted suspension samples. Figure. 3.3 (a) shows a variation of the average droplet diameter as a function of the processing time. The insets in Figure. 3.3 (a) are the light microscopy images of emulsified water droplets formed at 5 min and 60 min. Figure. 3.3 (a) shows the average droplet diameter is practically constant after 30 min of processing time suggesting formation of quasi-steady distribution of emulsified droplets. A photo image of the droplet cloud taken 24 h after the experiment (Fig. 3.3b) confirms the high stability of the formed emulsion.



**Figure 3.3** (a) Average droplet diameter as a function of the processing time at 7.4 kV with 6.7 kHz. The insets are the optical microscope images of the droplets extracted from the near the needle at 5 min and 60 min. (b) Side and top view of the emulsion after sedimentation for 24 hours.

At long processing times, the average diameter of the water droplets was approaching  $\sim 3 \mu\text{m}$ . The droplets were produced with a narrow size distribution with a standard deviation

of  $\sim 0.55 \mu\text{m}$ . The minimum diameter of the droplets achieved in the experiments can be analyzed based using the interfacial tension  $\gamma_{il}$ , applied ac frequency  $f$ , and induced electrical stresses.

It is interesting to evaluate a fundamental natural frequency  $f_n$  of emulsified water droplets. In the inviscid case,  $f_n$  is given by the Rayleigh-Lamb relationship [81,82] as

$$f_n = \left( \frac{48\gamma_{il}}{(3\rho_w + 2\rho_o)\pi^2 d^3} \right)^{1/2} \quad (3.1)$$

where  $\rho_w$  and  $\rho_o$  are the densities of water and oil, respectively. For water in castor oil system,  $\gamma_{il}$  can be evaluated [83] as 51.5 mN/m (using image analysis with axisymmetric pendant droplet technique). Then, for the initial drop with  $d = 2 \text{ mm}$ ,  $f_n$  is equal to 81 Hz and for  $d = 2 \mu\text{m}$   $f_n$  is  $\sim 3 \text{ MHz}$ . At some moment in the dispersion process, there might be a resonance between  $f_n$  and  $f$ . However, this effect could be strongly affected by the high viscosity of the castor oil.

The evaluation of electrical stresses requires evaluation of charge relaxation frequencies. A charge relaxation frequency of the deionized water  $f_w$  can be evaluated as  $\sigma_w / (\varepsilon_0 \varepsilon_w) = 7.8 \text{ kHz}$ , where  $\varepsilon_0$  is vacuum permittivity. The charge relaxation frequency of the water is close to applied ac frequency in our experiments. At the same time, a charge relaxation frequency of the castor oil  $f_o \ll f \approx f_w$ . In these conditions, a minimum diameter of the formed water droplet can be evaluated from the inequality [2,72]  $Ca_E^* = d\varepsilon_0 \varepsilon_{co} E^2 / 2\gamma_{il}$ .

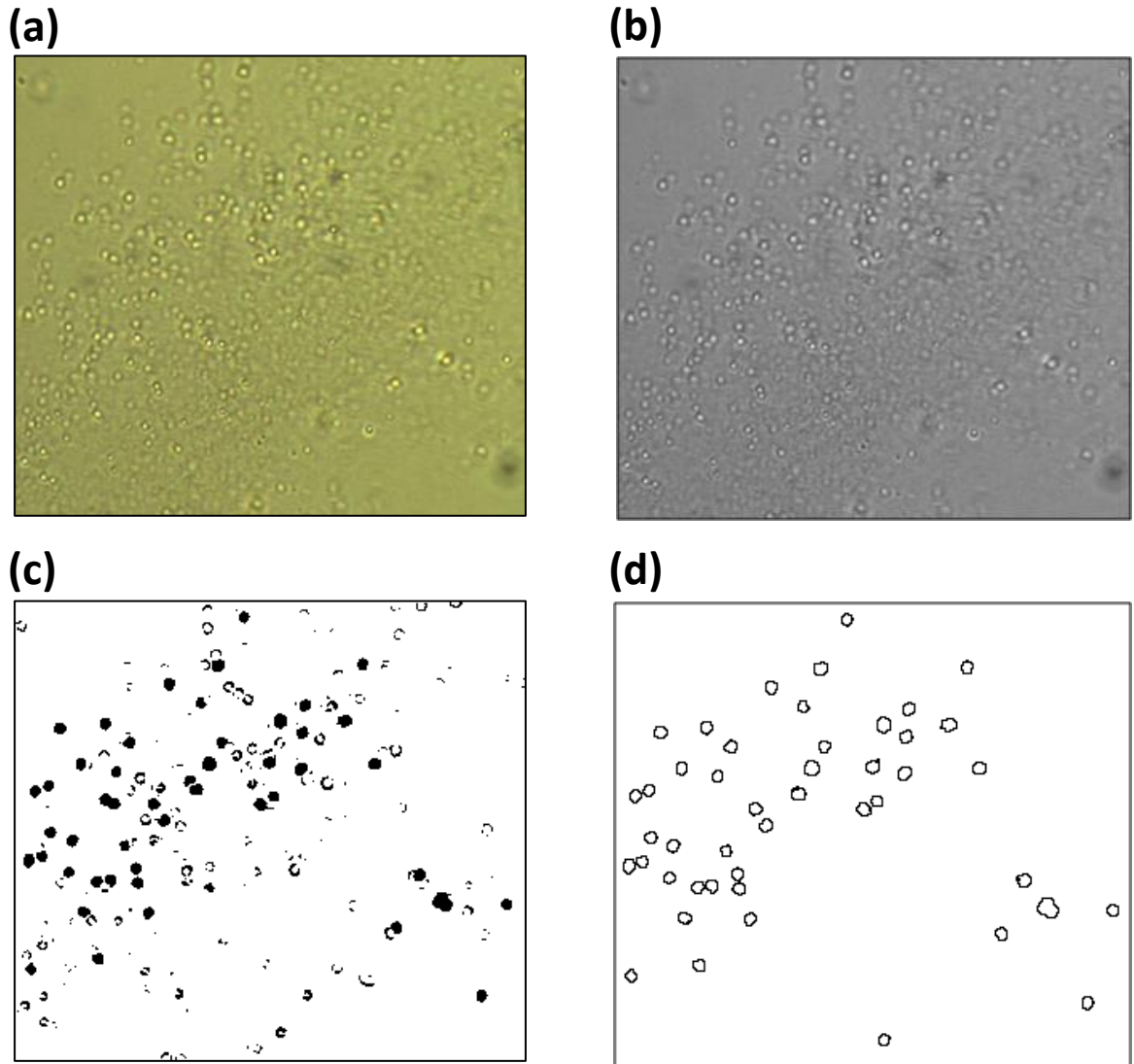


**Figure 3.4** Emulsified water droplets image analysis. (a) Image captured from the optical microscope. (b) Converting to mono color. (c) Creating binary image. (d) Removing noise mark.

Additional experiments were performed to study the effect of the electric field  $E$  on the average diameter of emulsified water droplets. In these experiments, different electric potential was applied for 60 minutes with the same experimental procedure. A pipette was used to pick a sample in the middle of suspension cloud and then dispensed it on a

microscope slide. This slide is then taken to a microscope where images of the microdroplets can be scanned for the uniformity and recorded. Image analysis is then applied to each of the collected images of the emulsion. This image processing changes the image from an RGB color image (Fig. 3.4a) into an 8 bit mono image (Fig. 3.4b). A threshold is then applied to the image to create a binary image (Fig. 3.4c-d). This image processing method eliminates out of focus droplets and other particles which are not of interest in the study. From these areas the diameters can be calculated assuming each droplet is a perfect circle. The end result is a file which includes droplet number area and calculated diameter. From the associated number the droplet can be traced back to the image. This allows anomalies to be connected back to the image. The image processing and calculation is continued until a sufficient number of droplets have been sampled. This process is repeated over four series using electric potential values in a range from 4 kV to 10 kV.

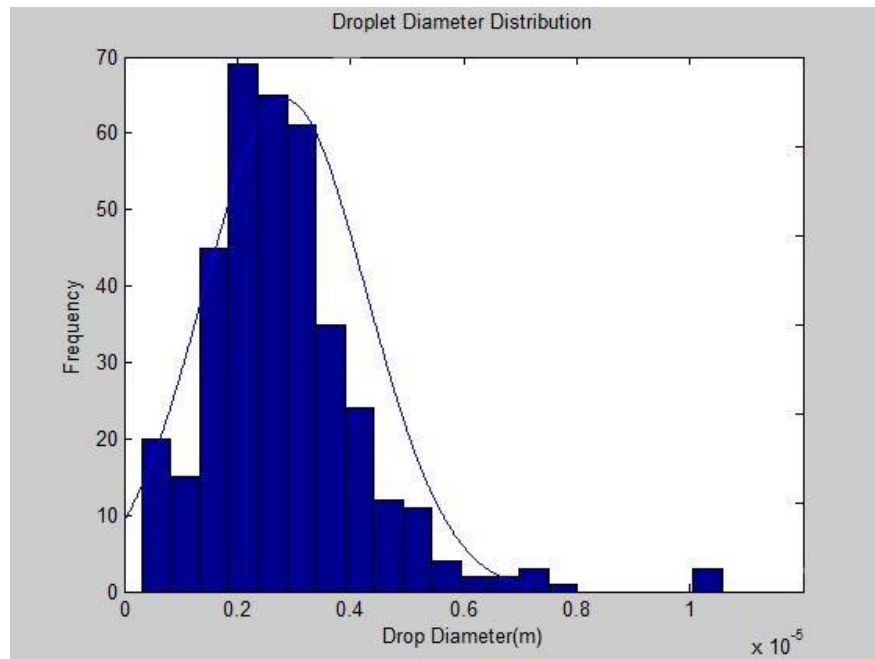


**Figure 3.5** Diameter distribution of microdroplets at 6.4 kV at 6.7 kHz.

A distribution of the diameters of the emulsion is plotted at 6.4 kV in Figure 3.5. This quasi-steady distribution is reached at least by one hour after the electric potential is applied. It is compared with the normal distribution curve for the same distribution with equal averaged diameter and standard deviation. The evaluated droplet diameters with different electric potentials are listed in Table 3.1. The maximum electric fields  $E_{\max}$  were simulated by COMSOL Multiphysics model in the cuvette filled with the castor oil at the different electric potentials. The maximum electric field  $E_{\max}$  was used to analyze the theoretical diameter.

**Table 3.1** Experiments at 6.7 kHz were performed to study the effect of the electric field  $E$  on the average diameter of emulsified water droplets.

Electric potential	Maximum electric field $E_{\max}$ (COMSOL Multiphysics)	Average diameter $d$
7.4 kV	30.4 kV/mm	0.0025 mm
6.4 kV	26.3 kV/mm	0.0028 mm
5.0 kV	23.1 kV/mm	0.0039 mm
3.5 kV	20.2 kV/mm	0.0064 mm

The critical capillary number,  $Ca_E^* = 0.21$ , is used to calculate the theoretical diameter of the micro droplets with respect to a uniform electric field

$$0.21 = d \varepsilon_0 \varepsilon_{co} E^2 / 2\gamma_{ll} \quad (3.2)$$

where  $\gamma_{ll}$  is the water-oil interfacial tension. Manipulation of the equation solving for the diameter yields the following:

$$d = 0.21 \frac{2\gamma_{ll}}{\varepsilon_0 \varepsilon_{co} E^2} \quad (3.3)$$

$$d = 0.6429 \cdot 10^{-3} / E^2 \quad (3.4)$$

where  $d$  is in  $\mu\text{m}$  and  $E$  is in  $\text{kV/mm}$ .

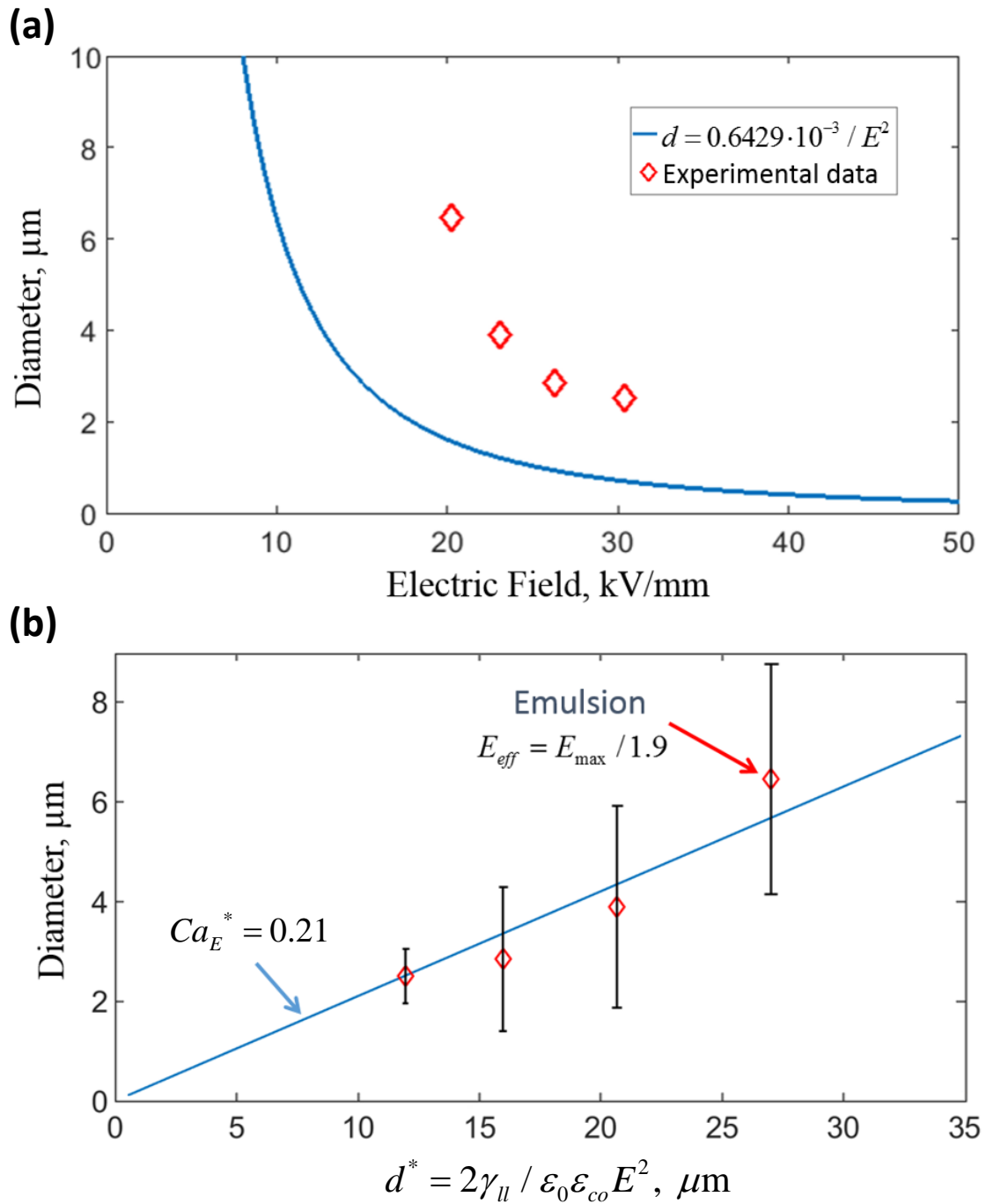


**Figure 3.6** (a) Theoretical (Eq. 3.4) and experimental diameter of microdroplets plotted against the electric field. (b) Critical electrical capillary constant plot adjusted by  $E_{eff} = E_{max}/1.9$ .

The theoretical diameter of microdroplet in Eq. (3.4) plotted to compare to the experimental diameter of microdroplets in terms of the maximum electric field  $E_{\max}$  listed in Table 3.1 in Figure 3.6 (a). There is an apparent shift in magnitude of the experimental diameter compared to the theoretical diameter. The primary causes of this are attributed to the fact that the maximum electric field values were used to plot the experimental data points. Another possible factor that could be a cause of the shift in the experimental data is that in the Multiphysics software pristine castor oil was used in the calculation of the electric field. In practice the electric potential across the two electrodes will be screened by the emulsion [84].

The theoretical diameter of microdroplet in Eq. (3.4) can be rearranged in terms of a characteristic length  $d^* = 2\gamma_{ll} / \epsilon_0 \epsilon_{co} E^2$ , leading to

$$d = 0.21d^* \quad (3.5)$$

where the critical capillary number  $Ca_E^* = 0.21$  is a slope and the characteristic length  $d^*$  is a dependent variable. Figure 3.6 (b) shows the theoretical diameter of microdroplet with respect to the characteristic length  $d^*$  in Eq. (3.5). The experimental diameter of microdroplets in terms of  $d^*$  was compared to the Eq. (3.5) and fitted by changing  $E_{\max}$ . A good fit between the experimental and theoretical values happened when  $E_{eff} = E_{\max}/1.9$  (Fig. 3.6b). This can be seen in the plot above where the new  $E_{eff}$  is used in place of  $E_{\max}$ . As the electric field between the pin and plate electrodes is increased the diameter of the microdroplets decreases. This is supported experimentally and theoretically.

### 3.6 Shape of Emulsion and Emulsion Properties

The existence of the sharp boundary of the suspension is quite remarkable (Fig. 3.8a). It makes the suspension look like a pendant droplet suspended on the end of the needle. If the continuity of the electric displacement field is assumed across the suspension boundary then the electric field inside the boundary  $E_e$  and the electric field immediately outside the boundary  $E_{co}$  are related as

$$\varepsilon_{co} E_{co} = \varepsilon_e E_e \quad (3.6)$$

It is expected that the dielectric permittivity of the suspension  $\varepsilon_e$  is greater than the dielectric permittivity of the oil  $\varepsilon_{co}$  [84]. As a result  $E_{co} \gg E_e$  and the strong electric field gradient across the suspension boundary results in the strong dielectrophoretic confinement force. The emulsion cloud hanging on the needle electrode is shaped as a sphere. Assuming the sphere radius of 2 mm and the average droplet diameter of 3  $\mu\text{m}$ , it is possible to evaluate that  $\sim 2 \cdot 10^9$  droplets will fit into the sphere by close-packing of equally sized spherical droplets [85]. At the same time, the initial water droplet can break into  $\sim 3 \cdot 10^8$  droplets with 3  $\mu\text{m}$  diameter. This suggests that the density of droplets in the cloud is extremely high and approaches  $\sim 15\%$  from the maximum possible value. The shape of the cloud (Fig. 3.7a) closely resembles the distribution of the electric field square  $E^2$  simulated by COMSOL Multiphysics for the cuvette filled with the castor oil (Fig. 3.7b) owing to the dielectrophoretic force  $F_{DEP} \sim \nabla E^2$ .

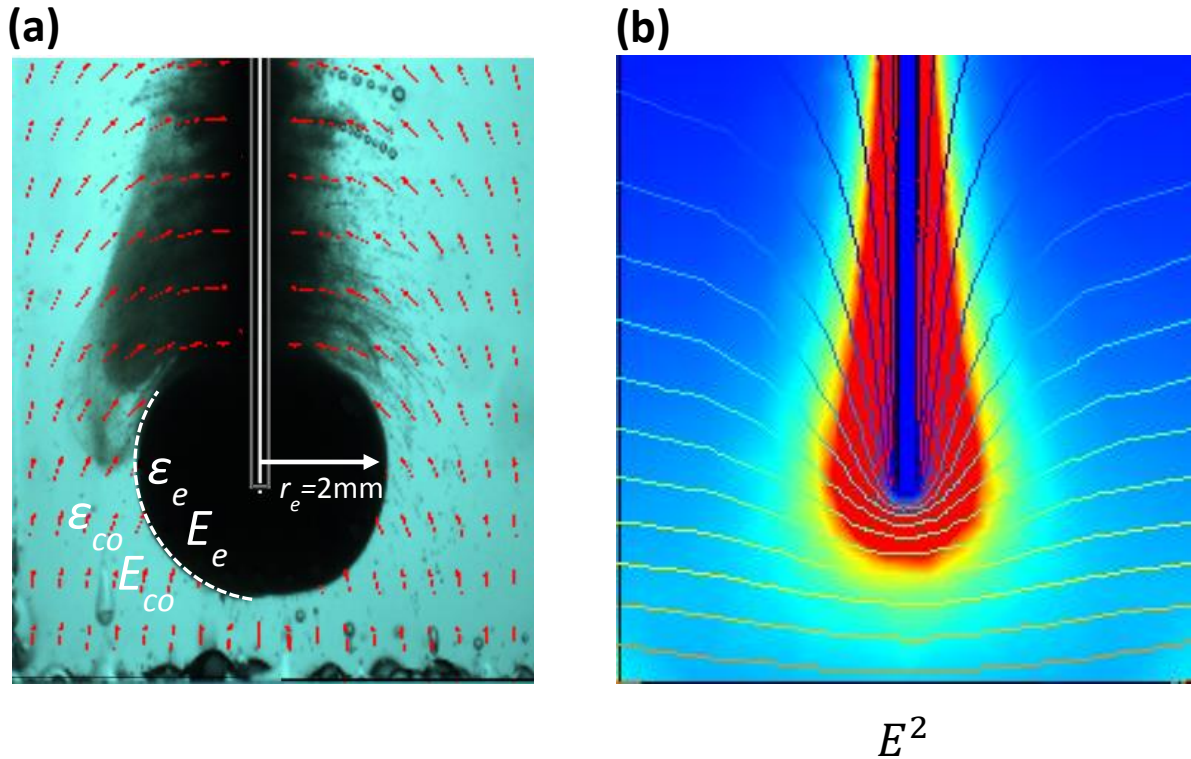


**Figure 3.7** (a) Image of emulsion cloud. Sharp boundary of the suspension is observed. (b) Electric field square distribution near the needle electrode (COMSOL Multiphysics).

### 3.7 Mechanisms of Droplet Break-up

An initial breakup of a large droplet was studied in a special experimental arrangement. A droplet with a diameter of 5mm was placed near the needle electrode powered by ac voltage at 4.2 kV and 6.7 kHz. The droplet breakup sequence is shown in Fig. 3.8. After the voltage was applied, the initially spherical still droplet (Fig. 3.8, 0 s) was attracted to the surface of the needle. During the motion, the droplet was deformed to compensate non-uniform electrically induced stresses acting on its surface (Fig. 3.9, 0.9 s). As a result, the front of the droplet directed to the needle had the highest surface curvature and the lateral sides of the droplet had the lowest one. At ~1 s, the front surface of the droplet came in contact with the

needle electrode. At this moment, the uncompensated electrical stress acting on the back surface started to elongate the droplet transforming it into the long cylinder (Fig. 3.9, 2.6 s). After reaching the critical diameter, the cylindrical channel started to disintegrate under the interfacial tension forces (Fig. 3.9, 7.2 s\_8.3 s) forming water droplets with diameters from 0.1mm to 1 mm.

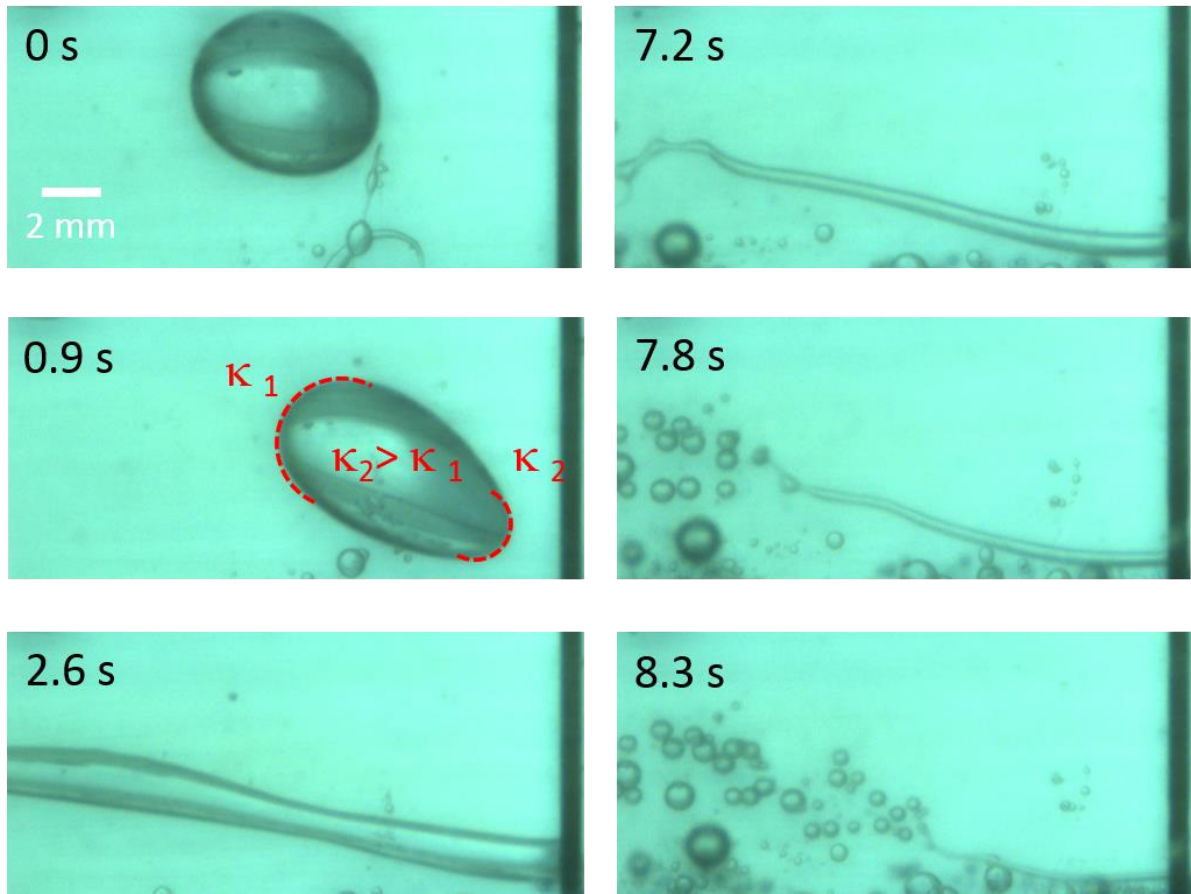


**Figure 3.8** Sequential images showing initial breakup of a large droplet placed in the oil near the needle electrode powered by ac voltage at 4.2 kV with 6.7 kHz. Numbers represent recording times.

The initial breakup of the droplet was followed by continuous emulsification on the microscale level. We identified three distinctive mechanisms responsible for further dispersion of the emulsified water droplets shown in Figure. 3.9.

The first mechanism involves small and large water droplets in contact with the needle electrode that continue to disintegrate through elongation into cylindrical channels followed by capillary break up. Figure 3.9 (a) illustrates this mechanism for small and large drops. The second mechanism includes breakup of the droplets at the surface facing the needle electrode. As a result, a jet of tiny droplets stemming from the surface is observed. In Figure 3.9 (b), the droplets in regions 1 and 2 are electrospaying tiny droplets into the needle electrode. It is possible to assume that a mechanism of electrospaying from a single droplet is similar to ac electrospaying from a pendant drop attached to an electrode [65,66]. According to the third mechanism, stable bead-like chains of water droplets are formed in the continuous phase [74,86]. Individual water droplets in the chain are interconnected by the thin liquid bridges (Fig. 3.9c). One end of the chain is usually connected with the needle electrode. At low voltages, chains can be stabilized for infinite time. At higher voltages, chains are stable only for short time intervals and disintegrate at the bridges to form tiny droplets. A charge transfer through the thin liquid bridges connecting the droplet beads plays an important role in balancing the radial stresses induced by the interfacial tension [74,86]. The bead-like structures were affected by the magnitude and frequency of the applied voltage. The lengths of the liquid bridges and the size of the water droplet beads were decreased with the frequency increase.

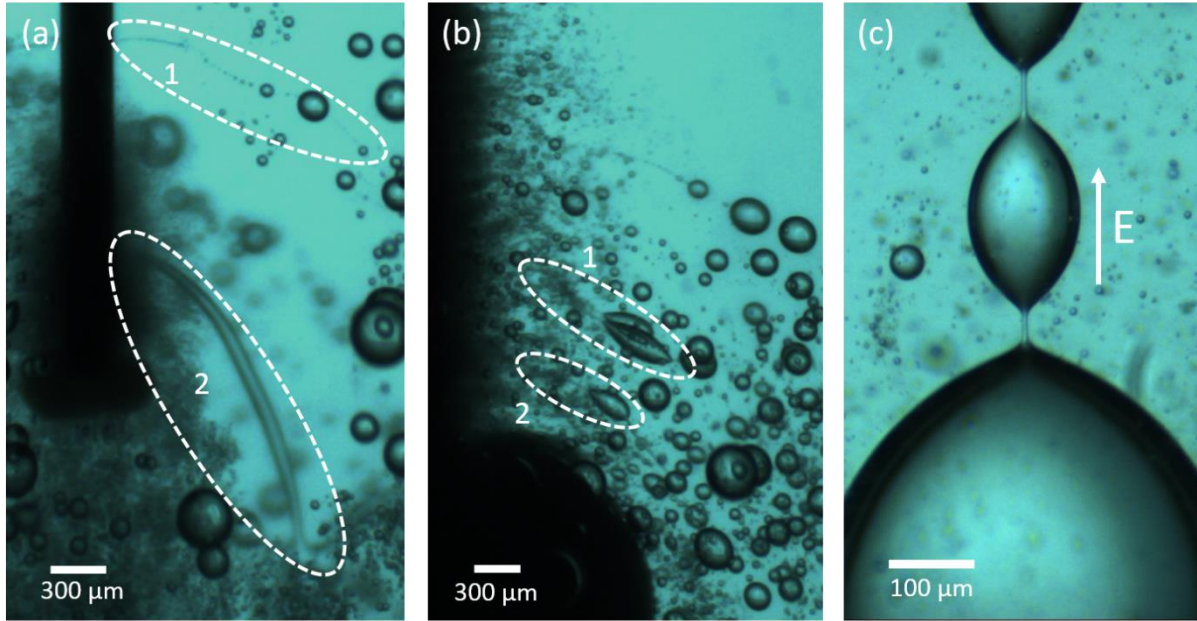


**Figure 3.9** Microscale mechanisms of water droplets breakup. (a) Small 1 and large 2 droplets in contact with the needle electrode are disintegrated by elongation and capillary breakup. (b) Droplets in regions 1 and 2 electro spraying inside the continuous phase. (c) Thin liquid bridges formed between droplets sustain the droplet chains aligned with the direction of the electric field. Under certain conditions, the bridges disintegrate to form tiny droplets.

The chain structures resemble the bead-and-string configurations observed during iterated stretching of viscoelastic jets [87]. However, in our experiments, the stretched jets are

composed of deionized water, which is a Newtonian fluid. As such, viscoelasticity is not of significance and the electric field is expected to play a major role in the chain formation. A mechanism of chain formation can be qualitatively understood considering a small droplet connected to the needle electrode. When  $f < f_w$ , the droplet and the needle electrode form the equipotential surface. A strong gradient of the electric field near the attached droplet creates dielectrophoretic force affecting droplets dispersed in the continuous phase. As a result,

another droplet is attracted to the initial droplet. However, the droplets could not merge. Indeed, if a large area of contact is established between the droplets, a charge transfer occurs between the droplets with equalizing the potentials and the attraction is changed to the repulsion, as shown in Figure 3.9. So, the interaction between the droplets occurs through jetting or bridging with a partial charge transfer. In some cases, thin stable bridges connecting the droplets can be formed [74,86]. A sequential addition of the droplets can create chains aligned in the direction of the electric field. Overall, the mechanism of chain formation is intriguing and merits further studies.

### 3.8 Comparative Analysis of Emulsification in DC and AC

An emulsification of a water droplet in castor oil in a DC electric field was studied. The experimental system is the same as the AC emulsification shown in Figure 3.1 (a) with DC power voltage at 7.4 kV. The droplet breakup sequence is shown in Figure 3.10. After the voltage was applied, the initially spherical droplet (Fig. 3.10a) was immediately attracted to the surface of the needle owing to a strong dielectrophoretic force. The droplet in contact with the needle experienced high electrically induced stresses on its outer surface. As a result, the initial droplet was broken into a main droplet with smaller droplets (Fig. 3.10b). During the process, the droplet was charged and then, had the same polarity as the dispersing electrode in DC. As a result, the droplet rapidly moved away from the needle with disintegrating small droplets. This is compared to the phenomena in AC emulsification, where the front surface of the initial droplet in contact with the needle electrode protruded

and further disintegrated into smaller droplets (Fig. 3.2b). The droplets in turn were attracted to the needle by the dielectrophoretic forces and again moved away from the needle with small disintegration after contacting the needle (Fig. 3.10c-e). Figure 3.10 (f) shows a distribution of the emulsion which confined well near the needle electrode with fine emulsion at 90 s in the AC electric field where electrically neutral droplets were produced (Fig. 3.2e). The relatively large droplets, however, were created in DC electric field at the same processing time 90 s shown in Figure 3.10 (e).

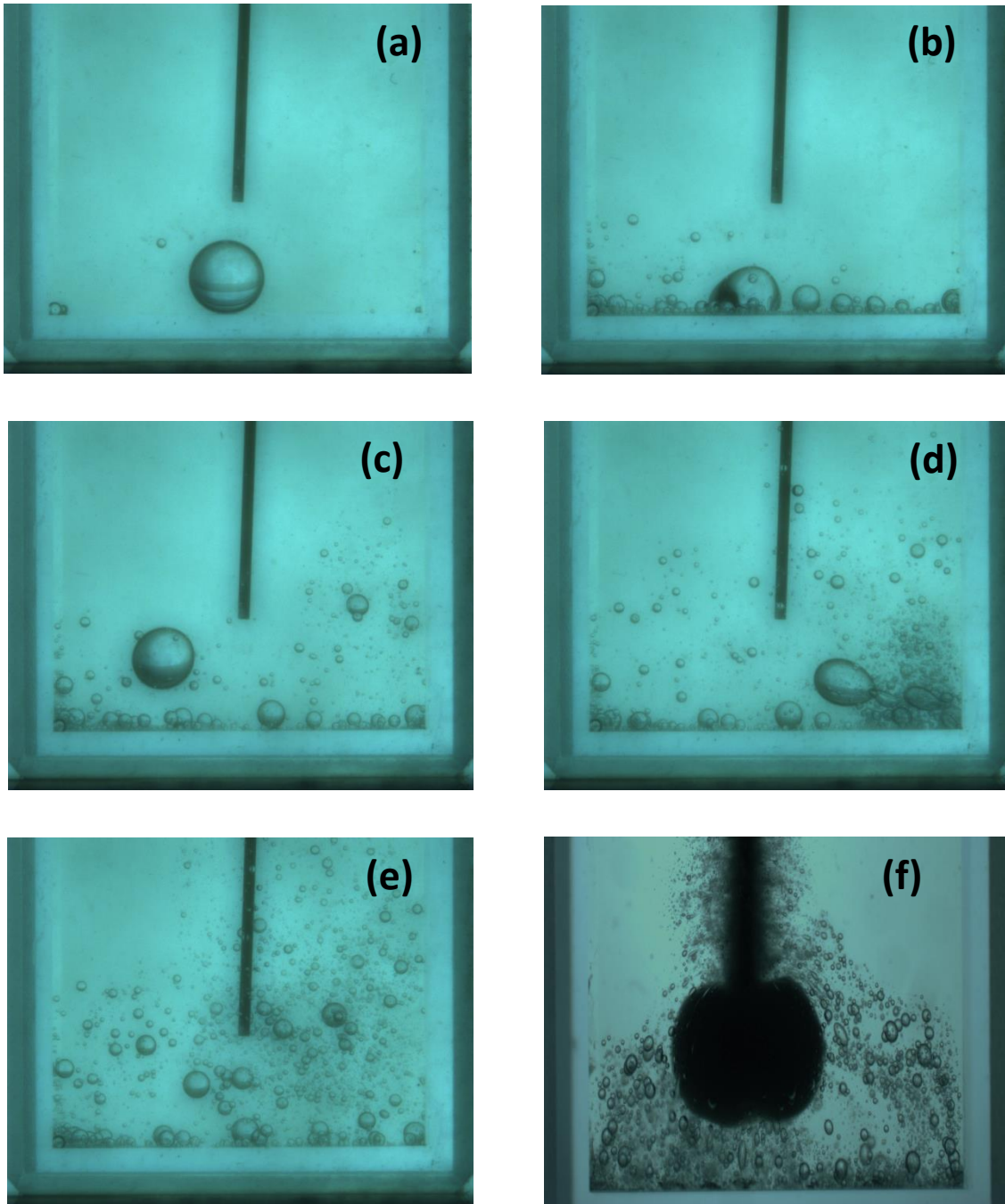


**Figure 3.10** Dispersion sequence of water-in-oil emulsification at 7.4 kV in a DC electric field at the processing times: (a) 0 s, (b) 1 s, (c) 10 s, (d) 50 s, (e) 90 s. (f) Distribution of the emulsion at 90 s in the AC electric field at the same experimental conditions.

## Chapter 4. Coalescence of Droplets in an Alternating Electric Field

### 4.1 Introduction

An excess energy of a fluid surface defines shape of individual droplets and free jets. The role of surface energy increases with transition to micro and nanoscale where electric fields have been successfully applied to balance surface effects in DC and AC electrosprays [25,60,64,88], electrospinning [89], droplet manipulation, breakup [2,40], emulsification [52,90], and electrically enhanced coalescence [74]. A conducting droplet freely suspended in an insulating fluid accepts spherical shape in the absence of an electric field. Upon application of the field, the droplet becomes elongated along the direction of the field and bursts at high electric fields. The droplet deformation and break up is controlled by the balance of surface tension and electric forces typically expressed in the form of the electrical capillary number  $Ca_E = d\varepsilon\varepsilon_0 E^2 / 2\gamma_{ll}$ , where  $\varepsilon_0$  is the permittivity of free space,  $\varepsilon$  is the relative permittivity of the liquid,  $E$  is the magnitude of the electric field,  $d$  is the diameter of the droplet, and  $\gamma_{ll}$  is the interfacial tension. A conducting droplet in a dielectric fluid breaks up when capillary number reaches the well-defined critical value of  $Ca_E^* = 0.21$  [2]. The effects of droplet and media conductivity, viscosity and dielectric permittivity on shape and stability of the droplet have been extensively studied [40].

The reverse process, coalescence of a droplet pair, is rich in physical effects and is a subject of continuous research efforts. The electric capillary number for a pair can be defined using the radius of the single spherical droplet with the equivalent total volume. At low capillary numbers the droplet attraction leads to complete coalescence [74]. At an

intermediate range of capillary numbers a non-coalescence [6,22] or a partial coalescence [7,91] of oppositely charged droplets is observed, when the droplets repel and bounce back from each other after contact and partial fluid and electric charge transfer. Theoretically, the complete coalescence of a pair is possible at  $Ca_E < Ca_E^*$ , however, the droplets in the pair often emit electrified jets and disintegrate well below  $Ca_E^*$  [91]. In this work, we report a phenomenon of oscillatory coalescence of water droplets. Two droplets situated in an alternating electric field coalesce through multiple repetitive stages of attraction, liquid bridge formation, fluid transfer, and repulsion. The goal of this study is to characterize this phenomenon, define its region of existence and uncover the underlying physical mechanisms.

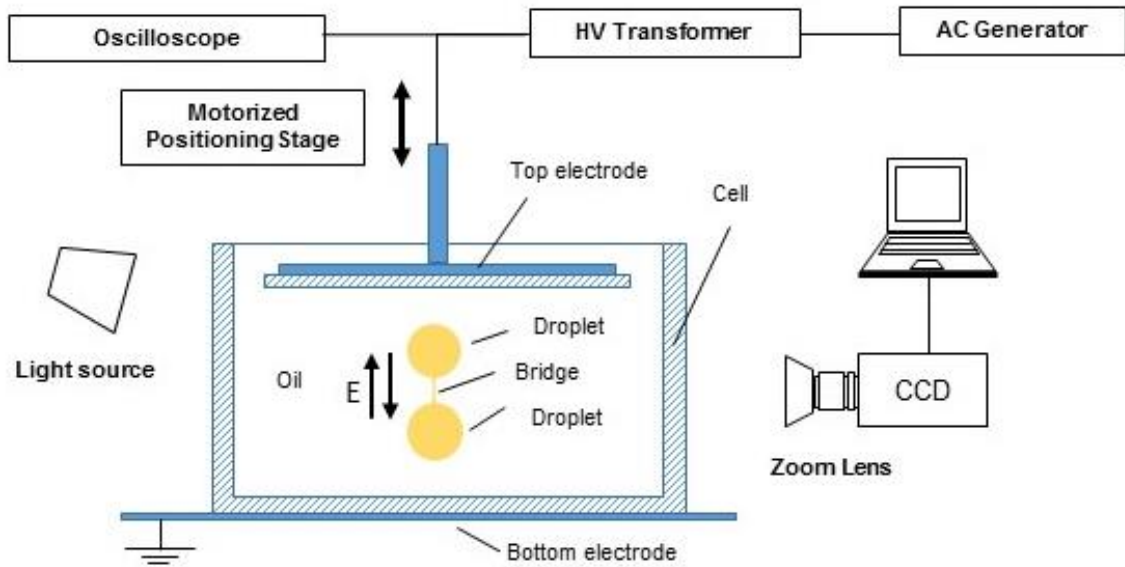


**Figure 4.1.** Schematic of the experimental setup.

## 4.2 Experimental

The experimental setup of a coalescence system is shown in Figure 4.1. A transparent rectangular acrylic cell with  $75 \times 53 \times 26 \text{ mm}^3$  [L×W×H] is used as an oil container. It has a relative permittivity of  $\epsilon_1 = 1.9$  and a thickness of  $h_1 = 1.7 \text{ mm}$ . The cell is placed on a grounded plate (bottom electrode) that served as the first electrode. A stainless steel planar electrode (top electrode) with  $31 \text{ mm} \times 31 \text{ mm}$  serves as the second electrode at which a acrylic plate with a thickness of  $h_2 = 1.3 \text{ mm}$  was attached. The top electrode parallel with the bottom electrode is positioned along the cell axis and adjusted with a motorized positioning stage. Distilled water is used as a dispersed phase. The conductivity of water  $\sigma_w$  is adjusted in the range from 0.5 to 235  $\mu\text{S/cm}$  (a conductivity meter is used, Model CON 400, OAKTON Co.) by salt addition. Ac power generator (Model MAC-01A, Compact Power, Inc.) with high voltage transformer is used as a voltage source and applied to the top electrode. The voltage wave form is monitored using an oscilloscope (Model TDS 2024B). The walls of acrylic cell play a role as a conductive barrier and have only a small displacement current across the interelectrode space. A CCD camera (Model PL-B954, Pixelink, Inc.) equipped with a scientific grade zoom lens (Model 125, Optem, Inc.) is used to capture droplet dynamics at a rate of 10 frames per second. Captured images are analyzed with custom MATLAB code to infer positions, shapes, and volumes of the droplets.

A pair of water droplets with the same conductivity is dispensed by micropipette in the middle of an oil-filled cell. The cell is filled with silicone oil with the conductivity  $\sigma_{so} = 10^{-11} \mu\text{S/cm}$ , kinematic viscosity  $\nu_{so} = 10000 \text{ cSt}$ , and relative permittivity  $\epsilon_{so} = 2.7$ . A droplet pair is characterized by radii of the top and bottom droplets  $r_1$  and  $r_2$ , the droplet size ratio  $\beta$

$= r_1/r_2$ , and the droplet volume ratio  $\alpha = V_1/V_2$ . The total volume of the droplet pair is fixed at 7.5  $\mu\text{L}$ . The initial volume ratio  $\alpha$  is set in an interval from 0.5 to 1.5. An alternating electric field  $E$  with the RMS value from 0.2 to 0.6 kV/mm is applied parallel to the line of centers of the droplets:

$$E = \frac{\phi}{\frac{\epsilon_{so}}{\epsilon_1} (h_1 + h_2) + h_0} \quad (4.1)$$

where  $\phi$  is a applied potential and  $h_1$  is a distance between the bottom of the cell to the bottom of the acrylic plate attached to the top electrode. The following applied frequencies  $f$  are used: 60 Hz, 10.3 kHz, 16.8 kHz 41.7 kHz. In all studied cases the charge relaxation frequencies of water  $f_w = \sigma_w / (\epsilon_0 \epsilon_w)$  and silicone oil  $f_{so} = \sigma_{so} / (\epsilon_0 \epsilon_{so})$  satisfy the following relationship  $f_w > f \gg f_{so}$ , representing a classic case of a leaky dielectric droplet pair suspended in a pure dielectric fluid.

### 4.3 Coalescence Sequence

Figure 4.2 shows a representative dynamics of a droplet pair. Initially freely suspended droplets polarize in the applied electric field, slightly elongate, and start to migrate towards one another. Polarization charges induced in the droplets affect the field uniformity enhancing electric field at top and bottom surfaces of the droplets and especially in the region between the droplets. The droplets assume characteristic egg-like shape. At 11.7 s, the local electric field between droplets reaches a critical value and the liquid bridge forms between droplets. The bridge formation allows charge and fluid transfer between the droplets. The

droplets assume the same potential. Positive and negative charges are shifted to the opposite ends of the continuous fluid structure. These charges alternate with the applied frequency using the conducting bridge interconnecting the droplets. The Maxwell stresses act on the opposite ends of the interconnected pair and the droplets start to move away from each other (13.2 s). Concurrently, the difference of the droplet diameters creates a pressure difference that drives the fluid flow through the bridge. A visual increase of one droplet and a decrease of another is observed between 11.7 s and 13.4 s. The bridge stretches and reduces in diameter but remains stable until  $\sim 13.4$  s. The bridge breaks up thereafter, and two partially coalesced droplets become electrically isolated forming two attracting dipoles. The attraction-repulsion sequence repeats itself with the oscillatory coalescence frequency  $f_c$  until the complete coalescence of the droplets.

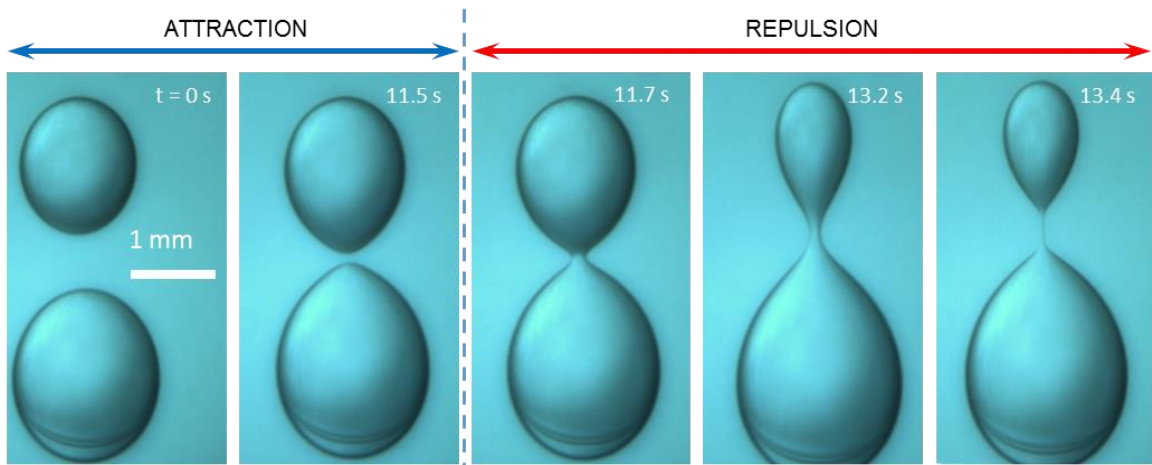


**Figure 4.2** Attraction and repulsion stages of the first oscillatory coalescence cycle for a pair of water droplets suspended in silicone oil ( $E = 0.38$  kV/mm,  $Ca_E = 0.09$ ,  $\sigma_w = 1.1$   $\mu$ S/cm,  $\alpha = 0.5$ , and  $f/f_w = 0.0695$ ). The liquid bridge formed in the repulsion stage alters the droplet dynamics by allowing charge and fluid transfer between droplets.

#### 4.4 Oscillatory Coalescence

At some experimental conditions, more than a few hundred cycles are required to achieve complete coalescence. In Figure 4.3 (a), the droplet contact repeats about two hundred times and the volume of the top droplet decreases with each cycle  $n$  as the fluid is transferred from the top to the bottom droplet. The volume ratio of the droplets consequently decreases from  $\alpha = 0.5$  to  $\alpha \approx 10^{-5}$ . The amount of fluid transfer per cycle ( $\sim 12.5$  nL/cycle on the average) demonstrates a complex behavior: it first decreases (cycles from 0 to 120), then increases and peaks at  $n \approx 150$ , and finally exponentially decreases until the final cycle of the oscillatory coalescence (Fig. 4.3b). The droplet oscillation frequency  $f_c$  remains practically constant ( $\sim 0.26$  Hz) for nearly 170 cycles ( $0.06 < \alpha < 0.5$ ) and steeply increases during the final cycles of the process (Fig. 4.3c).

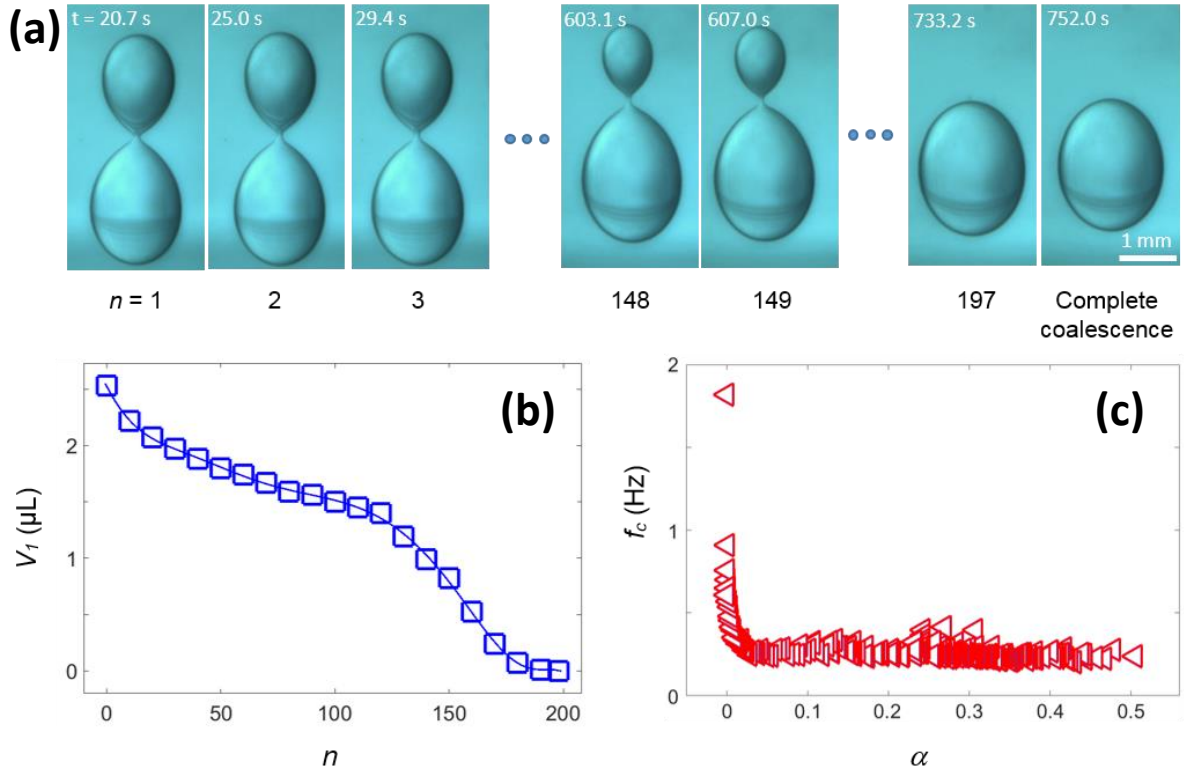


**Figure 4.3** (a) The oscillatory coalescence between a pair of droplets proceeds through 197 cycles ( $E = 0.42$  kV/mm,  $Ca_E = 0.11$ ,  $\sigma_w = 1.1$   $\mu\text{S/cm}$ , and  $f/f_w = 0.0695$ ). The liquid transfer reduces the droplet volume ratio from  $\alpha = 0.5$  to  $\alpha \approx 10^{-5}$ . The small satellite droplet completely coalesces during the last cycle. (b) The volume of the top droplet monotonically decreases with each cycle. (c) The oscillatory coalescence frequency remains practically constant for nearly 170 cycles.

#### 4.5 Fluid Transfer between Droplets

The fluid transfer is controlled by the pressure difference across the bridge and the bridge geometry. The effect of gravity is negligible in comparison to the surface tension: the characteristic Bond number of the system  $Bo = \Delta\rho g R^2 / \gamma$ , evaluated using the density difference of the two fluids  $\Delta\rho$  and the gravitational acceleration  $g$ , is less than  $10^{-2}$ . The excess pressure in the droplets is created by the surface tension and the Maxwell stresses. For

an isolated droplet, the Laplace pressure is inversely proportional to the droplet diameter and the Maxwell stresses are size independent. In an unequal pair, the smaller droplet has higher internal pressure. This forces the fluid transfer through the liquid bridge in the direction from the small to the large droplet. The Laplace pressure difference increases with the number of cycles. It is also expected that field non-uniformity and Maxwell stresses affect the fluid transfer in extremely unequal pairs ( $\alpha \ll 1$  and  $\alpha \gg 1$ ). The experiments with unequal pairs at  $\alpha = 0.5$  and  $\alpha = 1.5$  show the fluid transfer from smaller to larger drops (Fig. 4.4). Oscillatory coalescence of the pair at  $\alpha = 0.5$  proceeds through decrease of the top droplet in each consecutive cycle. Conversely, the coalescence of the pair at  $\alpha = 1.5$  shows monotonic increase of the top droplet. The system is metastable at the symmetry point ( $\alpha = 1$ ). Two equal droplets in a uniform electric field have the same internal pressure and perform oscillatory motion without noticeable fluid transfer until small initial difference in droplet size, field non-uniformity, or other body forces shift the system from the metastable point. This non-coalescence phenomena is observed at  $\alpha = 1$  with experimental conditions corresponding to Figure 4.4.

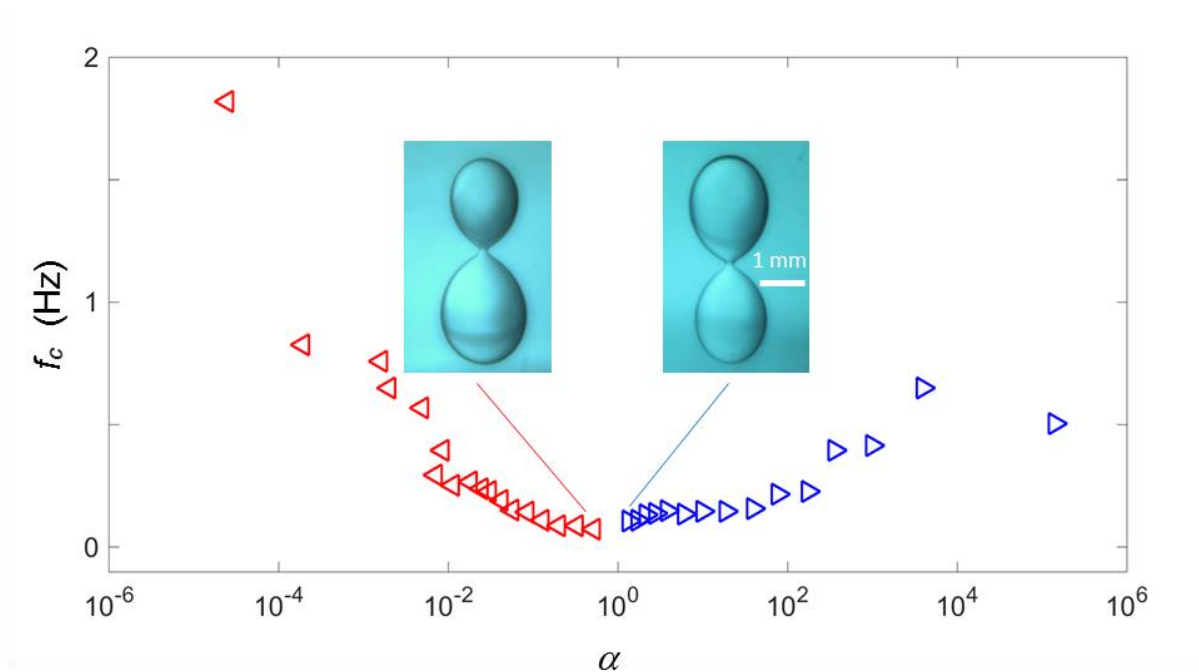


**Figure 4.4** Fluid transfer between droplets is controlled by the pressure difference induced by surface tension and electric stresses. Laplace's droplet pressures define a direction of fluid transfer in a uniform electric field at  $\alpha \sim 1$ . The oscillatory coalescence series initiated at  $\alpha = 0.5$  and  $\alpha = 1.5$  result in sequential increase of the larger drops ( $E = 0.40$  kV/mm,  $Ca_E = 0.10$ ,  $\sigma_w = 9.5$   $\mu$ S/cm, and  $f/f_w = 0.0695$ ). The system is metastable at the symmetry point ( $\alpha = 1$ ).

The bridge geometry in a single cycle is changing from a short and wide neck to a long thin thread interconnecting the droplets at the late repulsion stage (Fig. 4.2). This affects the fluid transfer rate. Fluid velocities in the bridge can be evaluated by measuring volumes of the droplets and bridge cross sectional areas. The fluid velocity at the moment of bridge formations reaches  $\sim 0.17$  m/s (Fig 4.2,  $t = 11.7$  s). This agrees well with the velocity evaluation based on the Bernoulli equation  $v \sim \sqrt{2\Delta P/\rho_w}$ , where  $\Delta P$  is the difference of Laplace's pressures in the droplets, and  $\rho_w$  is the water density. This also matches the characteristic velocities of the fluid reported for partial coalescence of the droplets in DC

field [7]. The fluid velocity drops as the bridge thins out and elongates. For long thin bridges, the characteristic velocity values  $\sim 1$  mm/s (Fig 4.2,  $t = 13.4$  s) are in a good agreement with the estimates based on Poiseuille flow.

## 4.6 Limits of Existence of the Oscillatory Coalescence

### 4.6.1 Effect of the Electric Field

The oscillating coalescence has a limit of existence in terms of the electric field strength. The effect of the electric field on the droplet coalescence frequency is shown in Figure 4.5 (a). The oscillation frequency remains practically constant  $\sim 0.2$  Hz for electric field strengths from 0.38 kV/mm to 0.47 kV/mm with  $\sigma_w = 1.1$   $\mu\text{S}/\text{cm}$  and initial  $\alpha = 0.5$ . The complete coalescence of the droplets on the first contact is observed at the electric fields lower than 0.38 kV/mm ( $Ca_E < 0.09$ ), as shown in Figure 4.6. The bridge thins out and becomes unstable at electric fields greater than 0.47 kV/mm. The droplet oscillation and periodic formation of the thin bridge is observed at  $Ca_E = 0.156$  (Fig. 4.7). However, the bridge is unstable and frequently breaks up generating a fine water-in-oil emulsion [52] in the area between two droplets (Fig. 4.7). The fluid transfer rate drops by two orders of magnitude with the electric field increase from 0.38 kV/mm to 0.47 kV/mm (Fig. 4.5b). Only 24 cycles are required for complete coalescence at 0.40 kV/mm, 200 cycles are needed at 0.42 kV/mm, and less than 10% of the fluid is transferred at 0.47 kV/mm after 150 cycles. In contrast, more than 50% of the fluid is transferred during the first cycle at  $E = 0.38$  kV/mm, where the two droplets almost completely coalesce, but, then, break up again and continue to oscillate

for another 14 cycles reaching  $\beta \approx 40$  before the last cycle. The average flowrate is  $\sim 2$  nL/cycle at  $E = 0.47$  kV/mm compared with  $\sim 100$  nL/cycle at  $E = 0.38$  kV/mm: the higher is the electric field strength, the less volume is transferred per cycle. Thinner and longer bridges form at high electric fields generating significant flow resistance.

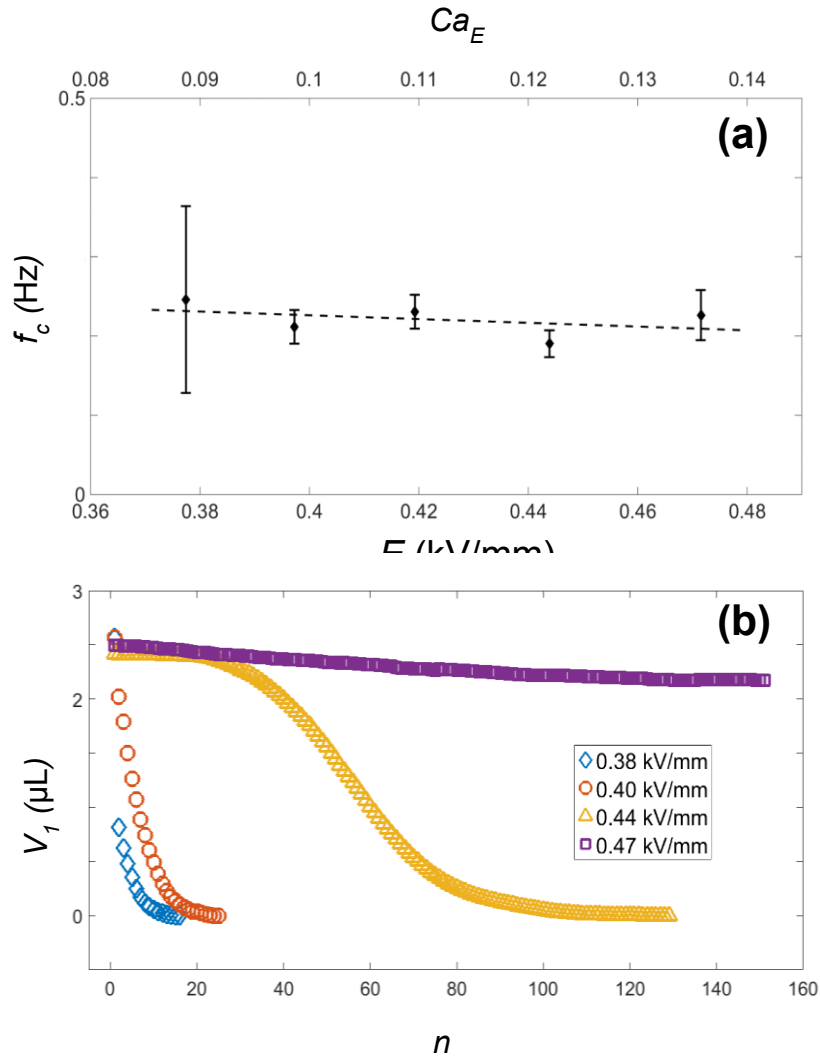


**Figure 4.5** Effect of the electric field strength on the oscillatory coalescence frequency (a) and fluid transfer (b) for  $\sigma_w = 1.1 \mu\text{S}/\text{cm}$  and initial  $\alpha = 0.5$ . The oscillation frequency is averaged over the first 10 cycles.

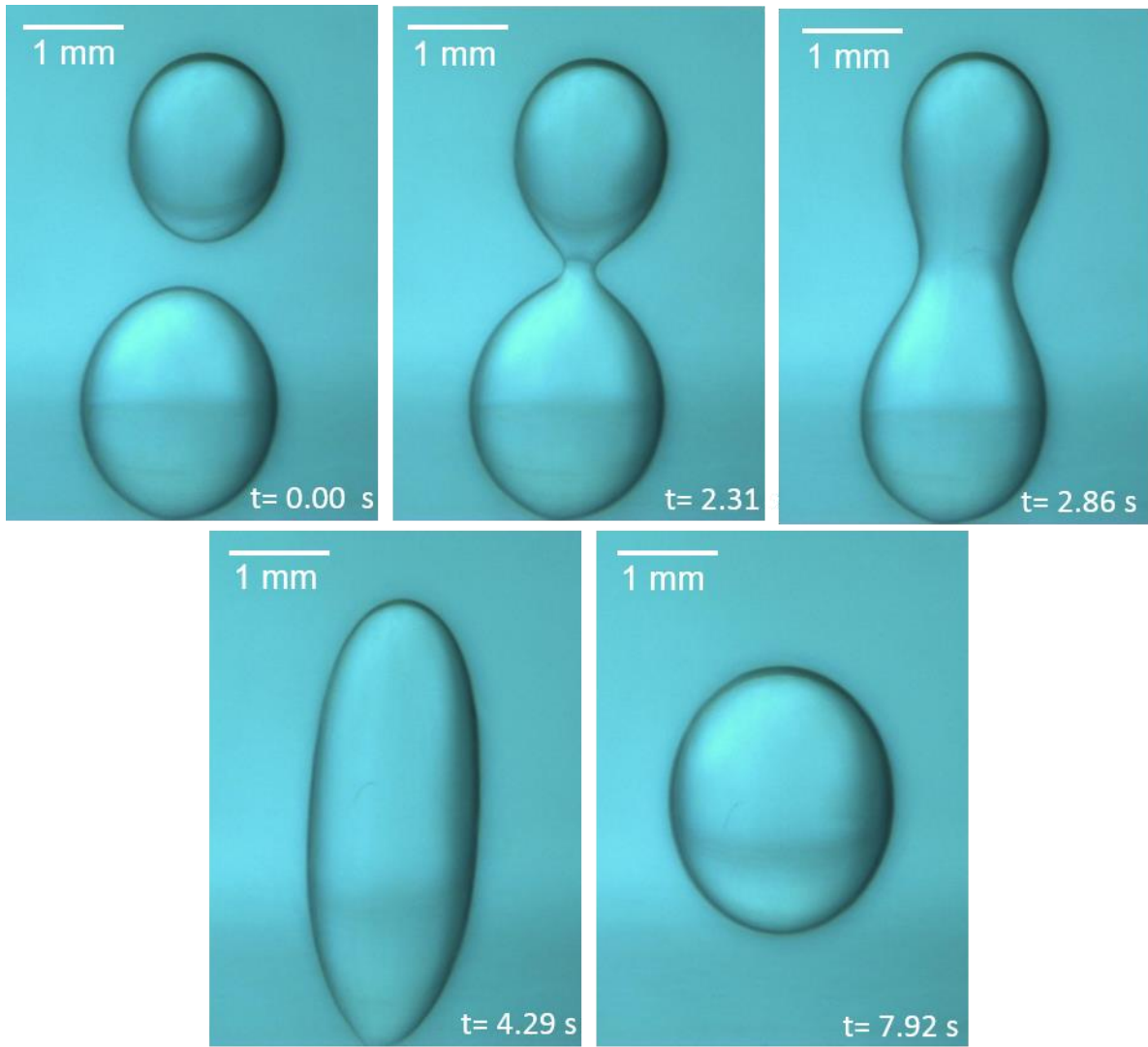


**Figure 4.6** Sequential images of complete coalescence of the droplets on the first contact at the electric fields lower than 0.38 kV/mm ( $Ca_E < 0.09$ ) for  $\sigma_w = 1.1 \mu\text{S}/\text{cm}$ , initial  $\alpha = 0.5$ , and  $f/f_w = 0.0695$ .

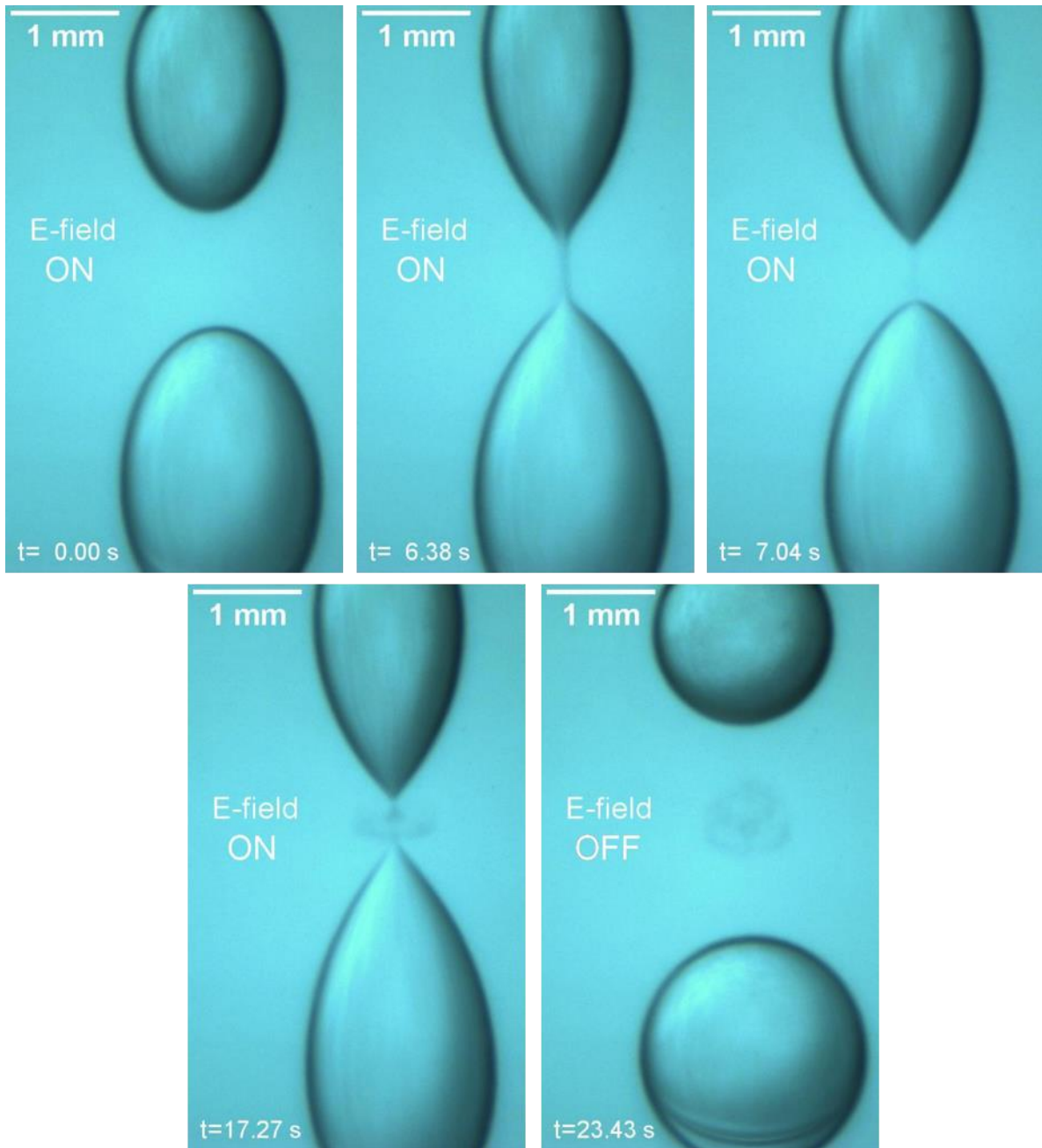


**Figure 4.7** The bridge thins out and becomes unstable at electric fields greater than 0.47 kV/mm. The droplet oscillation and periodic formation of the thin bridge is observed at  $Ca_E = 0.156$  for  $\sigma_w = 1.1 \mu\text{S/cm}$ , initial  $\alpha = 0.5$ , and  $f/f_w = 0.0695$ . The bridge is unstable and frequently breaks up generating a fine water-in-oil emulsion in the area between two droplets.

The effect of an electrical conductivity on the oscillating coalescence is shown in Figure 4.8 for  $E = 0.40$  kV/mm and  $f = 10.3$  kHz. The frequency of oscillatory coalescence is  $\sim 0.2$  Hz at  $\sigma_w = 1.1$   $\mu\text{S/cm}$ . It attains a minimum of  $\sim 0.04$  Hz at  $\sigma_w = 6.2$   $\mu\text{S/cm}$  and further increases with the conductivity increase (Fig. 4.8a). A mode of droplet interaction is changing from oscillatory coalescence to electro spray when conductivity increases above 40  $\mu\text{S/cm}$ . Figure 4.9 shows the non-coalescence mode observed at  $E = 0.40$  kV/mm and  $f = 10.3$  kHz for  $\sigma_w = 234$   $\mu\text{S/cm}$ . In the electro spray mode the droplets first attract towards one another (Fig. 4.9,  $t = 0$  s), deforming and developing Taylor's cones on the adjacent surfaces (Fig. 4.9,  $t = 7.37$  s). The electro spray starts at a certain distance and results in a partial charge transfer between droplets (Fig. 4.9,  $t = 7.37$  s to 30.25 s). It should be noted that at higher conductivity with thin bridge, bubbles shown in Figure 4.9 at  $t = 8.58$  s are created due to the Joule's heating proportional to the conductivity and the length of liquid bridge. The small charges of opposite polarity acquired during each ac cycle create repulsion force that compensates the dipole attraction between the droplets. The droplets stabilize without contacting each other continuously emitting electro sprays towards each other. The electro spray interaction mode is observed at higher conductivities where a droplet pair instead of coalescence is effectively emulsified into a cloud of fine microdroplets (Fig. 4.9). Variation of electrical conductivity from 1.1  $\mu\text{S/cm}$  to 9.5  $\mu\text{S/cm}$  has a weak influence on the fluid transfer rate (Fig. 4.8b). Maximum volume per cycle is transferred at  $\sigma_w = 6.2$   $\mu\text{S/cm}$  corresponding to the lowest oscillation frequency. At  $\sigma_w = 1.1$   $\mu\text{S/cm}$  and  $\sigma_w = 9.5$   $\mu\text{S/cm}$  oscillatory coalescence ends at 17 and 21 cycles, respectively.

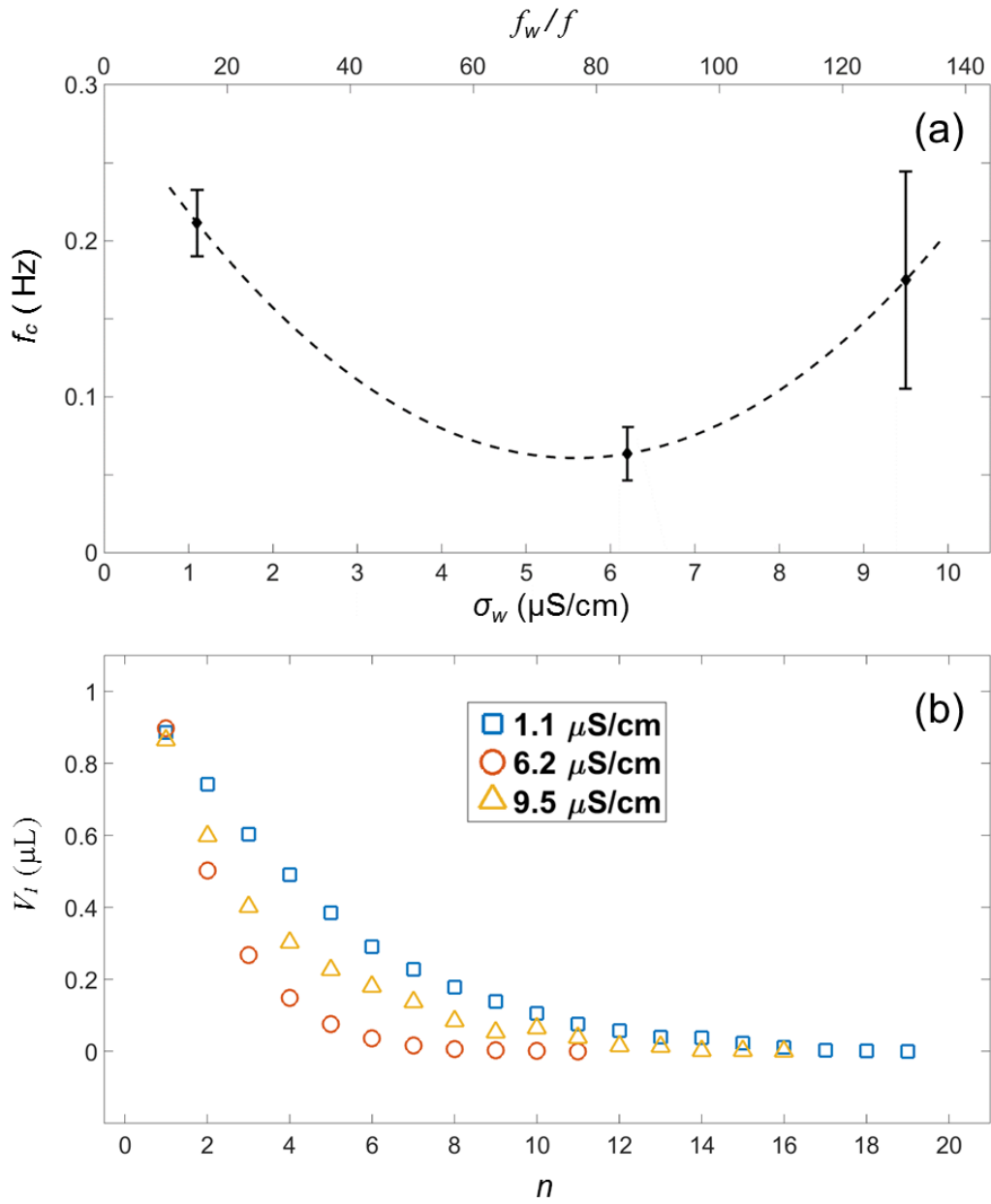


**Figure 4.8** Effect of the electrical conductivity of water droplets on the oscillatory coalescence frequency (a) and fluid transfer (b) at  $E = 0.40$  kV/mm and initial  $\alpha = 0.5$  ( $f_c$  is averaged over the first 10 cycles).

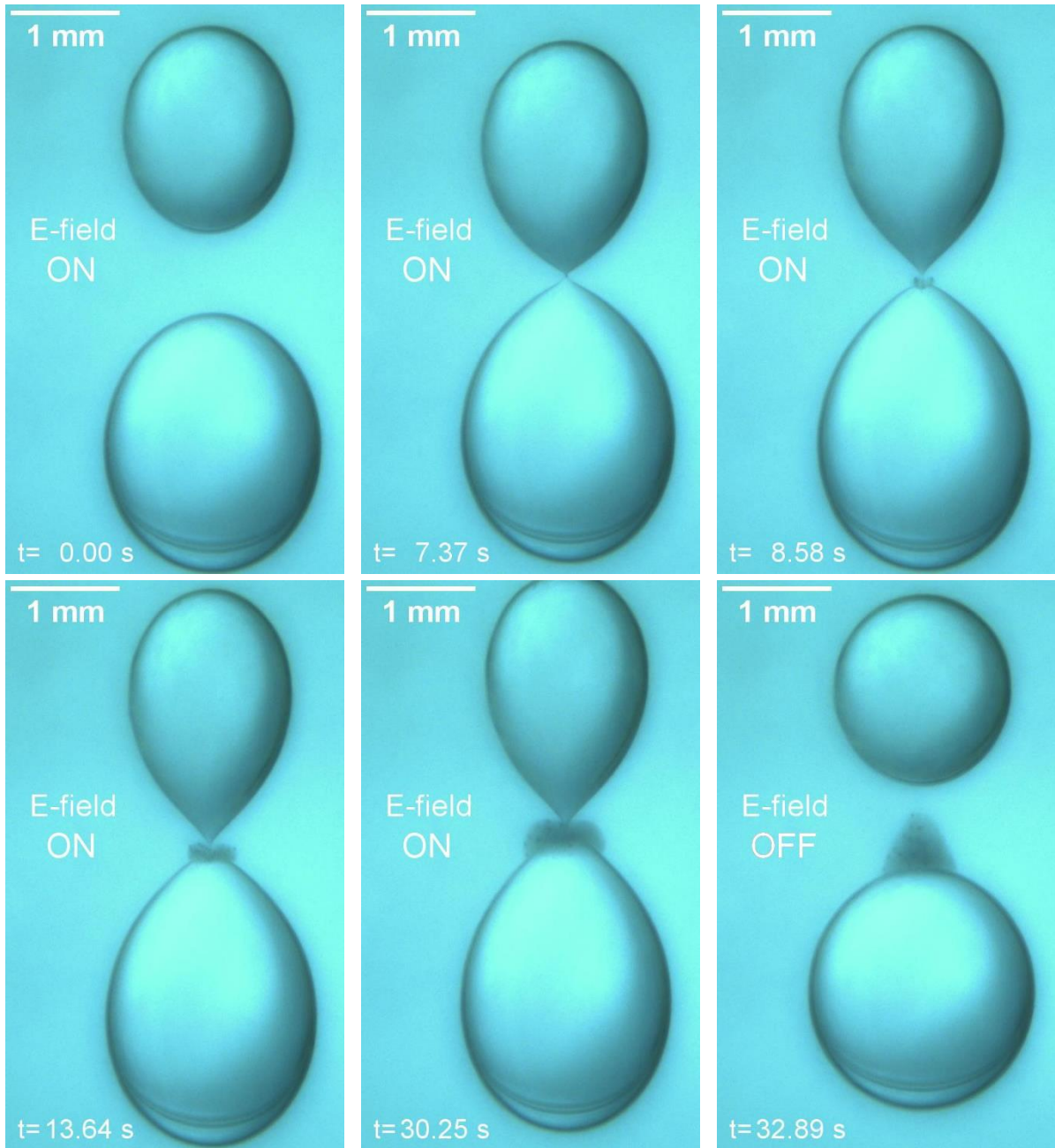


**Figure 4.9** Non-coalescence mode is observed at  $Ca_E = 0.10$  for  $\sigma_w = 234 \mu\text{S}/\text{cm}$ , initial  $\alpha = 0.5$ , and  $f/f_w = 3.3 \cdot 10^{-4}$ . In this mode the droplets first attract towards one another, deform and develop electrified menisci on the adjacent surfaces. The electrically-induced emission of mass starts at a certain distance and results in a partial charge transfer between the droplets.

#### 4.6.2 Effect of Non-dimensional Frequency

The region of existence of the oscillatory coalescence is shown in Figure 4.10 in terms of the electric capillary number and the non-dimensional frequency  $ff_w$  defined as a ratio of the applied frequency to the charge relaxation frequency of water. As expected, the complete coalescence on the first contact (Fig. 4.6) is observed at low electric fields ( $Ca_E < 0.09$ ) where the surface tension is dominant. The complete coalescence is also observed at  $ff_w > 0.1$ . The region of  $f \approx f_w$  corresponds to the transition from leaky dielectric to pure dielectric behavior of water. A transfer of free charges responsible for the repulsion forces in a coalescing pair is negligible in a pure dielectric fluid. As a result, only attractive forces exist between the droplets in this region and complete coalescence occurs on the first contact. Oscillatory coalescence is observed in the range of capillary numbers  $0.09 < Ca_E < 0.15$  and non-dimensional frequencies  $3 \cdot 10^{-3} < ff_w < 10^{-1}$ . A mode of droplet interaction is changing from oscillatory coalescence to non-coalescence when  $ff_w$  drops below  $3 \cdot 10^{-3}$ . In this mode the droplets first attract towards one another, deform and develop electrified menisci on the adjacent surfaces. The electrically-induced emission of mass starts at a certain distance and results in a partial charge transfer between the droplets. The droplets stabilize without contacting each other interacting via electrified jets. At  $ff_w < 3 \cdot 10^{-3}$ , a droplet pair is effectively emulsified into a cloud of fine microdroplets (Fig. 4.9). A non-coalescence pattern observed at  $Ca_E > 0.15$  involves droplets oscillation and periodic formation of unstable thin bridges (Fig. 4.7). A fine water-in-oil emulsion is created in the region between two droplets by frequent capillary breakups of the unstable bridges.

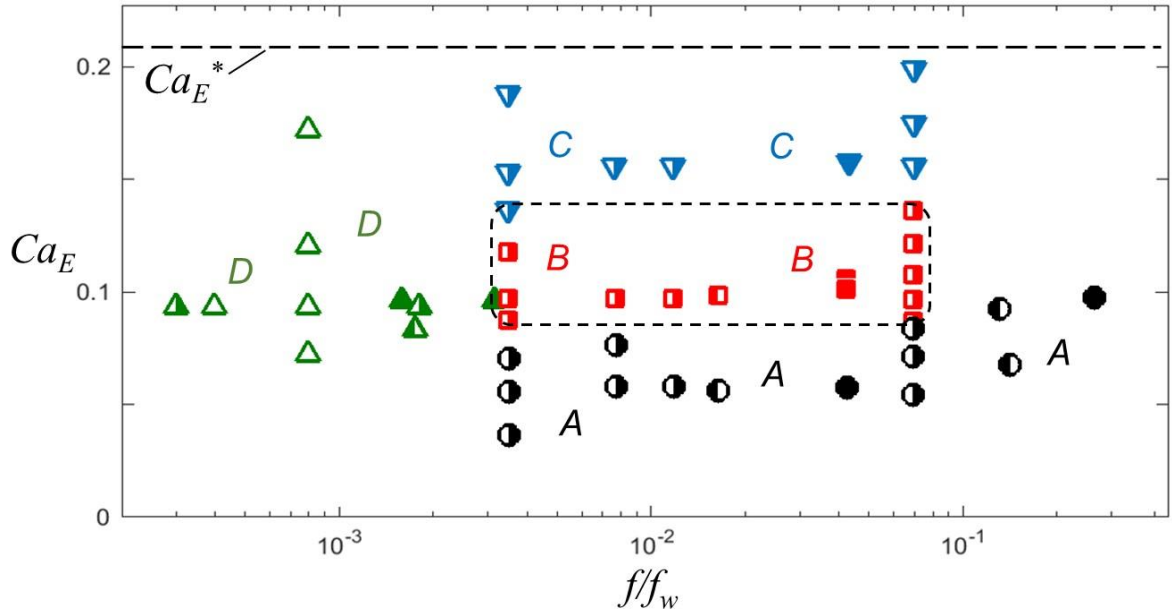


**Figure 4.10** Diagram illustrating the various coalescence regimes: (A) complete coalescence on the first contact, (B) oscillatory coalescence, (C) non-coalescence with the oscillatory motion of the droplet pair, unstable bridge formation and emulsification, (D) non-coalescence with droplets attraction, deformation and stabilization at a certain distance with electrified jet emissions; color also indicates the different coalescence regimes. The results are obtained with the water conductivities in the range from (0.5  $\mu\text{S}/\text{cm}$  to 235  $\mu\text{S}/\text{cm}$ ) and four applied frequencies: 60 Hz (hollow symbols), 10.3 kHz (symbols solid on the right), 16.8 kHz (symbols solid on the left), 41.7 kHz (solid symbols).

#### 4.7 Energy Based Model of the Oscillatory Coalescence

It is interesting to consider oscillatory coalescence of two equal droplets using an energy-based model. The kinetic energy of the droplets is negligible in the highly viscous oil and only surface and electric energies can be considered in the quasistatic approximation. Let the radii of the identical droplets be  $r$  and the center-to-center spacing be  $h$ . To avoid computational complexity the droplets are considered spherical for  $h \geq 2r$ , and the intersecting spheres model with total volume constraint is employed at  $0 \leq h < 2r$  [92]. The

total energy of the system  $U$  is represented as the sum of the surface energy  $U_s$  and the electric energy  $U_e$ :

$$U = U_s + U_e \quad (4.2)$$

We have further normalized the surface energy of the system by the surface energy of two isolated droplets  $8\pi\gamma r^2$ :

$$u_s = U_s / 8\pi\gamma r^2 \quad (4.3)$$

The electrical energy can be normalized by the energy of two conducting spheres with radius  $r$  placed in a dielectric medium with the electric field strength  $E$ :

$$u_e = U_e / 8\pi\epsilon_0 r^3 E^2 \quad (4.4)$$

Finally, the total energy of the system can be normalized by the surface energy of two isolated droplets  $8\pi\gamma r^2$  as:

$$u = U / 8\pi\gamma r^2 = u_s + u_e (8\pi\epsilon_0 r^3 E^2 / 8\pi\gamma r^2) \quad (4.5)$$

$$u = u_s + u_e \cdot \frac{Ca_E}{\sqrt[3]{2}} \quad (4.6)$$

#### 4.7.1 Surface energy of the intersecting spheres model

The geometry of two intersecting spheres is shown in Figure 4.11. The spheres have an equal radius that increases as the spheres approach each other because of the total volume constraint. According to this constraint the total volume of the fluid  $Q = 8\pi r^3/3$  remains constant. The radius, volume, and the surface area of the intersecting spheres could be found using the following method.

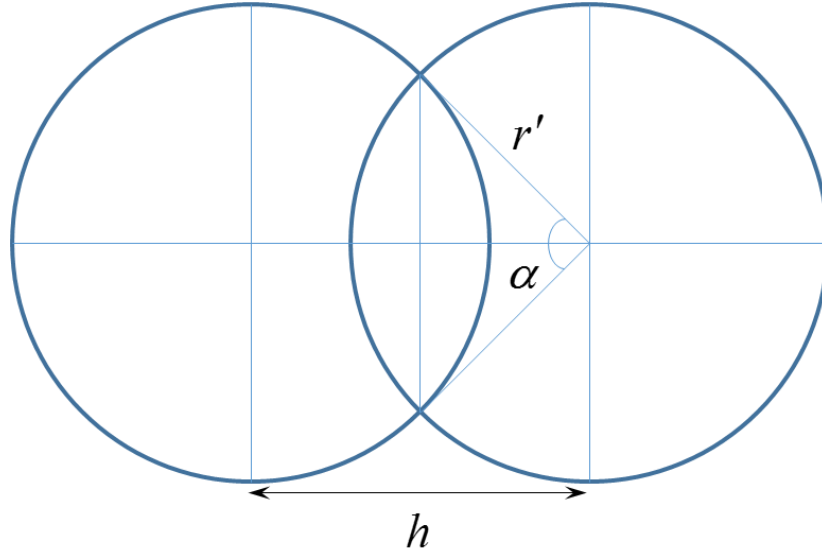


**Figure. 4.11** Geometry of the intersecting spheres model.

Consider angle  $\alpha$  corresponding to the cross section of the cone with the apex in the center of the sphere and the base formed by the section of the intersecting spheres with the symmetry plane. The solid angle  $\omega$  of a cone with the apex angle  $\alpha$  is given as:

$$\omega = 2\pi \left( 1 - \cos \frac{\alpha}{2} \right) \quad (4.7)$$

When  $\alpha = \pi$ , the solid angle is  $2\pi$ , which corresponds to the case of fully coalesced droplets. When  $\alpha = 0$ , the solid angle is 0, which corresponds to the case of two separate droplets. The radius  $r'$  of the intersecting spheres could be calculated using the total volume constraint. The volume of the intersecting spheres can found as:

$$Q = 2 \left( \frac{4}{3} \pi r'^3 \frac{4\pi - \omega}{4\pi} + \frac{1}{3} \pi r'^3 \cos \left( \frac{\alpha}{2} \right) \sin^2 \left( \frac{\alpha}{2} \right) \right) \quad (4.8)$$

From here the radius of the intersecting spheres can be expressed as:

$$\frac{r'}{r} = \left( \frac{4}{2 + 2 \cos\left(\frac{\alpha}{2}\right) + \cos\left(\frac{\alpha}{2}\right) \sin^2\left(\frac{\alpha}{2}\right)} \right)^{\frac{1}{3}} \quad (4.9)$$

The surface area of the intersecting sphere could be calculated as:

$$S = 2(4\pi - \omega)r'^2 \quad (4.10)$$

Finally, the surface area could be expressed as a function of  $\alpha$ :

$$S = 4\pi \left(1 + \cos\frac{\alpha}{2}\right) r'(\alpha)^2 \quad (4.11)$$

Finally the droplet spacing  $h$  can be related with the angle  $\alpha$  as:

$$\frac{h}{r} = \frac{2r'}{r} \cos\left(\frac{\alpha}{2}\right) \quad (4.12)$$

When  $\alpha = \pi$ , the droplet spacing zero, which corresponds to the case of fully coalesced droplets. When  $\alpha = 0$ , the droplet spacing solid angle is  $2r$ , which corresponds to the case of two separate droplets).

The radius of the intersecting droplets, the droplet spacing, and the surface energy can be calculated using Eqs. (4.9), (4.11) and (4.12). These parameters are listed in Table 4.1 in a non-dimensional form.

**Table 4.1** Non-dimensional radius, spacing, and surface energy for the intersecting spheres model.

Angle $\alpha$	Radius $r'/r$	Spacing $h/r$	Surface Energy $u_s$
3.141593	1.25992	0	0.79370
2.094395	1.05827	1.05827	0.83995
1.570796	1.02014	1.44269	0.88828
1.256637	1.00869	1.63209	0.92030
1.047198	1.00432	1.73954	0.94109
0.897598	1.00238	1.80623	0.95501
0.785398	1.00141	1.85038	0.96465
0.698132	1.00089	1.88106	0.97157
0.628319	1.00059	1.90323	0.97668
0.314159	1.00004	1.97545	0.99392
0.125664	1.00000	1.99606	0.99901
0	1.00000	2	1.00000

The non-dimensional surface energy of the droplets is plotted as a function of the droplet spacing in Figure 4.12. The normalized surface energy is equal to 1 for  $h > 2r$ . The energy reduces with the spacing in the interval  $h < 2r$  approaching the limit of fully coalesced droplets of  $u_s = 1/2^{1/3}$ .

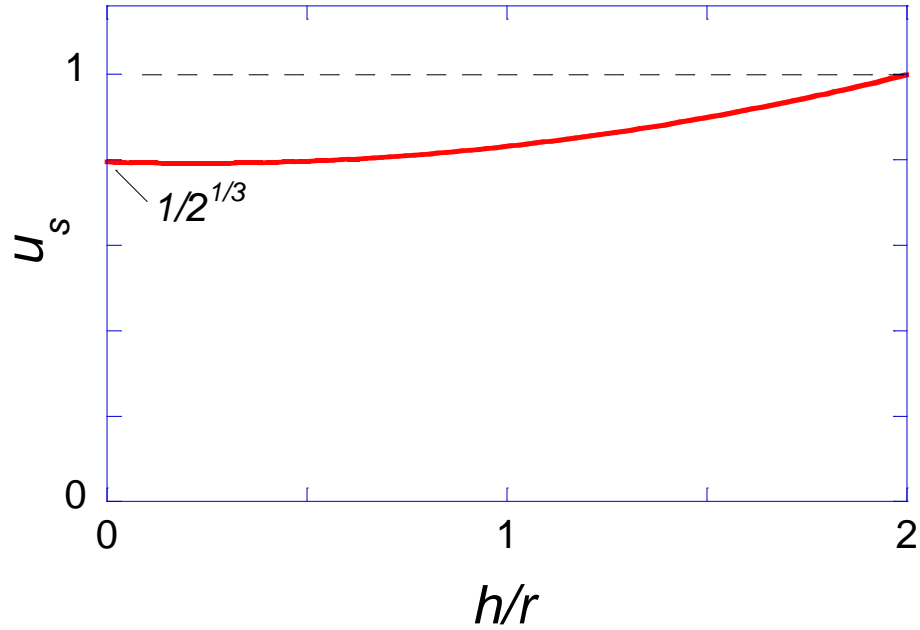


**Figure 4.12** The normalized surface energy as a function of the droplet spacing for the intersecting spheres model.

#### 4.7.2 Electrical energy of the intersecting spheres model

The dipole moment of two intersecting spheres as a function of the droplet spacing was adopted from Ref. [92,93]. The electric energy of the dipole was calculated as  $-pE$  and normalized by  $8\pi\epsilon_0 r^3 E^2$ . The non-dimensional angle, droplet spacing, dipole moment and electrical energy are listed in Table 4.2.

The non-dimensional electrical energy of the droplets is plotted as a function of the droplet spacing in Figure 4.13. The normalized surface energy is equal to -1 for  $h = 0$ . The energy reduces with the spacing in the interval  $h < 2r$  approaching  $u_e = -2\zeta(3)$  at  $h = 2r$ , where  $\zeta$  is the Riemann-zeta function.

**Table 4.2** Non-dimensional spacing, dipole moment, and electrical energy for the intersecting spheres model.

Angle ( $\alpha$ )	Spacing ( $h/r$ )	Dipole moment ( $p/\pi\epsilon_1 r^3 E$ )	Electrical energy ( $u_e$ )
3.141593	0	8.00000	-1
2.094395	1.05827	11.85190	-1.4814
1.570796	1.44269	14.24126	-1.7801
1.256637	1.63209	15.70716	-1.9633
1.047198	1.73954	16.63841	-2.0798
0.897598	1.80623	17.25547	-2.1569
0.785398	1.85038	17.68123	-2.2101
0.698132	1.88106	17.98567	-2.2482
0.628319	1.90323	18.21018	-2.2762
0.314159	1.97545	18.96649	-2.3708
0.125664	1.99606	19.18966	-2.3987
0	2	19.23280	-2.4041

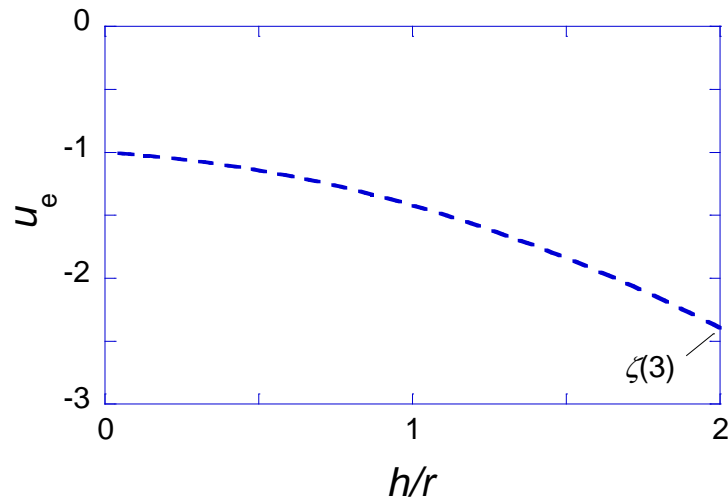


**Figure 4.13** The normalized electrical energy as a function of the droplet spacing for the intersecting spheres model.

### 4.7.3 Total energy of the intersecting spheres model

The total normalized energy of the droplets was evaluated using Eq. (4.6). The model results were plotted for a few characteristic  $Ca_E$  numbers in Figure 4.14. At  $Ca_E = 0.06$ , the total energy of the droplet has a well-defined minimum at  $h = 0$ . The droplet is stable. At  $Ca_E = 0.15$ , the energy minimum is displaced to  $h/r \approx 0.7$ . The droplet is expected to elongate, but remains stable. At the critical capillary number  $Ca_E^* = 0.21$  the energy minimum is displaced to  $h/r = 2$ . The energy distribution is flat in this area suggesting instability of the droplet and its break up. Finally, at  $Ca_E = 0.3$ , the energy monotonically drops with  $h/r$  and the droplet is unstable. In summary, the energy model based on rather simplifying assumptions predict the same critical capillary number as the theory of Taylor [2].

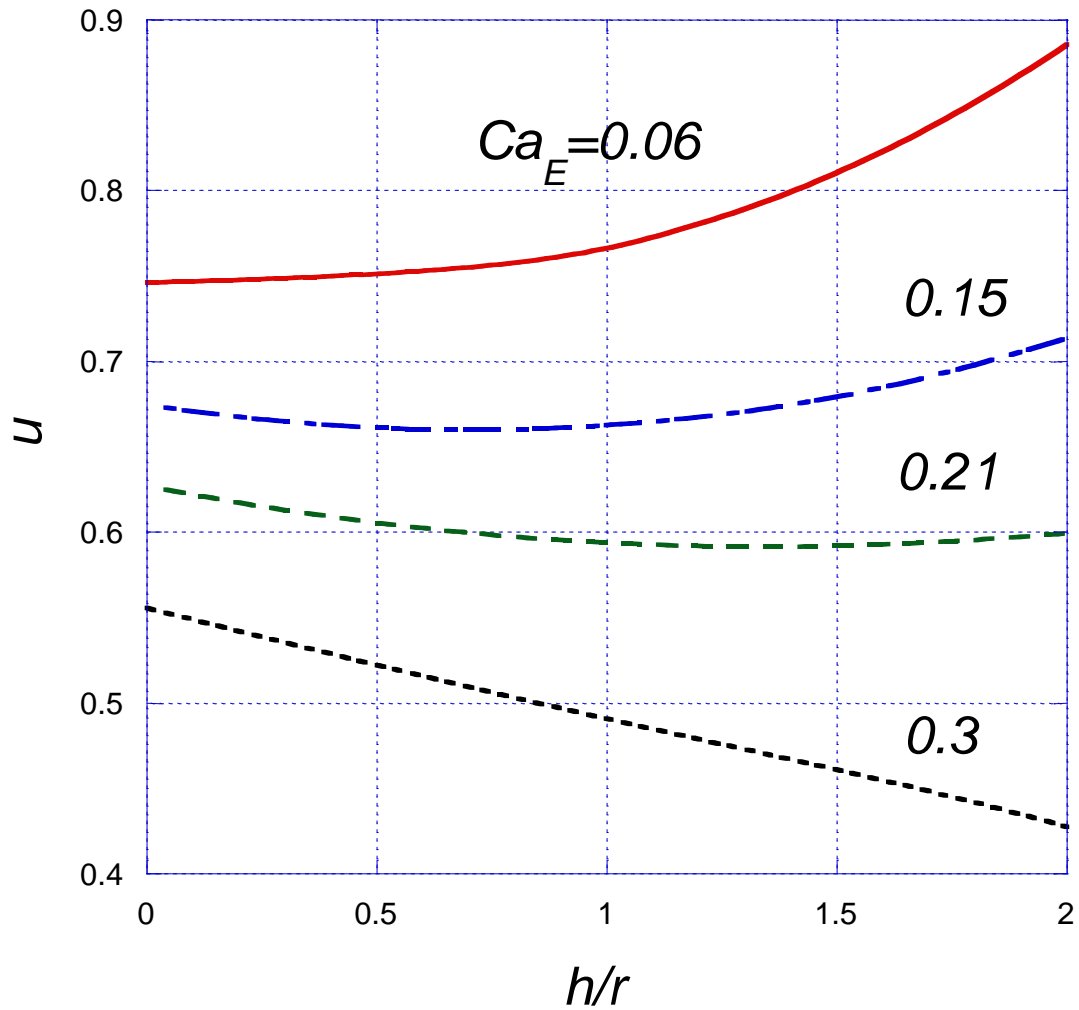


**Figure 4.14** The normalized energy plotted as a function of the droplet spacing of the intersecting spheres model for a few  $Ca_E$  numbers defined based on the radius of a single droplet with the same total volume.

#### 4.7.4 Critical Electric Capillary Number

Figure 4.15 (a) shows the normalized surface and electric energy of the droplets for the non-dimensional droplet spacing  $0 < h/r < 4$ . For non-contacting droplets the normalized surface energy  $u_s$  is equal to 1. The electric energy of the system is evaluated as  $-pE$ , where  $p$  is the

dipole moment of the droplet pair available as a function of spacing for isolated, equipotential, and intersecting spheres [92,94,95]. The normalized electric energy of the system, defined as  $u_e = U_e/8\pi\epsilon_0r^3E^2$ , is equal to -1 for two isolated ( $h \rightarrow \infty$ ) and for two fully coalesced ( $h = 0$ ) droplets (Fig. 4.15a). Electrically isolated droplets attract each other and minimize electric energy up to the point of contact  $h = 2r$ . After contact, the droplets are considered equipotential if  $h < 2r$  or if  $h > 2r$  and the liquid bridge connection exists. Electric energy of equipotential droplets monotonically decreases with an increase in the droplet spacing.

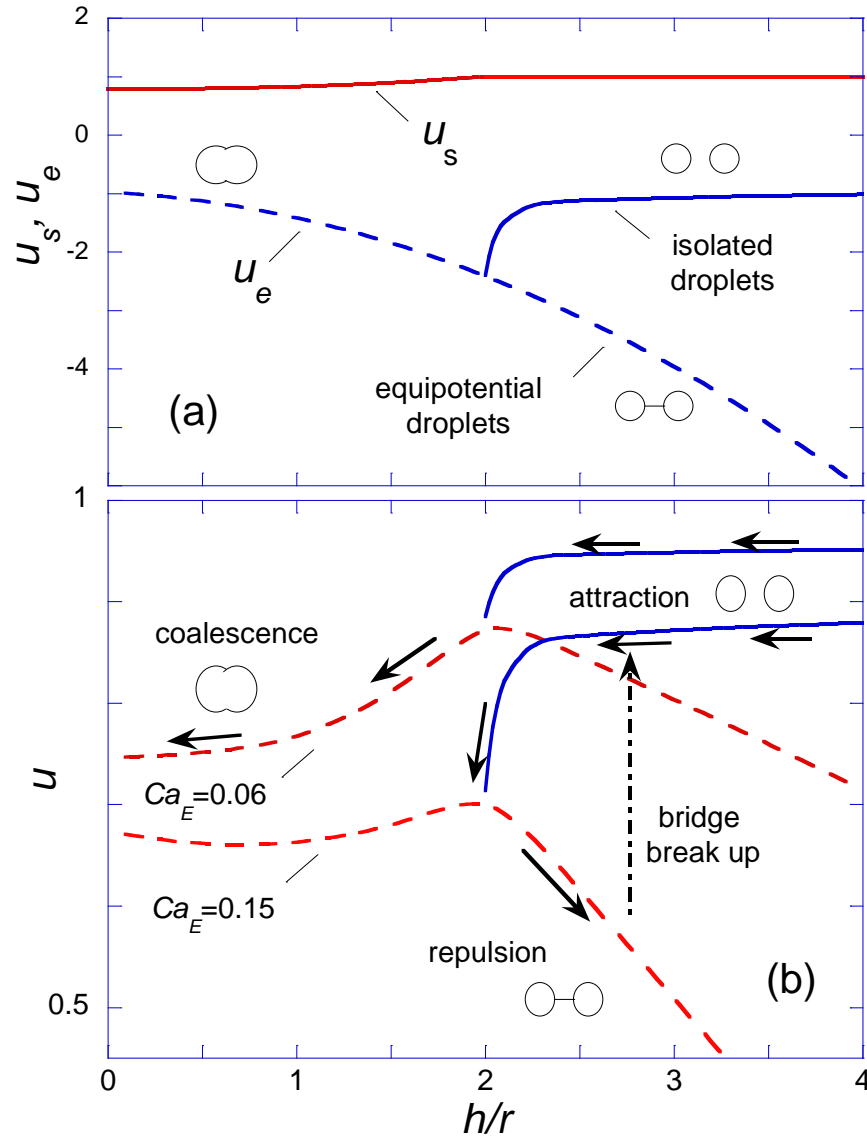


**Figure 4.15** (a) Normalized surface and electric energies of two equal droplets as functions of relative distance between droplets. (b) Total energy of the pair for electrically isolated droplets (solid line) and for equipotential droplets (dashed line) defines the droplet coalescence path. At  $Ca_E = 0.06$  the droplets coalesce after the first contact. At  $Ca_E = 0.15$  the droplets coalesce through oscillatory motion.

Two sets of curves for  $Ca_E = 0.06$  and  $Ca_E = 0.15$  show characteristic droplet evolution in the energy space (Fig. 4.15b). At  $Ca_E = 0.15$ , two isolated droplets first

minimize the total energy by moving towards each other and making a contact at  $h = 2r$ . The droplet potentials equalize after the fluid contact. Two scenarios are possible at this point: coalescence or recoil. The outcome is defined by a balance of the attraction and repulsion forces at the point of contact. The magnitudes of the attraction and repulsion forces can be evaluated from the absolute values of the left and right derivatives of  $du/dh$  at  $h = 2r$  taken along the equipotential curve. At  $Ca_E = 0.15$ , the repulsion force proportional to the slope on the right side of the contact point is stronger than the attraction force (the slope on the left side of the contact point). The droplets start to move apart, the liquid bridge forms, elongates and finally breaks up at a certain droplet spacing. The droplets become electrically isolated and transfer to the attraction curve and the cycle repeats. In contrast, at  $Ca_E = 0.06$ , two initially isolated droplets are attracted and fully coalesce after the first contact according to the energy diagram. The model predicts the existence of the critical  $Ca_E^{**}$  number that separates the regions of complete and oscillatory coalescence. Comparing the absolute values of the left and right derivatives at  $h = 2r$  it is possible to evaluate  $Ca_E^{**}$  as  $\sim 0.09$ , which is in a good agreement with our experimental results (Fig. 4.10). Thus the region of existence for oscillatory coalescence can be defined as  $Ca_E^{**} < Ca_E < Ca_E^*$ . The electric capillary number in this range is necessary but not sufficient condition of oscillatory coalescence. Other important conditions involve bridge stability in terms of electric field and charge relaxation frequency. The high viscosity of the continuous phase is also critically important. The kinetic energy of the droplets in low viscosity fluids could lead to the complete coalescence of the droplet pair on the first contact. The energy model assumes that the kinetic energy of the

droplets at the point of contact is negligible in comparison with the electrical energy of the droplets. This assumption can be expressed using the following inequality:

$$8\pi r^3 \rho v^2 / 6 \ll 8\pi \epsilon \epsilon_0 r^3 E^2, \quad (4.13)$$

where  $\rho$  is the droplet density, and  $v$  is the droplet velocity at the point of contact. Comparing the Stokes drag force  $6\pi\mu r v$  in the continuous phase with the viscosity  $\mu$  and dielectrophoretic attraction force  $\sim 4\pi\epsilon\epsilon_0 r^2 E^2$  yields:

$$v \approx \epsilon \epsilon_0 r E^2 / \mu \quad (4.14)$$

The substitution of the characteristic velocity value in Eq. (4.13) gives:

$$\rho r^2 \epsilon \epsilon_0 E^2 / 6 \mu^2 \ll 1 \quad (4.15)$$

Using the electric capillary number and the Ohnesorge number defined as  $Oh = \mu / \sqrt{\rho \gamma r}$  then yields:

$$Ca_E \ll Oh^2 \quad (4.16)$$

For characteristic value of  $Ca_E = 0.09$  the model assumption is valid for  $Oh \gg 0.3$ . This scale analysis agrees well with experimental range of the Ohnesorge numbers reported for the partial coalescence of droplets in DC fields [7]. The characteristic Ohnesorge number for the 10000 cSt silicone oil used in our experiments is  $\sim 50$ . This suggests that a reduction in the viscosity of the continuous phase of  $\sim 50$  times could be possible for oscillatory/partial coalescence in AC electric fields. However, in our experiments, droplet pairs coalesce on the first contact in the silicone oil with the kinematic viscosity of 1000 cSt ( $Oh \approx 5$ ). We partially attribute this inconsistency to the experimental difficulties associated with the initial

stabilization of the droplet pairs settling in the gravity field and plan to use alternative experimental arrangements to investigate low viscosity phases.

The viscosity of the continuous phase also affects the dynamics of droplets and liquid bridge thinning. The characteristic viscocapillary frequency  $f_\mu = \gamma / \mu r$  that describes the thinning of a viscously dominated thread with radius  $r$  is  $\sim 5$  Hz for the 10000 cSt silicone oil and  $r = 1$  mm. This is an order of magnitude higher than the observed oscillatory coalescence frequency. The latter is defined by the droplet attraction, the longest stage in the oscillatory coalescence cycle. The evaluation of  $f_c$  using the characteristic velocity at the point of contact (Eq. 4.14) yields  $f_c = v/r = f_\mu Ca_E / \sqrt{2}$ . For  $Ca_E = 0.1$ , the characteristic value of  $f_c \sim 0.4$  Hz agrees in the order of magnitude with the experimentally recorded values.

The critical electric capillary number obtained from the simplified energy model agrees well with the results obtained for the partial droplet coalescence in DC fields [22,91]. The model of coalescence of two droplets based on the critical angle of two contacting liquid cones suggested the existence of the critical capillary number  $Ca_E^{**} \approx 0.1$ . The droplets in DC field fully coalesced below this critical number and recoil above it. Previously, Brazier-Smith et al. [91], numerically predicted a partial fluid transfer and complex coalescence behavior of an electrified droplet pair at  $Ca_E^{**} > 0.1$ . A contact between droplets in DC electric field leads to one-time transfer of charges across the point of contact. If the electric field is sufficiently strong, the attraction is changed to the repulsion and droplets start to travel in the opposite directions. As a result, the oscillatory coalescence is not observed in DC electric fields. It should be noted, that a direct comparison and extrapolation of our

results to the DC case is inappropriate as another characteristic interval of the applied frequencies  $f_w \gg f_{so} > f$  exists between the region of frequencies studied in this work and DC.

According to the experimental results, once initiated at the droplet size ratio  $\beta \approx 1$  the oscillatory coalescence enhances the droplet disparity to extreme size and volume ratios. The complete coalescence is the final step of the sequence at  $\beta$  of  $\sim 20$  to  $50$ . At this point one of the droplets is a very small satellite droplet oscillating near the surface of the large droplet. The final coalescence is expected at this point: the surface energy of the satellite droplet is reduced  $\sim r^2$  and the electrical energy is reduced  $\sim r^3$ . The surface energy dominates during the final oscillation steps resulting in the complete coalescence. The above energy model qualitatively predicts this behavior, however, it fails to predict extreme volume and size ratios observed in the experiments.

#### 4.8 Stability of Liquid Bridge

The existence and stability of the liquid bridge between the droplets is crucial for oscillatory coalescence. High aspect ratio bridges in pure dielectric fluids are stabilized by polarization charges and resulting tangential stresses on the surface of the bridge [96]. In contrast, the classical leaky dielectric model applied to the bridge results in zero electric field inside the fluid and predicts the bridge instability at high aspect ratios [30]. In AC electric field, the leaky dielectric model is applicable at  $f < f_w$ . However, this criterion is only valid for the bulk fluid. The specific geometry of the bridge limits the charge transfer in the system. Essentially, the liquid bridge can be considered as a conductor with the resistance  $R_e$  that interconnects two oppositely charged droplets with the capacitance  $C$ . The response of the

system to a change of the electric field will have the characteristic frequency of  $f_{RC} \approx 1/R_e C$ , which is lower than the bulk charge relaxation frequency  $f_w$ . As a result, the electric field in the bridge remains finite at  $f < f_w$  generating longitudinal stresses and stabilizing the bridge. Finally at  $f \ll f_w$ , the electric field in the bridge relaxes to near zero and the bridge becomes unsustainable. This agrees well with the experimental observations on the transition from the oscillatory coalescence to the non-coalescence at  $f \ll f_w$  (Fig. 4.10). Additional complexity comes from a variable self-organized geometry of the bridge. For a given conductivity, the bridge thins out and becomes unstable at high electric fields (Fig. 4.7). A fine emulsion cloud is formed as a result of the bridge instability.

#### 4.9 Non-coalescence of droplets pair at low $f/f_w$

The non-coalescence of droplet pairs at  $f/f_w < 10^{-3}$  was experimentally observed for extremely low electrical capillary numbers  $Ca_E \ll 0.09$ . In Figure 4.16, the experimental results for droplet pairs are shown for the water droplets with  $\sigma_w = 0.5 \mu\text{S}/\text{cm}$  and applied frequency  $f = 60 \text{ Hz}$ . The corresponding  $f/f_w$  ratio is equal to  $8.5 \cdot 10^{-4}$  and the electrical capillary numbers  $Ca_E = 0.048$ . This ratio is below the range of oscillatory coalescence shown in the diagram Figure 4.10. Figure 4.16 (a), from  $t = 0 \text{ s}$  to  $0.8 \text{ s}$ , shows the contact of a droplet pair. The droplets first attract towards one another (Fig. 4.16a,  $t = 0 \text{ s}$  to  $0.2 \text{ s}$ ). Then, the liquid bridge forms between the droplets and stretches slightly (Fig. 4.16a,  $t = 0.3 \text{ s}$  to  $0.4 \text{ s}$ ). After that, the bridge stays for a long time, resulting in the stable non-coalescing water droplets (Fig. 4.16a,  $t = 0.5 \text{ s}$  to  $33.5 \text{ s}$ ). Similar experimental results were observed for the applied frequency of

16.8 kHz and water conductivity  $\sigma_w = 67 \mu\text{S}/\text{cm}$  at  $f/f_w = 1.8 \cdot 10^{-3}$  and the electrical capillary numbers  $Ca_E = 0.057$  (Fig. 4.17b).

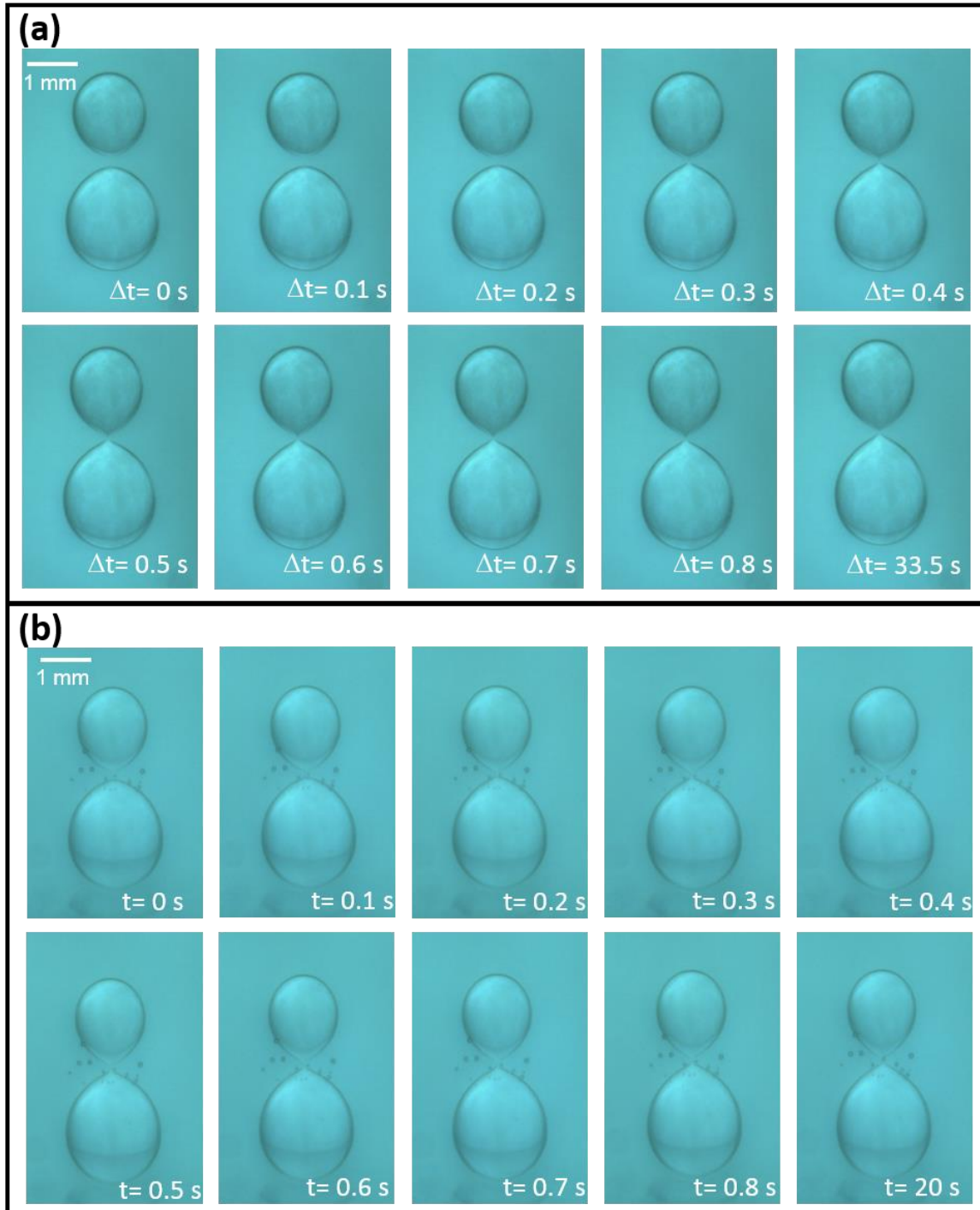


**Figure 4.16** (a) Images of stable non-coalescing water droplets at  $ff_w = 8.5 \cdot 10^{-4}$  and  $Ca_E = 0.048$  recorded the moment of contacting a droplet pair one another every 0.1 s. At  $t = 33.5$  s, the stable non-coalescing water droplets was observed. (b) Images of stable non-coalescing water droplets at  $ff_w = 1.8 \cdot 10^{-3}$  and  $Ca_E = 0.057$  recorded the moment of contacting a droplet

pair one another every 0.1 s. At  $t = 20$  s, the stable non-coalescing water droplets was observed.

These experimental results suggest that the non-coalescence of the droplet pairs extends the range of extremely low electric capillary numbers. The water droplet conductivities, applied frequencies, electrical capillary numbers, frequency ratios, and patterns of coalescence are listed in Table 4.3. The droplet pairs formed stable non-coalescing shapes at  $Ca_E = 0.057$  ( $f = 16.8$  kHz) and  $Ca_E = 0.048$  ( $f = 60$  Hz) at  $ff_w < 10^{-3}$  or  $ff_w \approx 10^{-3}$ . The droplet interaction was clearly observed in these experiments. The resolution of the optical recording system was insufficient to clearly record the bridge. However, we believe that the bridge is formed also in this case.

Data reported previously for DC case [22,91] showed existence of non-coalescence of the droplet pairs at  $Ca_E > 0.1$ . According to our results, the non-coalescence behavior of droplet pairs in AC fields is observed for electrical capillary numbers as low as  $Ca_E = 0.029$ . This surprising result requires additional studies and currently has no clear theoretical explanation. It is possible to suggest that stability of droplet pair interconnected with a bridge is achieved because of the continuous charge transfer across the bridge. The opposite charges of the droplets in the interconnected pair result in the repulsion force in the applied electric field that compensates the surface tension force. The stability of non-coalesced droplets suggests the existence of the energy barrier between the non-coalesced and fully coalesced states. This energy barrier can be explained by the initial droplet contact at the droplet spacing  $h > 2r$ . After the contact, the repulsion of the equipotential droplets is sufficient to overcome the surface tension attraction.

**Table 4.3** Experimental results are listed for the droplet pair at  $f/f_w = 8.5 \cdot 10^{-4}$  and  $f/f_w = 1.8 \cdot 10^{-3}$  with different  $Ca_E$ . Illustration of the various coalescence regimes: (A) complete coalescence on the first contact, (B) stable non-coalescing shape formation, no jet emissions, (C) non-coalescence with the oscillatory motion of the droplet pair, unstable bridge formation and emulsification, (D) non-coalescence with droplets attraction, deformation and stabilization at a certain distance with electrified jet emissions.

$\sigma_w$	$f$	$Ca_E$	$f/f_w$	Pattern
0.5 $\mu\text{S}/\text{cm}$	60 Hz	0.175	$8.5 \cdot 10^{-4}$	C
0.5 $\mu\text{S}/\text{cm}$	60 Hz	0.134	$8.5 \cdot 10^{-4}$	C
0.5 $\mu\text{S}/\text{cm}$	60 Hz	0.097	$8.5 \cdot 10^{-4}$	D
0.5 $\mu\text{S}/\text{cm}$	60 Hz	0.075	$8.5 \cdot 10^{-4}$	D
0.5 $\mu\text{S}/\text{cm}$	60 Hz	0.067	$8.5 \cdot 10^{-4}$	D
0.5 $\mu\text{S}/\text{cm}$	60 Hz	0.056	$8.5 \cdot 10^{-4}$	D
0.5 $\mu\text{S}/\text{cm}$	60 Hz	0.048	$8.5 \cdot 10^{-4}$	B
0.5 $\mu\text{S}/\text{cm}$	60 Hz	0.029	$8.5 \cdot 10^{-4}$	B
0.5 $\mu\text{S}/\text{cm}$	60 Hz	0.006	$8.5 \cdot 10^{-4}$	A
67 $\mu\text{S}/\text{cm}$	16.8 kHz	0.097	$1.8 \cdot 10^{-3}$	D
67 $\mu\text{S}/\text{cm}$	16.8 kHz	0.086	$1.8 \cdot 10^{-3}$	D
67 $\mu\text{S}/\text{cm}$	16.8 kHz	0.064	$1.8 \cdot 10^{-3}$	B
67 $\mu\text{S}/\text{cm}$	16.8 kHz	0.057	$1.8 \cdot 10^{-3}$	B

## Chapter 5. Conclusions and Future work

### 5.1 Conclusions

The electric field based method for in situ emulsification of water droplets immersed in a continuous oil phase is developed. High density water-in-oil emulsions are generated using non-uniform ac electric fields applied between needle and plate electrodes. An initial water droplet is entrained in the area of high electric field near the needle electrode where it is dispersed under the influence of high electric stresses. Breakup mechanisms responsible for a gradual dispersion of the water droplets are investigated. Identified mechanisms involve drop elongation to a cylindrical shape followed by a capillary breakup, ac electro spraying from individual water droplets, and formation and breakup of bead-like structures comprised by the water droplets interconnected by thin water bridges. Water droplets with diameters close to 1  $\mu\text{m}$  and a narrow size distribution are formed at long processing times. The generated emulsion has a well-defined boundary and is confined near the needle electrode in a shape resembling a pendant drop.

It is demonstrated that a non-uniform alternating electric field can be used to perform in situ emulsification of small water droplets initially suspended in a continuous oil phase. This system represents a leaky dielectric droplet in a pure dielectric fluid. Strong dielectrophoretic force is induced by the pin-to-plate electrical geometry. This results in dielectrophoretic entrainment and continuous dispersion of the water droplets. Breakup mechanisms responsible for a gradual dispersion of the water droplets are identified: droplet elongation and capillary breakup, ac electro spraying from individual water droplets, and

formation and breakup of bead-like structure of droplet chain. The average droplet diameter is controlled by the induced maximum electric field and processing time. Droplets with a size of a few microns are formed at high electric fields and long processing times. The droplet cloud is confined near the needle electrode in a shape resembling the distribution of the electric field near the needle electrode with a pendant droplet shape. The produced emulsion cloud has a high density and a well-defined boundary due to the variation of the dielectrophoretic force on its surface.

Partial coalescence of microdroplets is of interest for a number of microfluidic applications where a controlled fluid transfer from one droplet to another is required for mixing, dispensing and metering of chemical and biological fluids. The phenomenon of oscillatory coalescence of water droplets situated in an alternating electric field is reported. The oscillatory coalescence exists in a range of electrical capillary numbers and fluid conductivities and proceeds through a finite number of cycles. Each cycle includes attractive and repulsion stages and results in a partial fluid transfer through a liquid bridge formed between droplets during the repulsion stage. The energy model to describe the phenomena and define its limit of existence is proposed.

In summary, we have found that in a certain range of electric capillary numbers and fluid conductivities, a pair of drops in an alternating electric field coalesces through oscillatory sequence that includes the following stages: dipole-dipole attraction, formation of liquid bridge, repulsion of equipotential droplets, bridge elongation and breakup. The liquid bridge formed between droplets is stabilized by the charge transfer in an alternating electric field. Concurrently, the pressure difference between the droplets generates fluid flow through

the bridge. Once initiated, the oscillatory coalescence proceeds until complete coalescence in a finite number of steps. The region of the existence of the phenomenon is bounded by the complete coalescence on the first contact at  $Ca_E < 0.09$  and  $f/f_w > 10^{-1}$  and non-coalescence with the bridge instabilities and electrified jet emissions at  $Ca_E > 0.15$  and  $f/f_w < 3 \cdot 10^{-3}$ . The proposed model describing oscillatory motion of the droplets in energy space shows a good agreement with the experiments. The findings are useful for understanding electrically enhanced coalescence of water-in-oil emulsions, electrified droplet dynamics, and development of droplet manipulation methods. The main potential application of the phenomenon is the electrically controllable droplet-to-droplet fluid transfer and precise dispensing of bio and chemical reagents from freely suspended droplets in microfluidic devices based on the lab-on-a-chip and lab-in-a-droplet platforms.

## 5.2 Future work

While emulsifying droplets, electric fields inside emulsion cloud drops because dielectric permittivity of the suspension  $\epsilon_e$  is greater than the electric permittivity of the oil  $\epsilon_{co}$  if the continuity of the electric displacement field is assumed [84]. To compensate the electric field drop, reducing the interfacial tension is an alternative to reduce the droplet size. Water soluble surfactants such as sodium oleate can reduce the interfacial tension in castor oil. As a result of that, the droplet size can be reduced.

Data reported previously for DC case [22,91] showed existence of non-coalescence of the droplet pairs at  $Ca_E > 0.1$ . According to our results shown in the Table 4.3, the non-

coalescence behavior of droplet pairs in AC fields is observed for lower electrical capillary numbers. It is possible to suggest that stability of droplet pair interconnected with a bridge is achieved because of the continuous charge transfer across the bridge. The opposite charges of the droplets in the interconnected pair result in the repulsion force in the applied electric field that compensates the surface tension force. The stability of non-coalesced droplets suggests the existence of the energy barrier between the non-coalesced and fully coalesced states. This energy barrier can be explained by the initial droplet contact at the droplet spacing  $h > 2r$ . After the contact, the repulsion of the equipotential droplets is sufficient to overcome the surface tension attraction. This unexpected result requires additional studies and theoretical explanation.

## REFERENCES

- [1] H.A. Pohl, H. Pohl, Dielectrophoresis: The Behavior of Neutral Matter in Nonuniform Electric Fields, Cambridge university press Cambridge, 1978.
- [2] G. Taylor, Disintegration of water drops in an electric field, 280 (1964) 383-397.
- [3] E. Lac, G.M. Homsy, Axisymmetric deformation and stability of a viscous drop in a steady electric field, J. Fluid Mech. 590 (2007) 239-264.
- [4] T.J. Williams, A.G. Bailey, Changes in the size distribution of a water-in-oil emulsion due to electric field induced coalescence, IEEE Trans. Ind. Appl. (1986) 536-541.
- [5] J.S. Eow, M. Ghadiri, A.O. Sharif, T.J. Williams, Electrostatic enhancement of coalescence of water droplets in oil: a review of the current understanding, Chem. Eng. J. 84 (2001) 173-192.
- [6] W.D. Ristenpart, J.C. Bird, A. Belmonte, F. Dollar, H.A. Stone, Non-coalescence of oppositely charged drops, Nature. 461 (2009) 377-380.
- [7] B.S. Hamlin, J.C. Creasey, W.D. Ristenpart, Electrically Tunable Partial Coalescence of Oppositely Charged Drops, Phys. Rev. Lett. 109 (2012) 094501.
- [8] T. Hamouda, J. Baker, Antimicrobial mechanism of action of surfactant lipid preparations in enteric Gram-negative bacilli, J. Appl. Microbiol. 89 (2000) 397-403.

- [9] J.M. Odeberg, P. Kaufmann, K. Kroon, P. Höglund, Lipid drug delivery and rational formulation design for lipophilic drugs with low oral bioavailability, applied to cyclosporine, *European journal of pharmaceutical sciences*. 20 (2003) 375-382.
- [10] O. Sonnevile-Aubrun, J. Simonnet, F. L'alloret, Nanoemulsions: a new vehicle for skincare products, *Adv. Colloid Interface Sci.* 108 (2004) 145-149.
- [11] A. Fernández-Nieves, G. Cristobal, V. Garcés-Chávez, G.C. Spalding, K. Dholakia, D.A. Weitz, Optically anisotropic colloids of controllable shape, *Adv Mater.* 17 (2005) 680-684.
- [12] I. Cohen, H. Li, J.L. Houglund, M. Mrksich, S.R. Nagel, Using selective withdrawal to coat microparticles, *Science*. 292 (2001) 265-267.
- [13] S.L. Anna, N. Bontoux, H.A. Stone, Formation of dispersions using “flow focusing” in microchannels, *Appl. Phys. Lett.* 82 (2003) 364-366.
- [14] W.W. Zhang, Viscous entrainment from a nozzle: singular liquid spouts, *Phys. Rev. Lett.* 93 (2004) 184502.
- [15] H. Willaime, V. Barbier, L. Kloul, S. Maine, P. Tabeling, Arnold tongues in a microfluidic drop emitter, *Phys. Rev. Lett.* 96 (2006) 054501.
- [16] S.C. du Pont, J. Eggers, Sink flow deforms the interface between a viscous liquid and air into a tip singularity, *Phys. Rev. Lett.* 96 (2006) 034501.

- [17] M. Sato, T. Hatori, M. Saito, Experimental investigation of droplet formation mechanisms by electrostatic dispersion in a liquid-liquid system, *IEEE Trans. Ind. Appl.* 33 (1997) 1527-1534.
- [18] A. Barrero, J. Lopez-Herrera, A. Boucard, I. Loscertales, M. Marquez, Steady cone-jet electrosprays in liquid insulator baths, *J. Colloid Interface Sci.* 272 (2004) 104-108.
- [19] L. Rayleigh, The influence of electricity on colliding water drops, *Proceedings of the Royal Society of London.* 28 (1878) 405-409.
- [20] D. Sartor, A LABORATORY INVESTIGATION OF COLLISION EFFICIENCIES, COALESCENCE AND ELECTRICAL CHARGING SIMULATED CLOUD DROPLETS, *J. Meteorol.* 11 (1954) 91-103.
- [21] R. Allan, S. Mason, Effects of electric fields on coalescence in liquid liquid systems, *Transactions of the Faraday Society.* 57 (1961) 2027-2040.
- [22] J.C. Bird, W.D. Ristenpart, A. Belmonte, H.A. Stone, Critical Angle for Electrically Driven Coalescence of Two Conical Droplets, *Phys. Rev. Lett.* 103 (2009) 164502.
- [23] A. Castellanos, A. Ramos, A. Gonzalez, N. Green, H. Morgan, Electrohydrodynamics and dielectrophoresis in microsystems: scaling laws, *Journal of Physics D-Applied Physics.* 36 (2003) 2584-2597.

- [24] A. Ramos, H. Morgan, N.G. Green, A. Castellanos, Ac electrokinetics: a review of forces in microelectrode structures, *J. Phys. D.* 31 (1998) 2338.
- [25] J. Zeleny, The electrical discharge from liquid points, and a hydrostatic method of measuring the electric intensity at their surfaces, *Physical Review.* 3 (1914) 69.
- [26] J. Zeleny, Instability of electrified liquid surfaces, *Physical review.* 10 (1917) 1.
- [27] G. Taylor, Studies in electrohydrodynamics. I. The circulation produced in a drop by electrical field, 291 (1966) 159-166.
- [28] J.C. Baygents, N.J. Rivette, H.A. Stone, Electrohydrodynamic deformation and interaction of drop pairs, *J. Fluid Mech.* 368 (1998) 359-375.
- [29] M. CLOUPEAU, B. PRUNETFOCH, Electrohydrodynamic Spraying Functioning Modes - a Critical-Review, *J. Aerosol Sci.* 25 (1994) 1021-1036.
- [30] C.L. Burcham, D.A. Saville, Electrohydrodynamic stability: Taylor-Melcher theory for a liquid bridge suspended in a dielectric gas, *J. Fluid Mech.* 452 (2002) 163-187.
- [31] R.T. Collins, J.J. Jones, M.T. Harris, O.A. Basaran, Electrohydrodynamic tip streaming and emission of charged drops from liquid cones, *Nat. Phys.* 4 (2008) 149-154.
- [32] C. Sozou, Electrohydrodynamics of a Liquid Drop - Development of Flow Field, *Proceedings of the Royal Society of London Series A-Mathematical Physical and Engineering Sciences.* 334 (1973) 343-356.

- [33] S. Kanazawa, Y. Takahashi, Y. Nomoto, Emulsification and demulsification processes in liquid-liquid system by electrostatic atomization technique, *IEEE Trans. Ind. Appl.* 44 (2008) 1084-1089.
- [34] A.M. Ganan-Calvo, J.M. Lopez-Herrera, P. Riesco-Chueca, The combination of electrospray and flow focusing, *J. Fluid Mech.* 566 (2006) 421-445.
- [35] J.F. de la Mora, The fluid dynamics of Taylor cones, *Annu. Rev. Fluid Mech.* 39 (2007) 217-243.
- [36] R. Allan, S. Mason, Particle behaviour in shear and electric fields. I. Deformation and burst of fluid drops, *J. Fluid Mech.* 267 (1962) 45-61.
- [37] D. Saville, Electrohydrodynamics: the Taylor-Melcher leaky dielectric model, *Annu. Rev. Fluid Mech.* 29 (1997) 27-64.
- [38] N.G. Green, Dielectrophoresis and AC electrokinetics, in: *Anonymous Electrokinetics and Electrohydrodynamics in Microsystems*, Springer, 2011, pp. 61-84.
- [39] O. Ajayi, A note on Taylor's electrohydrodynamic theory, *J. Fluid Mech.* 364 (1978) 499-507.
- [40] E. Lac, G.M. Homsy, Axisymmetric deformation and stability of a viscous drop in a steady electric field, *J. Fluid Mech.* 590 (2007) 239-264.
- [41] M.J. Miksis, Shape of a drop in an electric field, *Physics of Fluids* (1958-1988). 24 (1981) 1967-1972.

- [42] J. Sherwood, Breakup of fluid droplets in electric and magnetic fields, *J. Fluid Mech.* 188 (1988) 133-146.
- [43] N. Dubash, A. Mestel, Behaviour of a conducting drop in a highly viscous fluid subject to an electric field, *J. Fluid Mech.* 581 (2007) 469-493.
- [44] J. Ha, S. Yang, Deformation and breakup of Newtonian and non-Newtonian conducting drops in an electric field, *J. Fluid Mech.* 405 (2000) 131-156.
- [45] R.B. Karyappa, S.D. Deshmukh, R.M. Thaokar, Breakup of a conducting drop in a uniform electric field, *J. Fluid Mech.* 754 (2014) 550-589.
- [46] C.T. Wilson, G. Taylor, The bursting of soap-bubbles in a uniform electric field, 22 (1925) 728-730.
- [47] H. Morgan, N.G. Green, *AC Electrokinetics*, Research Studies Press, 2003.
- [48] M.A. Nawab, S.G. Mason, The preparation of uniform emulsions by electrical dispersion, *J. Colloid Sci.* 13 (1958) 179-187.
- [49] M.P. Hughes, H. Morgan, Dielectrophoretic trapping of single sub-micrometre scale bioparticles, *J. Phys. D.* 31 (1998) 2205.
- [50] T. Scott, W. Sisson, Droplet size characteristics and energy input requirements of emulsions formed using high-intensity-pulsed electric fields, *Sep. Sci. Technol.* 23 (1988) 1541-1550.

- [51] T.C. Scott, D.W. DePaoli, W.G. Sisson, Further development of the electrically driven emulsion-phase contactor, *Ind Eng Chem Res.* 33 (1994) 1237-1244.
- [52] S. Choi, A.V. Saveliev, In situ emulsification using a non-uniform alternating electric field, *Appl. Phys. Lett.* 105 (2014) 074105.
- [53] S. Mhatre, R. Thaokar, Pin-Plate Electrode System for Emulsification of a Higher Conductivity Leaky Dielectric Liquid into a Low Conductivity Medium, *Ind Eng Chem Res.* 53 (2014) 13488-13496.
- [54] N. Otsu, A threshold selection method from gray-level histograms, *Automatica.* 11 (1975) 23-27.
- [55] E. de Juan, B. McCuen, J. Tiedeman, Intraocular tamponade and surface tension, *Surv. Ophthalmol.* 30 (1985) 47-51.
- [56] Y. Rotenberg, L. Boruvka, A. Neumann, Determination of surface tension and contact angle from the shapes of axisymmetric fluid interfaces, *J. Colloid Interface Sci.* 93 (1983) 169-183.
- [57] C. Huh, R. Reed, A method for estimating interfacial tensions and contact angles from sessile and pendant drop shapes, *J. Colloid Interface Sci.* 91 (1983) 472-484.

- [58] A.R. White, T. Ward, Pattern search methods for pendant drops: Algorithms for rapid determination of surface tension and surfactant transport parameters, *Colloids Surf. Physicochem. Eng. Aspects.* 485 (2015) 1-10.
- [59] R. Hengelmolen, B. Vincent, G. Hassall, Emulsions from Aerosol Sprays, *J. Colloid Interface Sci.* 196 (1997) 12-22.
- [60] L.Y. Yeo, D. Lastochkin, S.C. Wang, H.C. Chang, A new ac electro spray mechanism by Maxwell-Wagner polarization and capillary resonance, *Phys. Rev. Lett.* 92 (2004) 133902.
- [61] A.M. Ganan-Calvo, J.M. Lopez-Herrera, P. Riesco-Chueca, The combination of electro spray and flow focusing, *J. Fluid Mech.* 566 (2006) 421-445.
- [62] Y. Wang, M.K. Tan, D.B. Go, H. Chang, Electro spray cone-jet breakup and droplet production for electrolyte solutions, *Epl.* 99 (2012) 64003.
- [63] M. CLOUPEAU, B. PRUNETFOCH, Electrohydrodynamic Spraying Functioning Modes - a Critical-Review, *J. Aerosol Sci.* 25 (1994) 1021-1036.
- [64] J.B. Fenn, M. Mann, C.K. Meng, S.F. Wong, C.M. Whitehouse, Electro spray Ionization for Mass-Spectrometry of Large Biomolecules, *Science.* 246 (1989) 64-71.
- [65] D. Lastochkin, H. Chang, A high-frequency electro spray driven by gas volume charges, *J. Appl. Phys.* 97 (2005) 123309.

- [66] S. Maheshwari, N. Chetwani, H. Chang, Alternating Current Electrospraying, *Ind Eng Chem Res.* 48 (2009) 9358-9368.
- [67] M. Sato, T. Hatori, M. Saito, Experimental investigation of droplet formation mechanisms by electrostatic dispersion in a liquid-liquid system, *IEEE Trans. Ind. Appl.* 33 (1997) 1527-1534.
- [68] A. Barrero, J. Lopez-Herrera, A. Boucard, I. Loscertales, M. Marquez, Steady cone-jet electrosprays in liquid insulator baths, *J. Colloid Interface Sci.* 272 (2004) 104-108.
- [69] H. Kim, D. Luo, D. Link, D.A. Weitz, M. Marquez, Z. Cheng, Controlled production of emulsion drops using an electric field in a flow-focusing microfluidic device, *Appl. Phys. Lett.* 91 (2007) 133106.
- [70] P. He, H. Kim, D. Luo, M. Marquez, Z. Cheng, Low-frequency ac electro-flow-focusing microfluidic emulsification, *Appl. Phys. Lett.* 96 (2010) 174103.
- [71] S. Kanazawa, Y. Takahashi, Y. Nomoto, Emulsification and demulsification processes in liquid-liquid system by electrostatic atomization technique, *IEEE Trans. Ind. Appl.* 44 (2008) 1084-1089.
- [72] J. Eow, M. Ghadiri, Motion, deformation and break-up of aqueous drops in oils under high electric field strengths, *Chem. Eng. Process.* 42 (2003) 259-272.

- [73] L. He, D. Yang, R. Gong, T. Ye, Y. Lü, X. Luo, An investigation into the deformation, movement and coalescence characteristics of water-in-oil droplets in an AC electric field, *Petroleum Science*. 10 (2013) 548-561.
- [74] A.R. Thiam, N. Bremond, J. Bibette, Breaking of an Emulsion under an ac Electric Field, *Phys. Rev. Lett.* 102 (2009) 188304.
- [75] S. Mhatre, R.M. Thaokar, Drop motion, deformation, and cyclic motion in a non-uniform electric field in the viscous limit, *Phys. Fluids*. 25 (2013) 072105.
- [76] M.M. Ahn, I.S. Kang, Geometric characterization of optimal electrode designs for improved droplet charging and actuation, *Analyst*. 138 (2013) 7362-7368.
- [77] A. Castellanos, A. Ramos, A. Gonzalez, N. Green, H. Morgan, Electrohydrodynamics and dielectrophoresis in microsystems: scaling laws, *Journal of Physics D-Applied Physics*. 36 (2003) 2584-2597.
- [78] A. Ramos, H. Morgan, N. Green, A. Castellanos, Ac electrokinetics: a review of forces in microelectrode structures, *Journal of Physics D-Applied Physics*. 31 (1998) 2338-2353.
- [79] Z.R. Gagnon, H. Chang, Dielectrophoresis of ionized gas microbubbles: Dipole reversal due to diffusive double-layer polarization, *Appl. Phys. Lett.* 93 (2008) 224101.

- [80] M. Desmond, N. Mavrogiannis, Z. Gagnon, Maxwell-Wagner Polarization and Frequency-Dependent Injection at Aqueous Electrical Interfaces, *Phys. Rev. Lett.* 109 (2012) 187602.
- [81] H. Lamb, *Hydrodynamics*, Cambridge university press, 1932.
- [82] A. Yarin, Stationary d.c. streaming due to shape oscillations of a droplet and its effect on mass transfer in liquid-liquid systems, *J. Fluid Mech.* 444 (2001) 321-342.
- [83] F. FOWKES, Determination of Interfacial Tensions, Contact Angles, and Dispersion Forces in Surfaces by Assuming Additivity of Intermolecular Interactions in Surfaces, *J. Phys. Chem.* 66 (1962) 382-&.
- [84] T. Hanai, Dielectric properties of emulsions, *Kolloid-Zeitschrift.* 177 (1961) 57-61.
- [85] H. Coxeter, Close-packing and froth, *Illinois Journal of Mathematics.* 2 (1958) 746-758.
- [86] S. TAYLOR, Investigations into the Electrical and Coalescence Behavior of Water-In-Crude Oil-Emulsions in High-Voltage Gradients, *Colloids and Surfaces.* 29 (1988) 29-51.
- [87] H. Chang, E. Demekhin, E. Kalaidin, Iterated stretching of viscoelastic jets, *Phys. Fluids.* 11 (1999) 1717-1737.
- [88] G. Taylor, Electrically Driven Jets, *Proceedings of the Royal Society of London Series A-Mathematical and Physical Sciences.* 313 (1969) 453-&.

- [89] D.H. Reneker, A.L. Yarin, Electrospinning jets and polymer nanofibers, *Polymer*. 49 (2008) 2387-2425.
- [90] R.B. Karyappa, A.V. Naik, R.M. Thaokar, Electroemulsification in a Uniform Electric Field, *Langmuir*. 32 (2016) 46-54.
- [91] P.R. Brazier-Smith, S.G. Jennings, J. Latham, Investigation of Behaviour of Drops and Drop-Pairs Subjected to Strong Electrical Forces, *Proceedings of the Royal Society of London Series A-Mathematical and Physical Sciences*. 325 (1971) 363-13.
- [92] T. Jones, Effective dipole moment of intersecting conducting spheres, *J. Appl. Phys.* 62 (1987) 362-365.
- [93] I.W. McAllister, The axial dipole moment of two intersecting spheres of equal radii, *J. Appl. Phys.* 63 (1988) 2158-2160.
- [94] T. Jones, Dipole moments of conducting particle chains, *J. Appl. Phys.* 60 (1986) 2226-2230.
- [95] T.B. Jones, B. Rubin, Forces and Torques on Conducting Particle Chains, *J. Electrostatics*. 21 (1988) 121-134.
- [96] H. Gonzalez, F.M.J. Mccluskey, A. Castellanos, A. Barrero, Stabilization of Dielectric Liquid Bridges by Electric-Fields in the Absence of Gravity, *J. Fluid Mech.* 206 (1989) 545-561.

## **APPENDICES**

# MATLAB SCRIPTS FOR IMAGE ANALYSIS AND DROPLET VOLUME MEASUREMENT

The data presented in this dissertation were extracted from the CCD camera using the Matlab (version of R2013a). The data analysis was performed on a 3.33 GHz desktop with 7 Gb of ram running 64 bit edition of Microsoft Windows 7.

The volume analysis script need an input video file (in AVI format), for example `'Stack 534-544_1_top_1.avi'` is a name of the video file for the analysis. Images are converted to binary images by the Converting to Binary Image Function in A.3. The droplet interface is traced by Droplet Interface Finding Function in A.4. Droplet volume is first analyzed by integrating the right interface using Droplet Volume Integration in Right-hand-side Function in A.5. Then Droplet Volume Integration in Right-hand-side Function in A.6 is used for integrating the left interface. Both values are averaged for the final volume of the droplet.

## Appendix A: Volume Analysis Script

```
s1='Stack 534-544_1_top_1.avi';  
x1=5; x2=1387; y1=1035; y2=5;  
thresh=65;  
R_out=0.3048;  
pix=55.15;  
m = VideoReader(s1);  
nFrames = m.NumberOfFrames;
```

```

for i=1:nFrames

    a=read(m,i);

    a=imcomplement(a);

    [xs]=center_drop(a,thresh);

    [A] = image_mod(a,x1,x2,y2,y1,thresh);

    [extery,exterx] =exterior_mapper(A,xs);

    [Vol_right,Y_r,X_r,y_r,x_r]=vol_function_v1(exterx,extery,xs,R_out,pix);

    [Vol_left,Y_l,X_l,y_l,x_l]=vol_function_v2(exterx,extery,xs,R_out,pix);

    Volume(i)=0.5*(Vol_right+Vol_left);

end

```

## Appendix B: Droplet Center Finding Function

```

function [xs]=center_drop(a,thresh);

q=0;

q1=0;

x=size(a);

x1=x(1);

x2=x(2);

col=1;

while(q1==0)

    q=0;

    x1=x(1);

    while(q==0)

        if(a(x1,col,1) < thresh)

            a(:,col,:)=0;

            q=1;


```

```

        else
            x1=x1-1;
            if(x1==1)
                q=2;
                col=col+1;
            end
        end
    end
end
if(col==x2)
    q1=1;
elseif(q==1)
    q1=2;
end
end
q=0;
q1=0;
col=x(2);
while(q1==0)
    q=0;
    x1=x(1);
    while(q==0)
        if(a(x1,col,1) < thresh)
            a(:,col,:)=0;
            q=1;
        else
            x1=x1-1;
            if(x1==1)

```

```

        q=2;
        col=col-1;
    end
end
end
if(col==1)
    q1=1;
elseif(q==1)
    q1=2;
end
end
xs=round(0.5*(right_side+left_side));

```

### Appendix C: Converting to Binary Image Function

```

function [a] = image_mod(a,x1,x2,y1,y2,thresh)
pix(:,:)=a(:,:);
pix=double(pix);
a=medfilt2(pix,[2 2]);
for j=1:y1-1
    for k=1:size(a,2)
        a(j,k)=0;
    end
end
for j=y2+1:size(a,1)
    for k=1:size(a,2)
        a(j,k)=0;
    end
end

```

```

        end
    end
end
for j=y1:y2
    for k=1:x1-1
        a(j,k)=0;
    end
    for k=x2+1:size(a,2)
        a(j,k)=0;
    end
    for k=x1:x2
        if a(j,k)<thresh;
            a(j,k)=255;
        else
            a(j,k)=0;
        end
    end
end
end
end

```

#### Appendix D: Droplet Interface Finding Function

```

function [extery,exterx] =exterior_mapper(a,xs)
out=0;
i=size(a,1)-1;
while out==0
    if a(i,xs)>0 && a(i+1,xs)>0 && a(i+2,xs)==0
        ys=i+1;
    end
end

```

```

        out=1;

    else
        i=i-1;
    end

end

end

j=ys; k=xs;
extery(1)=j;exterx(1)=k;
s=2;
dir=1;
out=0;
while out==0
    mid=0;
    while mid==0
        if dir==1
            in=0;
            while in==0
                if a(j,k+1)>0
                    k=k+1;extery(s)=j;exterx(s)=k;
                    s=s+1;dir=4;in=1;
                elseif a(j-1,k+1)>0
                    j=j-1;k=k+1;extery(s)=j;exterx(s)=k;
                    s=s+1;dir=4;in=1;
                elseif a(j-1,k)>0
                    j=j-1;extery(s)=j;exterx(s)=k;
                    s=s+1;dir=1;in=1;
                elseif a(j-1,k-1)>0
                    j=j-1;k=k-1;extery(s)=j;exterx(s)=k;

```

```

        s=s+1;dir=1;in=1;
elseif a(j,k-1)>0
        k=k-1;extery(s)=j;exterx(s)=k;
        s=s+1;dir=2;in=1;
elseif a(j+1,k-1)>0
        j=j+1;k=k-1;extery(s)=j;exterx(s)=k;
        s=s+1;dir=2;in=1;
elseif a(j+1,k)>0
        j=j+1;extery(s)=j;exterx(s)=k;
        s=s+1;dir=3;in=1;
elseif a(j+1,k+1)>0
        j=j+1;k=k+1;extery(s)=j;exterx(s)=k;
        s=s+1;dir=3;in=1;
end
end
mid=1;
elseif dir==2
        in=0;
        while in==0
                if a(j-1,k)>0
                        j=j-1;extery(s)=j;exterx(s)=k;
                        s=s+1;dir=1;in=1;
                elseif a(j-1,k-1)>0
                        j=j-1;k=k-1;extery(s)=j;exterx(s)=k;
                        s=s+1;dir=1;in=1;
                elseif a(j,k-1)>0
                        k=k-1;extery(s)=j;exterx(s)=k;

```

```

        s=s+1;dir=2;in=1;
elseif a(j+1,k-1)>0
    j=j+1;k=k-1;extery(s)=j;exterx(s)=k;
    s=s+1;dir=2;in=1;
elseif a(j+1,k)>0
    j=j+1;extery(s)=j;exterx(s)=k;
    s=s+1;dir=3;in=1;
elseif a(j+1,k+1)>0
    j=j+1;k=k+1;extery(s)=j;exterx(s)=k;
    s=s+1;dir=3;in=1;
elseif a(j,k+1)>0
    k=k+1;extery(s)=j;exterx(s)=k;
    s=s+1;dir=4;in=1;
elseif a(j-1,k+1)>0
    j=j-1;k=k+1;extery(s)=j;exterx(s)=k;
    s=s+1;dir=4;in=1;
end
end
mid=1;
elseif dir==3
    in=0;
while in==0
    if a(j,k-1)>0
        k=k-1;extery(s)=j;exterx(s)=k;
        s=s+1;dir=2;in=1;
elseif a(j+1,k-1)>0
    j=j+1;k=k-1;extery(s)=j;exterx(s)=k;

```

```

        s=s+1;dir=2;in=1;
elseif a(j+1,k)>0
    j=j+1;extery(s)=j;exterx(s)=k;
    s=s+1;dir=3;in=1;
elseif a(j+1,k+1)>0
    j=j+1;k=k+1;extery(s)=j;exterx(s)=k;
    s=s+1;dir=3;in=1;
elseif a(j,k+1)>0
    k=k+1;extery(s)=j;exterx(s)=k;
    s=s+1;dir=4;in=1;
elseif a(j-1,k+1)>0
    j=j-1;k=k+1;extery(s)=j;exterx(s)=k;
    s=s+1;dir=4;in=1;
elseif a(j-1,k)>0
    j=j-1;extery(s)=j;exterx(s)=k;
    s=s+1;dir=1;in=1;
elseif a(j-1,k-1)>0
    j=j-1;k=k-1;extery(s)=j;exterx(s)=k;
    s=s+1;dir=1;in=1;
end
end
mid=1;
elseif dir==4
    in=0;
while in==0
    if a(j+1,k)>0
        j=j+1;extery(s)=j;exterx(s)=k;

```

```

        s=s+1;dir=3;in=1;
elseif a(j+1,k+1)>0
        j=j+1;k=k+1;extery(s)=j;exterx(s)=k;
        s=s+1;dir=3;in=1;
elseif a(j,k+1)>0
        k=k+1;extery(s)=j;exterx(s)=k;
        s=s+1;dir=4;in=1;
elseif a(j-1,k+1)>0
        j=j-1;k=k+1;extery(s)=j;exterx(s)=k;
        s=s+1;dir=4;in=1;
elseif a(j-1,k)>0
        j=j-1;extery(s)=j;exterx(s)=k;
        s=s+1;dir=1;in=1;
elseif a(j-1,k-1)>0
        j=j-1;k=k-1;extery(s)=j;exterx(s)=k;
        s=s+1;dir=1;in=1;
elseif a(j,k-1)>0
        k=k-1;extery(s)=j;exterx(s)=k;
        s=s+1;dir=2;in=1;
elseif a(j+1,k-1)>0
        j=j+1;k=k-1;extery(s)=j;exterx(s)=k;
        s=s+1;dir=2;in=1;
end
end
mid=1;
end
end

```

```

    if extery(s-1)==ys && exterx(s-1)==xs
        out=1;
    end
end
end
end

```

## Appendix E: Droplet Volume Integration in Right-hand-side Function

```

function [Vol,Y1,X1,y,x]=vol_function_v1(exterx,extery,xs,R_out,pix);
x=exterx-xs;
y=extery(1)-extery;
s=size(x);
s1=s(2);
j=1;
for i=1:s1
    if x(i)>=0
        Y(j)=y(i);
        X(j)=x(i);
        j=j+1;
    end
end
end
S=size(X);
S1=S(2);
k=1;
for i=1:S1
    if Y(i)>min(Y) & Y(i)<max(Y)
        Y1(k)=Y(i);
    end
end

```

```

        X1(k)=X(i);
        k=k+1;
    end
end
SS=size(X1);
SS1=SS(2);
X_dim=X1.*(R_out/pix);
for i=1:SS1
    v(i)=pi*((X_dim(i))^2)*(R_out/pix);
end
Vol=sum(v);

```

## Appendix F: Droplet Left-side Interface Tracking Function

```

function [Vol,Y,X,y,x]=vol_function_v2(exterx,extery,xs,R_out,pix);
x=-(exterx-xs);
y=extery(1)-extery;
s=size(x);
s1=s(2);
j=1;
for i=1:s1
    if x(i)>=0
        Y(j)=y(i);
        X(j)=x(i);
        j=j+1;
    end
end
end

```

```

S=size(X);
S1=S(2);
k=1;
for i=1:S1
    if Y(i)>min(Y) & Y(i)<max(Y)
        Y1(k)=Y(i);
        X1(k)=X(i);
        k=k+1;
    end
end
SS=size(X1);
SS1=SS(2);
X_dim=X1.*(R_out/pix);
for i=1:SS1
    v(i)=pi*((X_dim(i))^2)*(R_out/pix);
end
Vol=sum(v);

```